



POLITECNICO DI MILANO

SCHOOL OF INDUSTRIAL AND INFORMATION ENGINEERING

DEPARTMENT OF ENERGY

CEA - CADARACHE

LABORATOIRE D'ESSAIS DE THERMOYDRAULIQUE ET D'HYDROMÉCANIQUE
ANALYTIQUE DU CŒUR ET DES CIRCUITS

MASTER OF SCIENCE IN NUCLEAR ENGINEERING

Experimental study on the behaviour
of 4 half-scale PWR fuel assemblies
under seismic excitation

Advisors:

Marco Enrico Ricotti - *PoliMi*

Guillaume Ricciardi - *CEA*

Co-Advisor:

Roberto Capanna

Author

Lorenzo Longo

872558

ACADEMIC YEAR 2018-2019

Lorenzo Longo: *Experimental study on the behaviour of 4 half-scale PWR fuel assemblies under seismic excitation* | Master Thesis in Nuclear Engineering, Politecnico di Milano, © Copyright 2019.

Politecnico di Milano:
www.polimi.it

CEA:
www.cea.fr

School of Industrial and Information Engineering:
www.ingindinf.polimi.it

*"Papà, come fa a bruciare il sole nello spazio se non c'è aria?"
A mio fratello*

Estratto

Il presente documento è il resoconto dell'attività sperimentale sostenuta presso il CEA di Cadarache, nel periodo di stage tra Gennaio e Luglio 2018. Tale attività di ricerca sperimentale è contestualizzata in un più ampio progetto di ricerca mirante a sviluppare un nuovo modello semplificato di interazione fluido struttura. La validazione di tale modello avviene sia per via computazionale che per via sperimentale.

In questo contesto le più recenti campagne sperimentali necessarie a validare il modello, sono state condotte ed analizzate durante il periodo di stage. In questo estratto verranno forniti i background teorici essenziali e i risultati principali seguendo l'ordine rispettato nella stesura della tesi. Dopo una breve introduzione al soggetto seguiranno le equazioni chiave del modello e dai cenni di analisi dei segnali. Quindi le tecniche di velocimetria usate nell'ambito sperimentale saranno illustrate teoricamente per concludere la parte di conoscenze teoriche. Sarà poi fornita una descrizione del setup sperimentale e delle modifiche effettuate per condurre le nuove campagne sperimentali. Le peculiarità del codice computazionale sviluppato saranno presentati ed in seguito l'analisi dei dati sperimentali verrà proposta sottolineandone i risultati principali.

Introduzione al caso in studio

Il CEA è uno dei più importanti centri di ricerca francesi ed mondiali nel campo della ricerca e sviluppo di nuove tecnologie nucleari. È dislocato su tutto il territorio francese ed è complessivamente organizzato in 4 direzioni, ognuna delle quali divise in dipartimenti, a loro volta composti da servizi cui fanno capo i laboratori. Il laboratorio LTHC fa parte del Servizio delle tecnologie dei componenti (STCP), nel Dipartimento per le tecnologie nucleari (DTN) che fa capo alla Direzione per l'energia nucleare (DEN).

Il laboratorio LTHC si occupa di termoidraulica applicata al core dei reattori nucleari. Da diversi anni è attivo nello studio dell'interazione fluido-struttura presente tra gli assemblaggi di combustibile presenti nei core dei reattori pressurizzati. La ricerca e lo sviluppo di modelli per l'interazione fluido-struttura sono giustificati dalla necessità di capire il comportamento dinamico degli assemblaggi di combustibile. Tali assemblaggi sono costituiti da centinaia di barre di combustibile tenuti insieme da 10 griglie disposte su varie altezze. Questi sono poi soggetti ad un flusso d'acqua che ne influenza il comportamento. Si possono facilmente individuare almeno due motivi per la non linearità del comportamento degli assemblaggi, ovvero: l'attrito

nei numerosissimi punti di contatto griglia-barra di combustibile e l'interazione col fluido moderatore.

Per l'industria nucleare, lo studio del comportamento dinamico degli assemblaggi è fondamentale; infatti, in caso di scosse sismiche o di improvvisi abbassamenti del livello dell'acqua, gli assemblaggi sarebbero sottoposti a forti vibrazioni. Queste vibrazioni possono indurre lo scontro tra gli assemblaggi e, se troppo violente, possono portare alla deformazione o persino alla rottura delle griglie o delle barre. In questo modo il comportamento meccanico dell'assemblaggio danneggiato è inficiato ed il corretto funzionamento non è più garantito. Un assemblaggio con le griglie rotte è considerato come non funzionante.

Si capisce quindi che in fase di progettazione è fondamentale valutare le forze in gioco nell'interazione tra gli assemblaggi. Per questo l'industria nucleare è ghiotta di modelli semplici e computazionalmente rapidi, in grado di valutare i parametri in gioco nel comportamento dinamico del core nel suo insieme, ed in particolare dei singoli assemblaggi.

Modello semplificato per l'interazione fluido-struttura

Tra i diversi modelli, lineari e non, per descrivere il comportamento dinamico del core, lo stato dell'arte è rappresentato dal *approccio a mezzo poroso*. Tale modello è stato proposto da (Ricciardi, 2008) e come suggerito dal nome, considera l'intero volume del core come se fosse un unico mezzo poroso, unendo nel volume d'esame sia le forze applicate dal fluido sulla struttura, che quelle applicate dalla struttura sul fluido. Nonostante gli ottimi risultati, questo modello rimane computazionalmente oneroso.

Nell'ambito di un progetto di dottorato, un modello semplificato è stato proposto da (Capanna, 2018). Tale modello considera il singolo assemblaggio di combustibile modellato con la teoria della trave di Eulero, mentre il fluido viene modellato sotto l'ipotesi di irrotazionalità, ovvero viene considerato un modello basato sul flusso potenziale con un fluido non viscoso, incomprimibile e newtoniano. Le ipotesi sulla struttura, (assemblaggio) sono:

1. lunghezza molto maggiore dello spessore;
2. ogni sezione trasversale dell'assemblaggio è ugualmente flessa;
3. gli effetti gravitazionali (flessione dovuta al peso) sono trascurati;
4. il materiale ha un comportamento lineare;
5. le deformazioni sono piccole rispetto allo spessore dell'assemblaggio

Tali ipotesi sul flusso e sull'assemblaggio portano alla definizione del seguente

modello matematico:

$$\begin{cases} \hat{m} \frac{\partial^2 \hat{w}(\hat{z}, \hat{t})}{\partial \hat{t}^2} + \hat{\beta} \frac{\partial^4 \hat{w}(\hat{z}, \hat{t})}{\partial \hat{z}^4} = \int_0^{2\pi} \hat{p} \sin \theta \hat{R} d\theta \\ \nabla^2 \hat{p} = 0 \\ \left. \frac{\partial \hat{p}}{\partial \hat{y}} \right|_{\hat{y}=\hat{l}_y} = \left. \frac{\partial \hat{p}}{\partial \hat{x}} \right|_{\hat{x}=\hat{l}_x} = 0 \\ \left. \frac{\partial \hat{p}}{\partial \hat{y}} \right|_{\hat{r}=\hat{R}} = -(\partial_{\hat{t}} + \partial_{\hat{z}})^2 \hat{w}(\hat{z}, \hat{t}) \sin \theta \end{cases}$$

Di tale sistema si fornisce la notazione utilizzata: \hat{m} è la massa lineica dell'assemblaggio, \hat{w} è la funzione che rappresenta lo spostamento per ogni punto \hat{z} dell'assemblaggio ad ogni istante di tempo \hat{t} , $\hat{\beta}$ rappresenta la rigidità flessionale, \hat{p} è la pressione ed \hat{R} è il raggio dell'assemblaggio di combustibile¹. Si noti che le grandezze sono tutte adimensionalizzate.

Teoria dell'analisi del segnale

Nell'analisi dei dati sperimentali, la funzione di trasferimento è stata largamente utilizzata. Un breve richiamo teorico è quindi doveroso nonostante la sua fama e i suoi innumerabili utilizzi. La funzione di trasferimento valuta la risposta in frequenza ad un impulso dato in ingresso al sistema in studio. Un assemblaggio di combustibile è fondamentalmente una barra incastrata alle estremità. La scomposizione in modi vibrazionali del moto di oscillazione dell'assemblaggio vede, per ogni modo, una funzione di trasferimento G il cui modulo può essere approssimato a quello per l'oscillatore armonico. Al modo i -esimo corrisponde:

$$|G_i(\omega)| = \frac{1}{m_i \sqrt{(\omega^2 - \omega_i^2)^2 + 4\xi_i^2 \omega_i^2 \omega^2}}$$

dove m_i , η_i e ω_i sono rispettivamente la massa modale, lo smorzamento ridotto e la frequenza naturale al modo i -esimo.

Tale funzione di trasferimento sarebbe valida se l'assemblaggio fosse eccitato a frequenza fissa. Nel caso in esame gli esperimenti sono stati condotti spazzando un range di frequenze tra 0.05 Hz e 25 Hz. In questi casi è più opportuno usare la funzione di correlazione incrociata al posto della funzione di trasferimento. La funzione di cross-correlazione agisce sulle densità spettrali di due segnali ed è paragonabile alla funzione di trasferimento. Tali densità spettrali di potenza dei segnali sono a loro volta la trasformata secondo Fourier del valore di aspettazione dei segnali nel tempo. La correlazione incrociata sarà poi usata per l'analisi dei dati

Tecniche di velocimetria laser

Alcune campagne sperimentali prevedevano lo studio del campo di velocità locale all'interno dell'apparato sperimentale. Un metodo non invasivo per analizzare la

¹È noto che l'assemblaggio di combustibile di un reattore pressurizzato sia a sezione quadrata, tuttavia nel modello semplificato esso viene approssimato a sezione circolare per sfruttare la simmetria cilindrica.

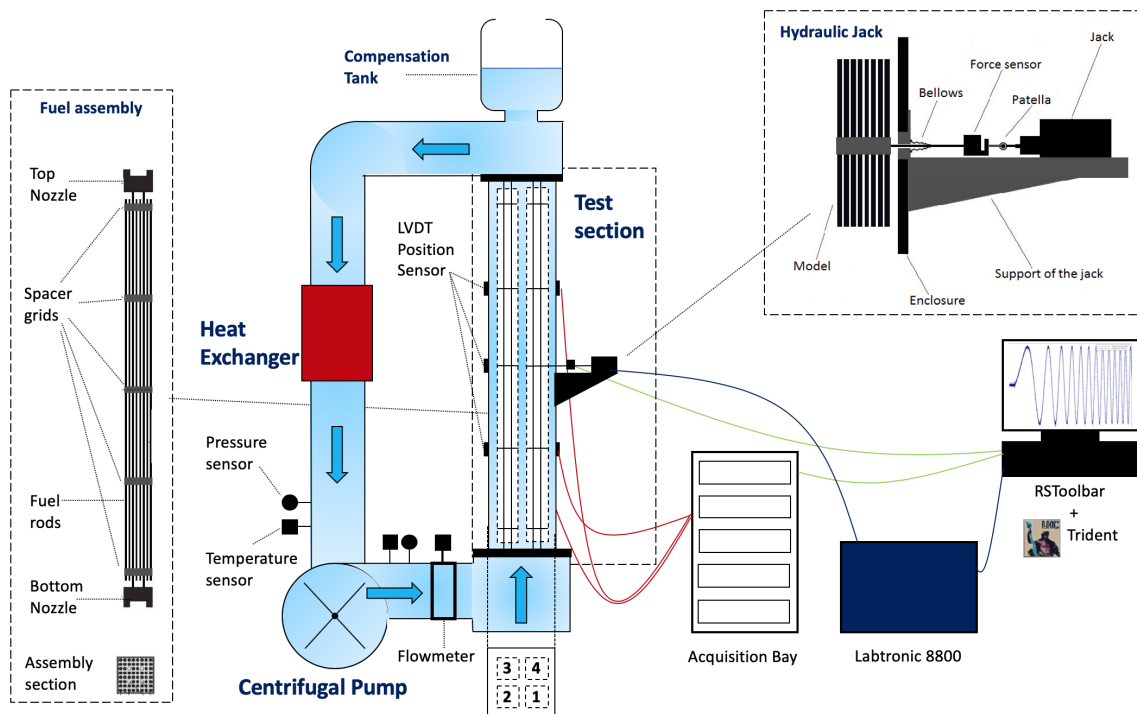


Figura 2: Schema del funzionamento di Icare: una pompa centrifuga mette in moto il flusso d'acqua a velocità imposte, uno scambiatore di calore ne tiene costante la temperatura e gli esperimenti vengono effettuati nella *test section*.

velocità di un flusso, senza appunto condizionarne il comportamento, è dato dalle tecniche di velocimetria ottiche. Nel caso in esame le tecniche utilizzate sono state la LDV, *Laser Doppler Velocimetry*, e la PIV, *Particle Image Velocimetry*. Entrambe prevedono l'utilizzo di un laser e la presenza di particelle all'interno del fluido.

La tecnica LDV prevede l'utilizzo di due fasci laser leggermente sfasati sulla lunghezza d'onda; tali fasci vanno ad illuminare un volume di circa 1 mm^3 nel flusso. Quando le particelle attraversano il volumetto, riflettono la luce inviata dai laser; la luce riflessa viene poi raccolta da un fotorivelatore che riesce a estrapolare la velocità della particella e quindi del fluido.

La tecnica PIV usa il laser ed un apparato ottico per illuminare un piano sottile all'interno del fluido. Un telecamera viene quindi focalizzata su tale piano, atta a registrare il passaggio e la traiettoria delle particelle. Con la tecnica PIV è possibile studiare un piano del flusso, mentre con la tecnica LDV l'indagine sulle velocità è di tipo puntuale.

Descrizione dell'apparato sperimentale

L'apparato sperimentale utilizzato è *Icare expérimental* (Icare). Icare è stato progettato da (Clément, 2014) durante il suo progetto di dottorato nel 2014; esso è un apparato modulare che può ospitare al suo interno fino a 4 assemblaggi di combustibile in scala dimezzata, come mostrato in figura 2.

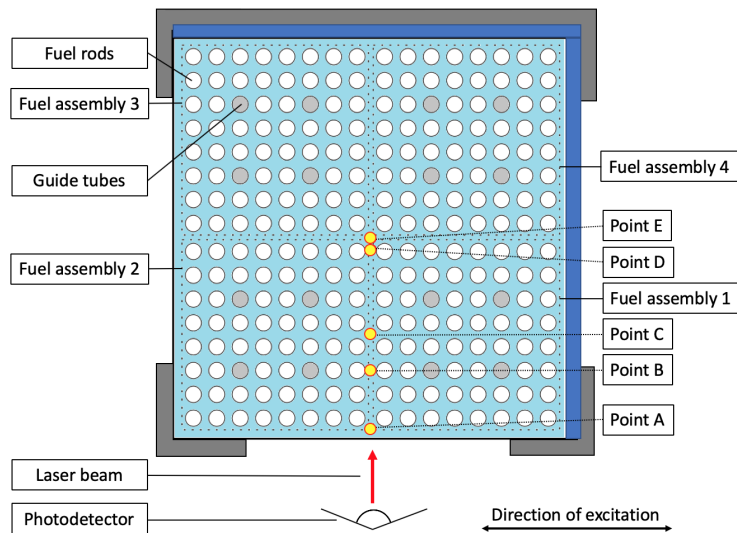


Figura 3: Punti di misura LDV

Ognuno dei 4 assemblaggi in scala dimezzata è formato da 60 cilindri in PMMA e 4 cilindri in acciaio disposti in configurazione quadrata 8x8. I cilindri in PMMA simulano le barre di combustibile mentre gli altri 4 simulano gli alloggiamenti per le barre di controllo e sono saldati a 5 griglie in metallo in cui le barre di PMMA vengono incastrate. Ogni assemblaggio ha una sezione di $10.1 \times 10.1 \text{ cm}^2$, un'altezza di $2,57 \text{ m}$ e ogni barra ha un diametro di 9 mm , quindi molto simile al diametro di una barra reale.

Tramite un pistone idraulico è possibile indurre una vibrazione in un assemblaggio a diverse altezze. Inoltre la sezione sperimentale di Icare è dotata di 24 rivelatori di posizione LVDT (*linear variable differential transformer*), disposti all'altezza delle 3 griglie centrali degli assemblaggi, 6 per ogni facciata di Icare. Dato che gli assemblaggi sono fissati per le estremità all'interno della sezione sperimentale, le griglie in cima ed ai piedi di ogni assemblaggio si possono approssimare come ferme. La disposizione dei 24 rivelatori consente quindi di registrare il movimento di ognuna delle griglie centrali per ogni assemblaggio in ogni direzione. I 4 assemblaggi sono disposti in configurazione 2x2; questa configurazione permette di valutare gli accoppiamenti tra gli assemblaggi quando uno di questi è eccitato dal pistone idraulico

Icare può ospitare 1, 2 o 4 assemblaggi in confinamento largo, 8 mm di spazio in ogni direzione per ogni assemblaggio, o stretto, 4 mm . In configurazione da 1 o 2 assemblaggi, delle lastre vengono aggiunte all'interno della sezione per sostituire gli assemblaggi mancanti.

Su 3 delle 4 pareti della sezione sperimentale di Icare si trovano 4 oblò. In questo modo è possibile condurre delle misure di velocimetria laser sul flusso d'acqua cui sono sottoposti gli assemblaggi. La velocità di tale flusso può arrivare fino a 5 m/s (2 assemblaggi in confinamento stretto), mentre la temperatura può essere portata fino a $30 \text{ }^\circ\text{C}$.

La misura del campo di velocità è stata fatta principalmente tramite LDV. Sono stati individuate due altezze di interesse: livello 1 tra l'altezza della 3^a e della 4^a griglia e livello 2 tra l'altezza della 2^a e della 3^a griglia. Per ogni livello, nello spazio

tra 2 assemblaggi, la velocità è stata misurata in 5 punti diversi: A) tra la parete di Icare e gli assemblaggi, B) all'inizio degli assemblaggi, C) a metà profondità rispetto alla lunghezza dell'assemblaggio, D) alla fine dell'assemblaggio e E) all'inizio dello spazio centrale tra i 4 assemblaggi, come mostrato in figura 3.

Gli esperimenti condotti su Icare prevedevano l'eccitazione ad ampiezza costante di una griglia di un assemblaggio e la misura degli spostamenti delle griglie di tutti gli altri assemblaggi. Per ogni misura, frequenza di oscillazione è stata fatta variare da 0 a 25 Hz .

Sviluppo del codice e analisi dei dati

Il codice computazionale sviluppato rende possibile l'analisi di tutti gli esperimenti dinamici effettuati su Icare. Il codice, sviluppato sulla piattaforma Scilab, è costituito da alcune funzioni che permettono di analizzare i dati sperimentali in base al tipo di studio fisico che si vuole fare. Si possono effettuare studi sui modi di vibrazione degli assemblaggi, studi sull'accoppiamento in qualsiasi direzione e studi sugli esperimenti di velocimetria LDV. Nell'era delle *soft skills*, il vantaggio del software sviluppato consiste nell'aver un'interfaccia grafica molto intuitiva. Questo, insieme alla costruzione del database degli esperimenti condotti su Icare, consente l'analisi dell'enorme quantità di esperimenti effettuati anche quando Icare verrà disabilitato.

Il codice legge in ingresso i segnali dati dai rilevatori di posizione e forza presenti su Icare e i dati registrati tramite LDV, tratta questi dati e ne calcola le funzioni di correlazione incrociate usando un filtro Hann.

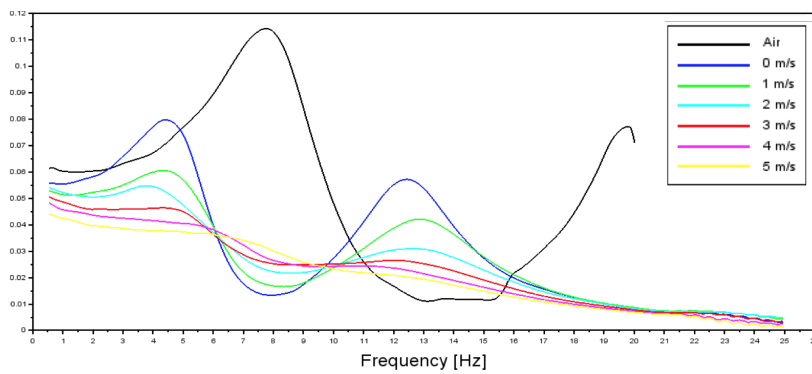
Analisi dei dati

La prime informazioni che si può leggere dall'analisi dei dati sperimentali, sono le variazioni delle frequenze di risonanza, dello smorzamento e della rigidità, in funzione dei diversi parametri sperimentali.

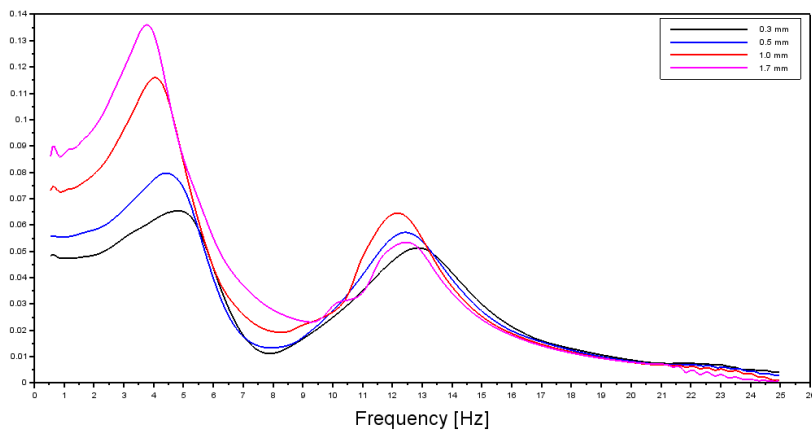
Come già noto in letteratura, la presenza dell'acqua e la sua velocità portano ad una diminuzione dei valori delle frequenze di risonanza e alla presenza di accoppiamento tra gli assemblaggi. Tali frequenze di risonanza del sistema sono state stimate a circa 6, 13 e 20 Hz se l'assemblaggio è in aria, mentre si spostano verso i 4, 8 e 13 Hz in presenza dell'acqua.

Funzione di trasferimento tra spostamento e forza applicata

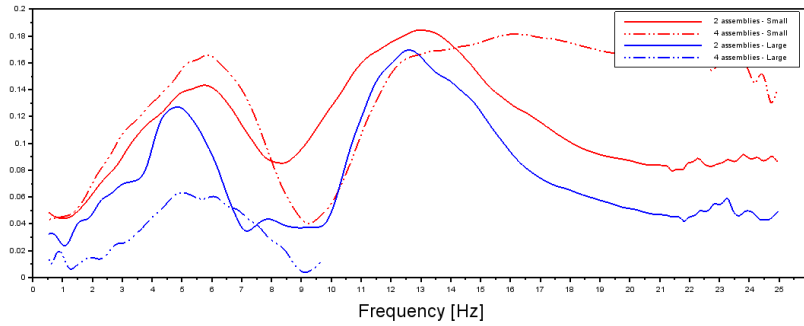
La velocità del flusso cui è sottoposto l'assemblaggio incide notevolmente sulla funzione di trasferimento tra lo spostamento della griglia eccitata e la forza applicata. In figura 4a si può vedere come la presenza dell'acqua trasli le frequenze di risonanza verso valori più bassi. Inoltre i picchi di risonanza diventano sempre meno intensi e più larghi, indicando un progressivo aumento dello smorzamento. A velocità superiori a 3 m/s i picchi diventano quasi indistinguibili. La figura 4b mostra invece esperimenti condotti a diverse ampiezze di eccitazione. Si può vedere che aumentando l'ampiezza di oscillazione, la rigidità e lo smorzamento diminuiscono. La differenza nella forma



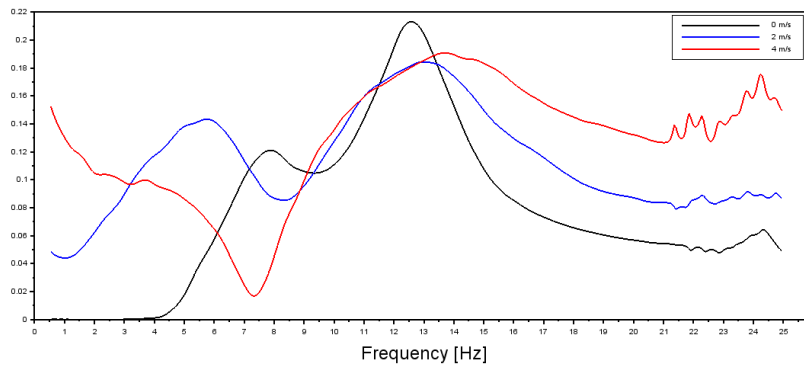
(a) Effetti della velocità su esperimenti condotti con un'ampiezza di eccitazione di 0.5 mm



(b) Effetti dovuti all'ampiezza di vibrazione su esperimenti condotti in acqua stagnante



(a) Effetti dell'intorno sull'accoppiamento



(b) Effetti della velocità sull'accoppiamento

dei picchi delle funzioni di trasferimento dimostra la non linearità del comportamento dell'assemblaggio. Aumentando la velocità del fluido a 5 m/s si nota che le differenze tra le ampiezze di oscillazione diventino impercettibili.

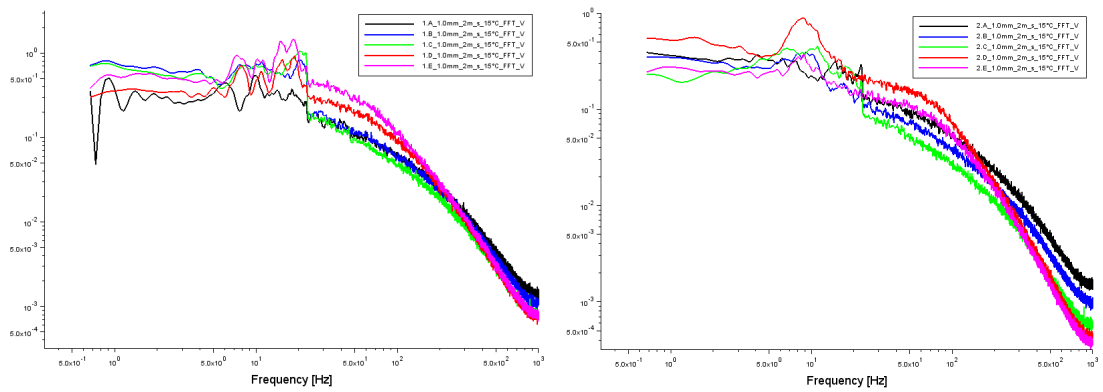
Accoppiamento

Gli effetti più apprezzabili sull'accoppiamento tra gli assemblaggi, sono dati dalla velocità del flusso e dall'intorno circostante l'assemblaggio eccitato. Anche in acqua ferma, si vede un accoppiamento tra gli assemblaggi 1 e 2 dell'ordine del 25% (fatto 100 lo spostamento della griglia eccitata). Tale accoppiamento massimo avviene tra le griglie in basso intorno alla 3^a frequenza di risonanza; questo valore viene portato fino al 40 % per basse frequenze se la velocità del flusso è a 4 m/s .

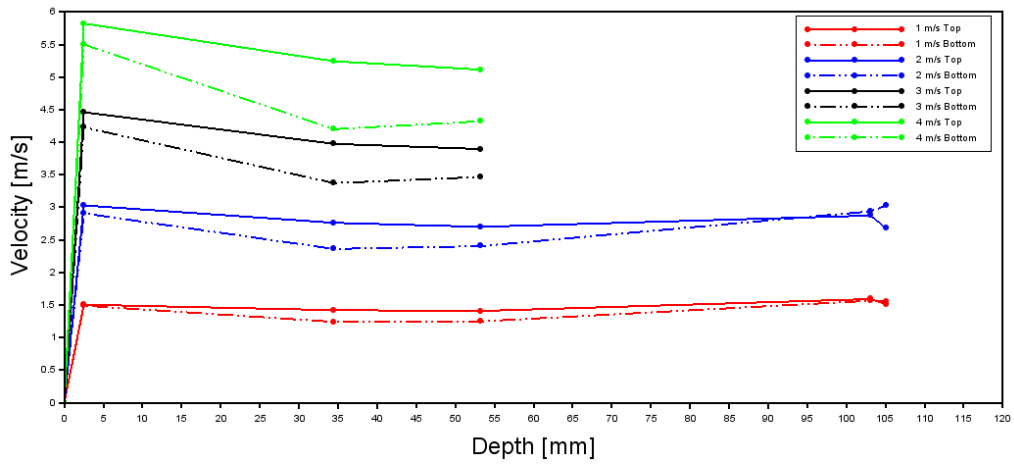
Riguardo l'intorno dell'assemblaggio eccitato, si vede che in configurazione a confinamento largo (8 mm) il numero di assemblaggi non incide significativamente sull'accoppiamento. Al contrario, come mostrato in figura 5a, in confinamento piccolo (4 mm), il numero degli assemblaggi intorno all'assemblaggio eccitato non è trascurabile. In particolare si può vedere come si enunci l'antipicco relativo alla seconda frequenza di risonanza.

Velocimetria Laser Doppler

Tra i risultati della velocimetria laser, in figura 6 vengono mostrati quelli relativi all'andamento della velocità in base all'altezza ed alla profondità di misura. Sia dall'analisi in frequenza (figure 6a e 6b) che dall'analisi in tempo (figura 6c) si può vedere che la velocità tende ad essere maggiore al livello 1 e vicino la parete piuttosto



(a) Livello superiore alla griglia eccitata (b) Livello inferiore alla griglia eccitata



(c)

Figura 6: Paragone tra le densità spettrali di potenza delle velocità a diverse profondità per il livello a)1, b) 2. c) Andamento medio delle velocità rispetto all'altezza ed alla profondità di misura.

che tra gli assemblaggi. Il fatto che sia più elevata vicino alla parete si spiega facilmente considerando il diametro idraulico visto dal fluido: esso è più grande tra gli assemblaggi.

Il fatto che la velocità sia più elevata in alto invece è indice di una proprietà strutturale di Icare. Il flusso d'acqua infatti entra all'interno della sezione dei test proprio da 4 fori posti esattamente sotto gli assemblaggi. Quindi il flusso d'acqua esce dagli assemblaggi e si sposta negli spazi tra gli assemblaggi a maggior diametro idraulico. Questo fa sì che all'aumentare dell'altezza considerata, il flusso d'acqua sia sempre maggiore all'esterno degli assemblaggi che all'interno. Tale comportamento fisico è riscontrabile nel fatto che le velocità misurate hanno un rapporto con le velocità nominali sempre maggiore dell'unità.

Ulteriori effetti sul flusso d'acqua sono dati dall'ampiezza di oscillazione. Dai dati sperimentali risulta che il flusso d'acqua segua delle oscillazioni legate alla vibrazione dell'assemblaggio. Queste sono tanto più evidenti quanto più l'ampiezza di oscillazione è bassa. Aumentando l'ampiezza, l'energia fornita al sistema sarà incanalata nel flusso in maniera sempre più disordinata aumentando l'inefficienza. Quindi all'aumentare dell'ampiezza di eccitazione dell'assemblaggio, la funzione di trasferimento tra velocità misurata e ampiezza imposta diminuirà.

Misure PIV

Misure di velocità con la tecnica PIV non sono state riportate in questo documento. Parte dei risultati PIV saranno proposti al 18° Incontro *NURETH* nell'articolo *TIME-RESOLVED PARTICLE IMAGE VELOCIMETRY BETWEEN TWO PWR SUB-BUNDLES*, di cui l'autore della tesi è coautore.

Contents

Abstract	XXI
Sommario	XXII
1 Introduction	1
1.1 Energy from nuclear reactions	1
1.1.1 Fission reaction	1
1.1.2 Nuclear power plant	2
1.2 Research on nuclear energy at CEA	5
1.2.1 Commissariat à l’Energie Atomique et aux Energies Alternatives	5
1.2.2 Internal structure of the CEA	6
1.3 Internship context	7
1.3.1 Internship goals	8
1.4 Thesis structure	8
2 Theoretical background	11
2.1 PWR core models	11
2.1.1 Core description	11
2.1.2 Core modelization	13
2.2 Simplified model	16
2.2.1 Euler-Bernoulli beam	16
2.2.2 Potential flow	20
2.2.3 Fluid-structure interaction	21
2.3 Signal analysis theory	23
2.3.1 Transfer Function	24
2.3.2 Cross-correlation	25
2.4 Theory on optical velocimetry	27
2.4.1 Laser Doppler Velocimetry	28
2.4.2 Particle Image Velocimetry	29
3 Experimental setup	33
3.1 History of the experimental setups	33
3.1.1 Hermes	34
3.2 Icare expérimental	35
3.2.1 Data acquisition	39
3.3 New configurations	40
3.3.1 Small confinement configurations	40

CONTENTS

3.3.2	Optical velocimetry configuration	42
4	Experimental parameters and computational tools	47
4.1	Objectives of the experimental campaign	47
4.1.1	Experimental parameters	47
4.1.2	Work plan	49
4.2	Code development	50
4.2.1	Acquisition e pre-treatment of the data	52
4.2.2	Hann window	53
5	Data analysis	55
5.1	Transfer function Position/Force	55
5.1.1	Vibrational modes in transfer function peaks	62
5.2	Coupling	62
5.3	LDV	68
5.3.1	Transfer function Velocity/Position	69
5.4	Comments on experimental results	73
6	Conclusions	75
6.1	Conclusions	75
6.2	Future perspectives	76
A	Scilab	79
A.1	Icare_measures.sce	79
A.2	LDV_measures.sce	82
B	Tables of Experiments	83

List of Figures

1.1	PWR power plant scheme	4
1.2	Lab level	6
2.1	Pressurized Water Reactor	12
2.2	Design of Reactor elements: core section and fuel assembly	13
2.3	Simulation of a PWR core	14
2.4	Porous structure model	15
2.5	Bending of Euler-Bernoulli beam	17
2.6	Bending of Euler-Bernoulli clamped-clamped rod	21
2.7	Transfer function scheme	24
2.8	Backscattered LDV scheme	28
2.9	PIV scheme	30
2.10	PIV result in a section plane of a vertical flow	31
3.1	Hermes T	35
3.2	Icare scheme	36
3.3	LVDT Layout on Icare	37
3.4	Icare confinements	38
3.5	Position and force sensors	39
3.6	New elements in Icare	41
3.7	LDV scheme of measurements	43
3.8	PIV scheme: view on the horizontal section from the top.	44
3.9	Photo of Icare test section for PIV	45
4.1	Conceptual maps of experiments.	51
4.2	Reference system for LVDT	52
4.3	Hann window	53
5.1	Force and position signals in time	56
5.2	Transfer function comparison between Large and Small layouts	57
5.3	Different bellows comparison	57
5.4	Confinement comparison	58
5.5	Velocities comparison	59
5.6	Cases for velocity comparisons	60
5.7	Amplitudes comparison	61
5.8	Amplitudes comparison at different velocities	61
5.9	Temperature and number of assemblies comparisons	63

LIST OF FIGURES

5.10	Vibrational mode at resonance frequencies	64
5.11	Coupling on grid level	65
5.12	Coupling with respect to the central grids	65
5.13	Flow velocity and amplitude effects	66
5.14	Neighbourhood effects	67
5.15	Velocity and position signals in time	68
5.16	Comparison on velocity signals in time	69
5.17	PSD of the velocity and the position	69
5.18	Transfer function and coherence	70
5.19	Transfer function for different flow velocities	70
5.20	Transfer function for different amplitude	71
5.21	Comparison of the points of measure	72
5.22	Comparison of velocity PSD	72
5.23	Average behaviour of the velocity with respect to height and depth	73
6.1	Eudore facility	77
A.1	Command window for Icare_measures.sce	80
A.2	Console output with the experimental parameters informations	80
A.3	Icare_measures.sce graphs	81
A.4	LDV_measures.sce command window	82

List of Tables

2.1	Mode shapes and α values	18
3.1	Properties of the experimental facilities	46
4.1	Possible parameters for each experiment in Icare Small layout.	48
4.2	Velocities and LDV points relation in experiments	48
4.3	Temperatures and amplitudes relation in experiments	49
4.4	Parameters relation in PIV measures	50
B.1	Table of Experiments	85
B.2	PIV measurement campaign	89

Abstract

During an earthquake, the fuel assemblies of a PWR (Pressurized Water Reactor) can be set in motion. In the case of high excitation, these movements can cause shocks between the assemblies. In order to create some margin it is necessary to better understand the dynamics of fuel assemblies under axial flow and to have tools to predict the intensity of fuel assemblies vibrations.

The dynamic behaviour of the assemblies is nonlinear. This non-linearity has two origins: the first is due to the internal friction of the structure, and the second is due to the fluid-coupling effects induced by the flow. For nuclear industries it is too expensive, in computational time terms, to explore the behaviour of an entire core dealing with every detail. Thus, the research of simple models that take into account qualitatively or quantitatively some parameters is encouraged.

Simulation or experimental works are needed in order to validate models and to have a better understanding of involved phenomena. In the case of an experimental validation, it is necessary to design a specific setup, calibrate it and conduct the experimental campaigns. The analysis of the collected data is then carried out by means of the implementation of appropriate computational codes.

Concerning fluid-structure interaction, it is important to conduct experiments by recording the data on the dynamics of the assemblies and on the flow velocity to which they are subjected. Different investigation techniques can be used for the speed field: LDV and PIV are non intrusive laser techniques for the analysis of the velocity field punctually (LDV) and in plane (PIV). The motion of the assemblies can be recorded with mechanical motion captors.

The development of computational codes, the records of the experimental data set and its analysis are the focus of this document. The previous experimental setups are illustrated highlighting the strengths and weaknesses. The used setup is called Icare, it consists of 4 half-scale PWR fuel assemblies in a square lattice 2x2. Icare and the modifications made to conduct the experimental campaigns are illustrated in detail. The analysis of the data concern the dependence on some parameters of the dynamic behaviour of the assemblies, the coupling between assemblies and is correlated by the study of the velocity field to which they were subjected.

Keywords: PoliMi, CEA, nuclear engineering, fluid structure interactions, experimental, PWR, coupling, LDV.

Sommario

Durante un evento sismico, gli assemblaggi di combustibile di un PWR sono soggetti a un moto di vibrazione. Tali vibrazioni possono essere abbastanza ampie da portare ad uno scontro tra gli assemblaggi e ad una eventuale deformazione o rottura delle loro griglie. La rottura delle griglie inficia il comportamento meccanico e invalida il funzionamento dell'assemblaggio stesso. È quindi importante riuscire a valutare le forze in gioco e studiare il comportamento dinamico degli assemblaggi.

Un assemblaggio di combustibile ha un comportamento dinamico non lineare a causa dei numerosi punti di attrito presenti tra i cilindri e le griglie che lo costituiscono. Nel core di un reattore gli assemblaggi sono inoltre soggetti ad un flusso d'acqua assiale, che influenza l'interazione tra essi e aumenta la non linearità del comportamento dello stesso assemblaggio. Per l'industria nucleare, studiare il comportamento di un core, tramite un modello che tenga conto minuziosamente di ogni dettaglio, è costoso in termini di tempo computazionale. Quindi è incentivata la ricerca di modelli semplificati che tengano conto qualitativamente o quantitativamente di alcuni parametri.

La validazione di tali modelli può avvenire tramite simulazioni e campagne sperimentali. Nel caso di una validazione sperimentale, bisogna costruire un setup apposito, calibrarlo e condurre le varie campagne. L'analisi dei dati raccolti viene poi effettuata per mezzo di opportuni software computazionali.

Parlando d'interazione fluido struttura è importante condurre esperimenti registrando i dati sulla dinamica degli assemblaggi e sul campo di velocità del flusso cui sono sottoposti. Diverse tecniche di investigazione si possono usare per il campo di velocità; tra le meno invasive la LDV e la PIV sono tecniche laser che permettono un'analisi del campo di velocità puntuale (LDV) e in piano (PIV). Il moto degli assemblaggi si può registrare con dei sensori di movimento meccanici.

Lo sviluppo dei codici computazionali, la raccolta e l'analisi dei dati sperimentali su un setup con 4 assemblaggi in scala dimezzata sono il fulcro di questo documento. I precedenti setup sperimentali sono illustrati evidenziandone i punti di forza e di debolezza. Il setup usato e le modifiche fatte per condurre le campagne sperimentali sono illustrati con maggior dettaglio. L'analisi dei dati è concentrata sulla dipendenza da alcuni parametri del comportamento dinamico degli assemblaggi, sull'accoppiamento tra essi ed è correlata dallo studio del campo di velocità cui gli stessi erano sottoposti.

Parole chiave: PoliMi, CEA, ingegneria nucleare, interazione fluido struttura, sperimentale, PWR, accoppiamento, LDV.

Chapter 1

Introduction

Despite being a Master of science thesis, even though most of the people that will read it know well the subject, I would like to spend a few words describing some basic aspects of nuclear engineering, imagining my parents browsing through it and understanding nothing.

The aim of this chapter is to give the reader basic notions about the general context of the developed project, from the most general physical groundings of nuclear engineering to the purpose of this thesis work. After the general introduction on nuclear fission and nuclear power plants, the chapter introduces the research center and the framework in which my internship took place. Finally, a brief overview of the thesis structure is presented in the last section.

1.1 Energy from nuclear reactions

1.1.1 Fission reaction

Matter is made of atoms: heavy nuclei surrounded by clouds of electrons. The nucleus is composed by nucleons, positively charged protons and uncharged neutrons, while electrons are negatively charged elementary particles. An atom is normally neutral, i.e. it has the same number of protons (called *Atomic Number Z*) and electrons. Different elements are indicated by different *Z*, while elements with the same *Z* but different number of nucleons (called *Mass Number A*) are called *Isotopes*. The isotopes share the same chemical properties but they have different nuclear behaviours.

The nucleus is lighter than the sum of the masses of its components because of the binding energy that holds the nucleons together. Indeed, mass and energy are linked by the square of the light velocity in Einstein's relation:

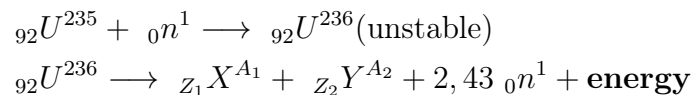
$$E = mc^2$$

This relation allows to treat mass and energy as the same physical quantity: thanks to it can easily be understood why the mass defect of the nucleus and the binding energy among its nucleons are interconnected. Nuclei can be *stable* or *unstable*, depending on the energy of their nucleons, on the mass number *A* and on

the ratio between protons and neutrons. A stable nucleus does not change its nuclear composition in time and its nucleons are in the minimum of the energy level, the *ground state*, while an unstable nucleus verges to a stable configuration by means of a radioactive decay.

For heavy nuclei a more stable configuration of nucleons is obtained whenever the nucleus splits into two parts, i.e. when a fission reaction occurs. The heaviest, most unstable nuclei might therefore be expected to fission spontaneously without external intervention but they do so only rarely. For fission to occur rapidly enough in order to be exploited in nuclear reactors, it is necessary to supply the nucleus with some external energy by means of an induced neutron absorption (Lamarsh & Baratta, 2001).

A neutron colliding with a nucleus may penetrate it: the nucleus excites itself reaching a higher unstable energy level and subsequently splitting in smaller nuclei called fission fragments. The total mass of the fission fragments is smaller than the mass of the initial nucleus: this difference corresponds to the binding energy released in the process of fission. For example, when the isotope U^{235} is shot with a neutron the following fission process occurs:



One of the most used fuel in nuclear reactors is Uranium. Indeed, it is possible to induce a fission reaction on it by using a neutron, obtaining as reaction products fission fragments, 200 *MeV* of energy and an average number of neutrons of 2.43. Since the net neutron balance of the fission reaction is positive, it is possible to establish a self-sustained chain of fission reactions which can be exploited for producing nuclear energy in a controlled way.

To understand why using nuclear energy can be advantageous we can compare three different reactions: supposing that a coal combustion reaction releases 1 arbitrary unit of energy, a methane burning reaction will release 3, while a nuclear fission reaction will give 23000000 (this number is often referred to as *Megafactor*)! For this reason a Uranium pellet of only 5 g in mass used for a fission reactor gives the same energy as 640 *Kg* of wood, 300 m^3 of gases, 400 *Kg* of coal or 350 *Kg* of oil (Ricotti, 2016).

1.1.2 Nuclear power plant

Self-sustained chain

The basic idea behind a Nuclear Power Plant (NPP) is to use a reactor that houses the controlled self-sustained chain of induced fission reactions on Uranium and produces heat, warming up water and producing steam that will be finally used to move an electric generator and produce electricity. The self-sustainability of the fission process depends on the number of neutrons available to induce a fission event at every step in the chain. Indeed, a nuclear reactor can work in three different regimes, identified by the value of the multiplication coefficient k , that is the ratio of the number of neutrons between two consecutively generations in the fission chain:

- subcritical: $k < 1$, the chain reaction cannot be self-sustained, the power generated by the reactor is decreasing and the reactor is shutting down;
- critical: $k = 1$, the chain reaction is self-sustained and the power generated by the reactor is constant in time;
- overcritical: $k > 1$, the chain reaction is more than self-sustained, hence the power is growing in time

Another way to identify this three states is the variable *reactivity* ρ , which is defined as:

$$\rho = \frac{k - 1}{k}$$

According to its values, the reactor's behaviour can be subcritical, critical or overcritical if $\rho < 0$, $\rho = 0$ or respectively $\rho > 0$.

Operating a NPP in steady state means that the net produced power is kept constant in time. This implies that there is the necessity to compensate the variation of reactivity induced by different phenomena such as the nuclear fuel consumption or transmutation effects. Furthermore, if the power produced in the reactor is not kept under control, it could rise at a very high rate, hence it is fundamental to be able to decrease the reactivity. This could be done using some materials whose tendency is to capture neutrons and therefore decrease the value of k . These materials are the main components of the control rods, nuclear reactor elements aimed at stabilizing the reactivity by means of their insertion or extraction in the reactor core.

Pressurized Water Reactor

The nuclear reactor is composed by eight fundamental elements: fuel, moderator, reflector, thermovector fluid, motor fluid, control system, structural system and shields. Avoiding going into unnecessary details, just know that one of the most recognized classification of the reactors is done with respect to the employed moderator, which is the element in the reactor that increases the probability to induce fission events slowing down the neutrons. This classification divides reactors in four groups: moderated by graphite, by water, by heavy water or non moderated (this latest are called *fast reactor* because the neutrons are not slowed down by the moderator). With respect to this kind of classification, most reactors use water as moderator: they are called LWR, Light Water Reactor, where *light* indicates natural water, in contrast with the *heavy* water used in other kinds of reactors. Almost 85 % of approximately 440 operating reactors, are LWR and they are divided into two families: Pressurized Water Reactor (PWR) and Boiling Water Reactor (BWR) in the ratio 70 to 30 (PWR to BWR). The PWR is therefore the most common reactor. Furthermore in the LWR, water acts not only as moderator, but also as reflector and thermovector fluid (Lombardi, 2012).

A simplified way to describe the PWR is illustrated¹ in Fig.1.1. It is composed by two loops: the primary loop, that is radioactive, and the secondary loop that is not. In the primary loop there are the core, where uranium is stored and the fission

¹Graphic by Sarah Harman (Department, 2019)

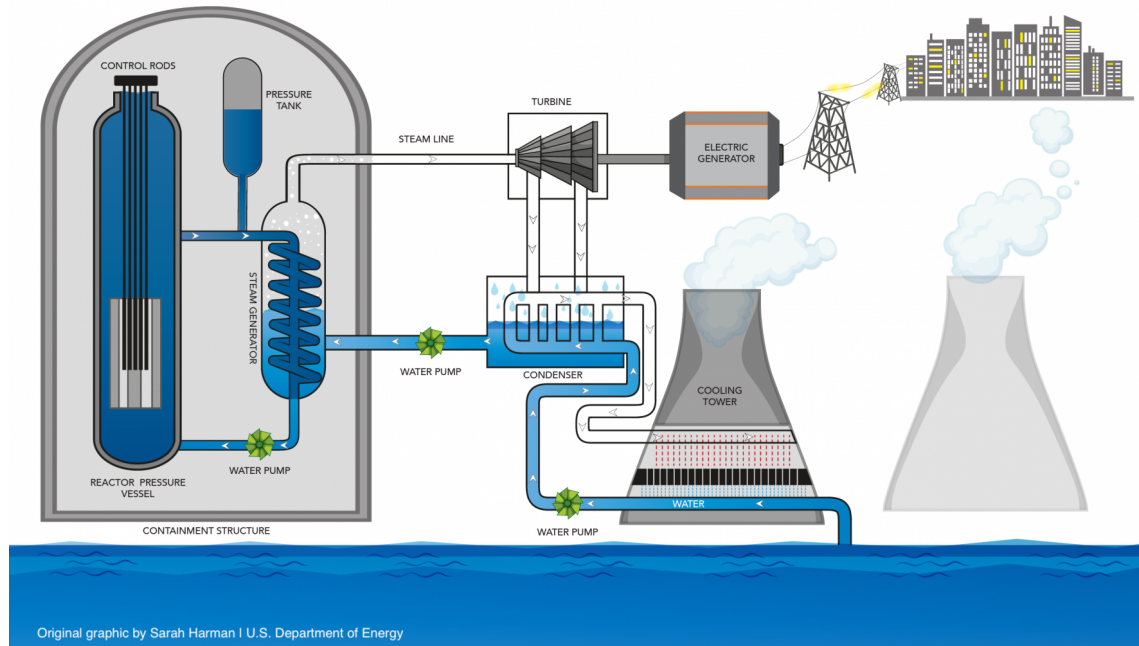


Figure 1.1: PWR power plant scheme.

reactions occur, the pressurizer, that keeps the pressure under a certain threshold, and the steam generator, which is a heat exchanger that receives the hot water at $330\text{ }^{\circ}\text{C}$ and cools it down transferring heat to the secondary loop. The water coming out from the steam generator is at $290\text{ }^{\circ}\text{C}$ and it is streamed to the core by means of a pump. Closing the primary loop, the water cooled in the steam generator is again heated up by the fission in the core. The core consists of groups of fuel rods called assemblies. A better description of a PWR core is in the section 2.1. In the secondary loop the steam generator produces steam by means of the heat transferred from the primary loop. The steam expands in a turbine feeding an electric generator that produces electricity. After the turbine, the steam goes through the condenser, partly returning as liquid water and partly evaporating through the evaporative towers. Since part of the steam mass is lost in the evaporative towers, there is the necessity to reintegrate it, for example by means of a river. Eventually another pump sends the cooled water to the steam generator closing the secondary loop. Further details on nuclear reactions and nuclear plants are available in (Lombardi, 2012; Stephenson, 1958; Lewis, 2008).

The research on new technologies using fission for energy production, is therefore motivated by the desire of improving performance, control and safety in operating a NPP as much as by the desire to deepen the knowledge of the involved physical phenomena. The CEA is one of the main research centers in Europe focusing on nuclear energy.

1.2 Research on nuclear energy at CEA

1.2.1 Commissariat à l’Energie Atomique et aux Energies Alternatives

The CEA (*Commissariat à l’énergie atomique et aux énergies alternatives*) is the French Alternative Energies and Atomic Energy Commission. It is a public body established on the 18th October 1945 by Charles de Gaulle (president of the French Republic in charge at that time) and headed by Frederic Joliot-Curie (High Commissary for Atomic Energy). It was conceived as an organization dedicated to atomic energy and its use for military and civilian purposes (medical applications and electricity generation). In 2010 the Atomic Energy Commission became the Atomic Energy Commission and Alternative Energies, to express the expansion of its field of action on renewable energy. The CEA is active in four areas:

- low-carbon energies (nuclear and renewable),
- defense and security,
- information technologies,
- health technologies.

For each of these fields, the CEA’s mission is to pursue excellent research and to provide support to the industry by maintaining a cross-disciplinary culture of engineers and researchers. Around these main roads, there is a wide variety of projects.

Particularly with regard to the energy framework, the CEA aims at developing new industrial sectors that meet the requirements of safety and environmental protection (minimizing the production of greenhouse gases) and reduction of energy costs. It thus helps to optimize the operation of the current fleet of reactors and to enhance security. Meanwhile, it is involved into international research programs on 4th generation nuclear reactors and into thermonuclear fusion projects, particularly through the ITER project, the first prototype which should demonstrate the scientific and technological feasibility of this energy source. In the field of renewable energy, its work covers mainly the exploitation of solar energy (thermal and photovoltaic), hydrogen and biomass and the development of electric vehicles and biofuels.

Finally, more cross-disciplinary research began to understand the mechanisms of climate changes, control of natural resources, materials, control of environmental impacts of energy technologies, the economics of energy (evolution scenarios, cost analysis, carbon footprint, etc.) and adaptation of networks made necessary by the increasing integration of new energy sources (Capanna, 2014).

The CEA currently operates in nine locations throughout France; civilian research centers are in Paris-Saclay, Grenoble, Marcoule and Cadarache; military centers are located on the sites of the DAM Ile-de-France, Le Ripault, Valduc, Cesta and Gramat. It employs 15 942 employees with an annual budget of about 5 billion euros (data from the end of 2017). It benefits from the strong regional identities of these laboratories and the partnerships forged with other research centers, local authorities and universities.

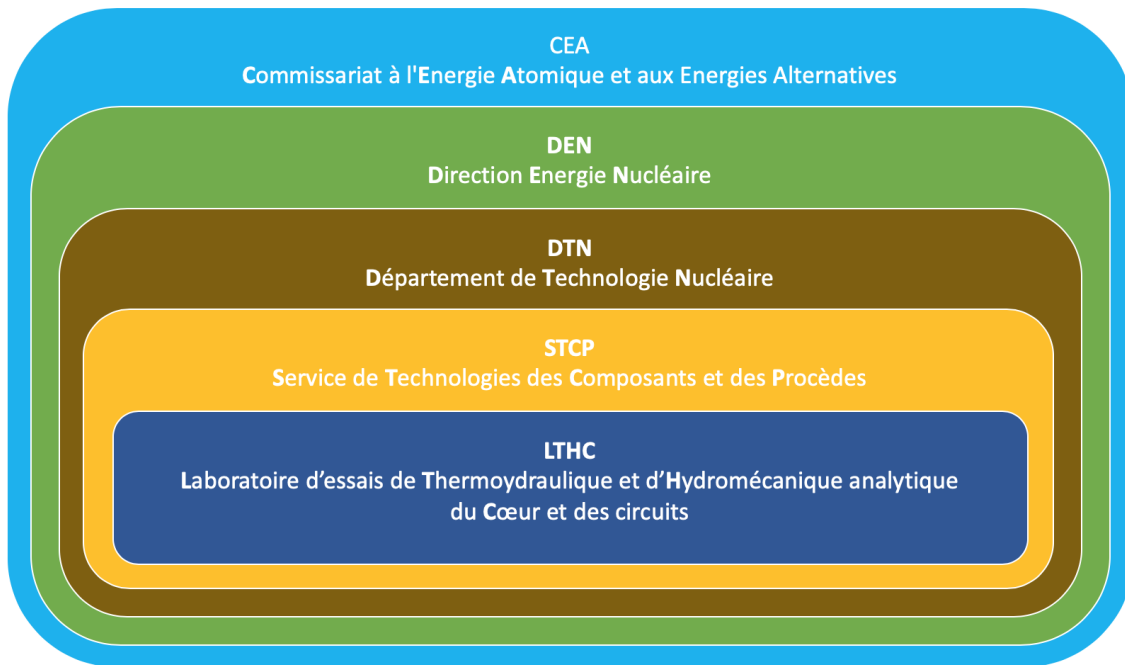


Figure 1.2: Lab level

1.2.2 Internal structure of the CEA

The CEA is constituted by four different directorates:

- DAM - *Direction des Applications Militaires*,
- DEN - *Direction Énergie Nucléaire*,
- DRF - *Direction de la Recherche Fondamentale*,
- DRT - *Direction de la Recherche Technologique*.

This project has been developed in the Laboratory of Thermohydraulic and Hydromechanic experiments on the Core and on the circuits (LTHC: *Laboratoire d'essais de Thermohydraulique et d'Hydromécanique analytique du Cœur et des circuits*), which is part of the Service of Technologies (STCP: *Service de Technologies des Composants et des Procédés*) in the Department of Nuclear Technology (DTN: *Département de Technologie Nucléaire*). The DTN itself pertains to the DEN Directorate. The DEN directorate is dedicated to nuclear energy in all its aspects (energy production, fuel management and optimization, safety, waste management and exhaust fuel re-processing). Within that, the DTN deals with the improvement of water reactors of all types and the development of future reactors. The objective of STCP is to study the components of the core and reactor circuits and to develop processes related to liquid metals, particularly sodium for fourth generation reactors (Boccaccio, 2015).

Within the STCP, the LTHC, directed by J. Peybernès, is born from the previous LHC and has the main mission to study and to qualify experimentally the performances of the components of the core and the circuits of the reactors. In order to carry out its mission, the LTHC has many hydraulic loops and test sections, which

make it possible to recreate the real or simulated conditions of the operation of a PWR. These facilities make it possible to both observe and apprehend the physical phenomena at work within a PWR core, and to qualify the various components of the core (Mokhtari, 2016).

1.3 Internship context

During an earthquake, the fuel assemblies of a PWR core can be set in motion. In the case of high excitation, these movements can cause shocks between the assemblies. Some hot points could be generated, breaking the coating of the fuel assemblies and releasing radioactive products in water. It is important to keep the coating undamaged, since it is the first confinement barrier for radioactive products. Furthermore, if a big shock damages the grids, it could as well compromise the correct operation of the control rods, thus delaying a possible lowering of reactivity. In order to establish some safety margin it is necessary to better understand the dynamics of fuel assemblies under axial flow and to have tools to predict the intensity of fuel assemblies vibrations when set in motion.

The dynamic behaviour of the assemblies is non-linear and this non-linearity has two origins: the first is the internal friction of the structure, while the second is the fluid-coupling effects induced by the flow. A lot of models could be found in literature, both linear and non-linear, but these models are not so much accurate or too complicate to conduct simulations with the typical industrial time.

Fluid-structure interactions have been studied for a long time at CEA. Concerning the experimental point of view, in the last thirty years six setups with different configurations (five of them in LHC) have been studied with the aim to create models for impact forces, fluid effects and the coupling between assemblies when one or more of them are excited. Meanwhile, based on the theory developed by Païdoussis (Païdoussis, 1966), in 2008 G. Ricciardi proposed a new model based on a porous medium approach for modeling the fluid structure interaction in a PWR (Ricciardi, 2008) and his model was validated by three experimental setups: *Echasse*, *Cadix* and *Couplage*. In 2014, S. Clement realized the newest setup *Icare*, that has four half-scale PWR fuel assemblies in a square lattice 2 x 2 (Clément, 2014). Finally, another main setup in LTHC is *Hermès*; with *Hermès* it is possible to conduct experiment on a full scale assembly also in typical PWR operational condition.

It is within this framework that a new tripartite research and development action (CEA-EDF-AREVA) has been carried out at the CEA to study the dynamic behaviour of fuel assemblies under axial water flow. A new PhD project aimed to study a new simplified model has been developed between 2015 and 2018. This model uses the Euler-Bernoulli beam, a particular case of the Timoshenko beam theory, to model the structure (Timoshenko, 1953), while, introduces some approximations to the fluid in order to model it with the potential flow theory. For further informations see (Capanna, 2018).

The present document is the report of the internship that took place in LTHC from January to July 2018, aimed to conduct new experimental campaigns and analyze new data that, merged with older experiments and numerical simulation,

have been used to validate the theoretical model.

These experiments have been performed on Icare, the newest setup (in function from December 2014 to April 2018). The main feature of Icare is to have four fuel assemblies arranged in a 2 x 2 squared lattice. Such configuration allows the study of the coupling effects between assemblies, both aligned and misaligned with respect to the excited one. Indeed, during these tests a grid of a fuel assembly is set in motion by a hydraulic cylinder scanning a range of frequencies so as to excite the three first natural modes of the bending structure. Several displacement sensors are placed along the excited assembly and over the other non-excited assemblies in order to catch the dynamics response of the excited assembly itself and the couplings existing between different fuel assemblies.

1.3.1 Internship goals

The internship has foreseen two main parts: the first objective was to carry out a new experimental campaign on the existing mock-up with different configurations also integrating some laser velocimetry measurements giving information about the velocity fields around the assemblies; in the second part the processing of experimental data from the tests took place.

More in detail we can outline three main objectives:

1. carry out a new experimental campaign on the existing mock-up with different configurations also integrating some laser velocimetry measurements giving information about the velocity fields around the assemblies;
2. developing the code to perform the data analysis from the new experiments;
3. evaluate the overall frequency response of the assemblies with respect to the vibration of the first one: evaluate the coupling between assemblies, the velocity field in the by-passes and proper frequencies of the system

The final intent is to study the described interactions starting literally from mounting the new configuration on the setup.

1.4 Thesis structure

In this chapter the basic principles of fission reactions and nuclear power plant have been presented. The PWR has been shown in a simplified way with its main components. A brief introduction on the CEA and on the LTHC has been made and eventually the internship context has been clarified.

The next chapter deals with the physical background necessary for a good comprehension of the thesis' topic. The PWR core will be illustrated using the models employed to simulate its behaviour with regard to the fluid structure interaction. Theory on signal analysis and laser velocimetry will follow.

In the third chapter an overview on the previous experimental setups and on Icare is presented, making the point on the state of the art. There is a deeper illustration

on Icare and on the methods and procedures used to acquire data. The new installed configurations are described too.

Chapter four concerns experimental parameter: how campaigns have been performed and which were their purposes.

In chapter five the analysis of the recorded data set is proposed. The main experimental results concerning the vibrational mode of the fuel assembly, the coupling with the other and the investigation on the velocity field are illustrated in this chapter, leading to the conclusion and to the future perspectives in the last chapter.

Chapter 2

Theoretical background

This chapter presents the theory of physical and engineering aspects concerning fluid structure interaction in a reactor core. Firstly the PWR core is described, followed by the mathematical derivation of the simplified model in which this work had context. Then theoretical methods for signal analysis and velocimetry techniques are introduced.

2.1 PWR core models

2.1.1 Core description

The PWR core is the part of the reactor that houses the fissile elements (where the fission reactions occur) and consequently heats up the water. The core is situated in the *reactor pressure vessel*, a structure in steel with external diameter of about 5 m, height of 12 m and with walls of thickness up to 0.3 m (Murray & Holbert, 2014). This mighty structure weighs 355 t and is designed to operate with water at 155 bar. Fig.2.1 illustrates¹ the main elements composing the reactor vessel with a zoom on the core barrel, the structure that contains the core in the reactor pressure vessel. On the top of the reactor there is the mechanism enabling action on the control rods. This mechanism is magnetically connected to the control rods and when the magnetic current interrupts the control rods fall vertically straight into the core.

Fuel assemblies The core is composed of about 150÷200 bars called *fuel assemblies* arranged in an approximately cylindrical array as in Fig.2.1. The fuel assembly is the structure that contains the fuel in a typical PWR. This sophisticated fundamental element is designed to optimize the fission chain, to allow the measure of neutron fluxes and the control of the reactivity by means of the movement of the control rods. Indeed, in the pressurized reactors the fuel consists of cylindrical pellets of enriched uranium dioxide (UO₂) about 1.5 cm height and 1 cm wide². These pellets

¹Image from <https://www.britannica.com/technology/pressurized-water-reactor/images-videos>.

²Natural uranium contains different isotopes but only a few percentage of them can sustain the PWR fission chain. For this reason instead of natural uranium, this reactor uses enriched

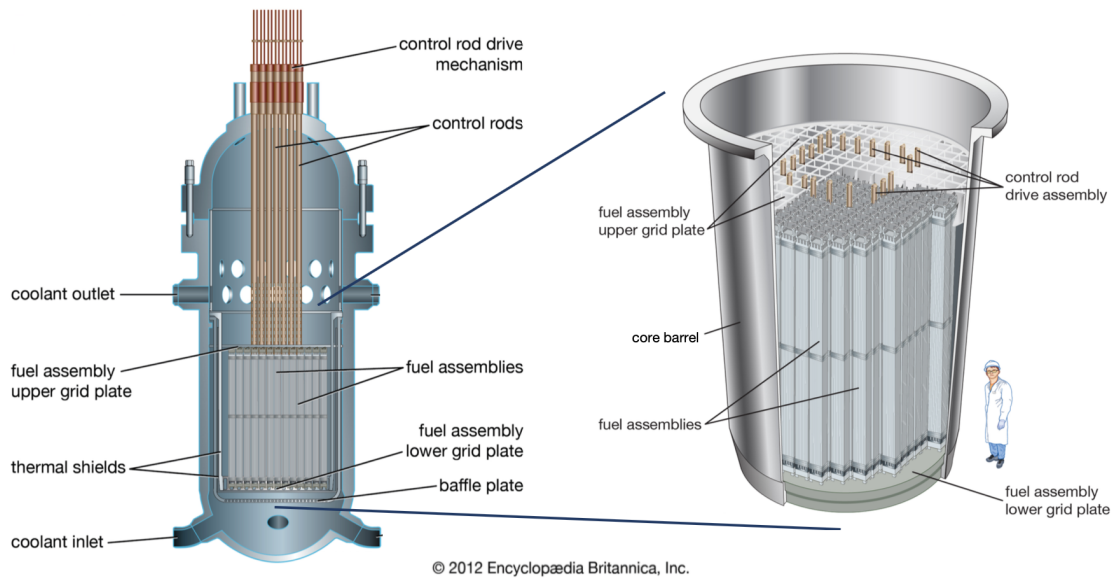


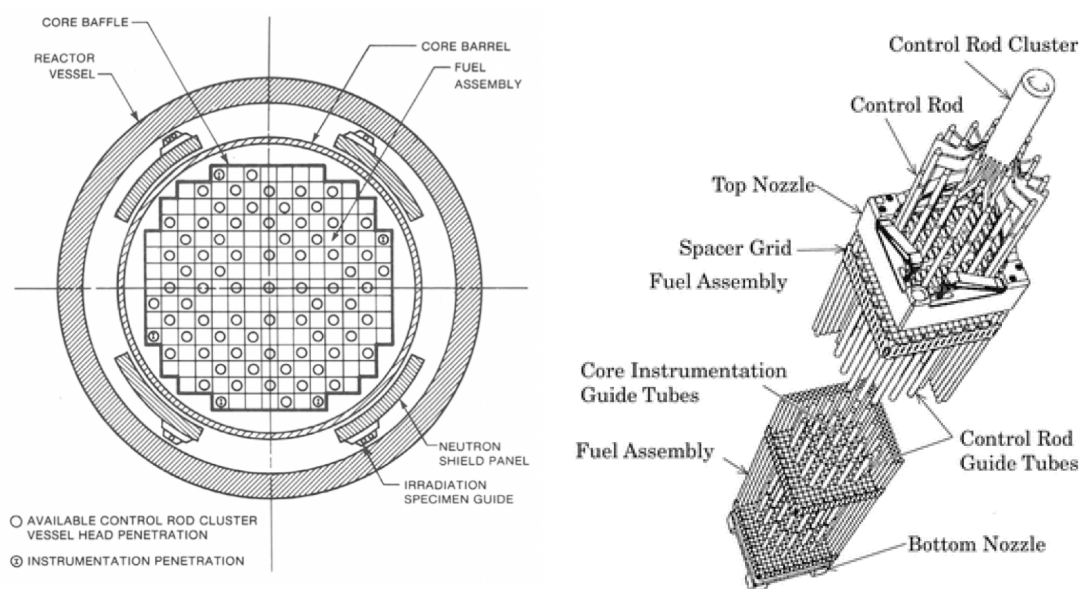
Figure 2.1: The reactor pressure vessel houses the core.

are piled in a column of active height of 365 cm and coated by a zircaloy cylindrical tube 0.6 mm thick. The zircaloy tube is approximately 0.5 m taller than the pellets column and contains other structures for industrial purpose; the height covered only by the uranium pellets is called "active length". This tube is sealed to form the *fuel rod*, thin cylindrical pin with an external diameter of $9.5 \div 10\text{ mm}$ and about 4 m height.

The fuel assembly is obtained assembling 264 fuel rods in a 17×17 square lattice, as shown in Fig.2.2b. The 25 empty rod positions are occupied by the so-called guide tubes, 12 mm wide cylinders designed for a double purpose: keep the assembly aligned and house the control rods or the measurement instruments. The fuel rods are kept separated by about 3 mm gap by means of 8 to 10 spacer grids (depending on the PWR reactor type) placed at different height values along the fuel assembly. At the bottom and at the top there are two nozzles that hold the assembly in its position inside the core. It should be noticed that the control rods cluster is not part of the fuel assembly, as one could think looking at Fig.2.2b: instead, the fuel assembly is designed to house the ensemble of the control rods when it is necessary. Along the approximately 30-year-long operative life of a PWR, fresh fuel assemblies are inserted while the exhausted ones are extracted and stored. Almost once per year, while the reactor is off and flooded, the fuel assemblies are redispersed in order to sustain the fission reactions.

To sum up, in simplicity, the fuel assembly is a 4 m long bar with a square basis of 0.2 m per side, formed by 289 thin rods containing uranium pellets. The core is approximately a square cylinder of 4 m width and height and 86 t weight; it is formed arranging a group from 150 to 200 assemblies, leaving a few millimeters between contiguous assemblies. By means of the fission reactions it produces a thermal power

uranium: the enrichment process brings the weight percentage of U^{235} from 0.7% to a range of $2 \div 5\%$ (Lamarsh & Baratta, 2001).



(a) Horizontal section of the core in a PWR: all the square correspond to a fuel assembly section. (b) Fuel assembly illustrated with its main components.

Figure 2.2: Design of Reactor elements: a) horizontal section of the core; b) design of a fuel assembly.

up to 4500 MW. This heat is transferred to a flux of water at 155 bar with a flow rate up to 1.75 t/s (up to 5 m/s) that enters in the core at 290 °C and gains 30 °C over 4 m; this flow is also highly turbulent, with a Reynolds number $Re = 500000$ at 300 °C.

It should be clear that the core of a nuclear reactor is a very complex structure, so it is difficult to simulate its behaviour without a reliable simplified model.

2.1.2 Core modelization

The safety of Pressurized Water Reactor (PWR) cores subjected to a seismic load is a major concern in the nuclear industry. The core is considered able to work until the grids of the fuel assemblies are not damaged or, more precisely, they are not flared up. Hence, the core is well designed with respect to a seismic event if the estimated forces involved in the shocks between grids do not flare them up. Because of the complexity of the core and of the random character of a seismic event, a fine model of the fuel assemblies is not convenient: performing many simulations with a huge number of structures merged to the fluid structure interaction would take too long with the currently available calculation tools. A simplified model for the fuel assemblies is therefore preferred.

It has been experimentally seen that a fuel assembly has a non linear behaviour with regard to stiffness and damping. These non-linearities are explained either by the bonds between grids and rods or by the presence of the fluid, which introduces an additional stiffness, complex damping, turbulence effects and coupling between the fuel assemblies. Nevertheless, both linear and non-linear models have been developed.

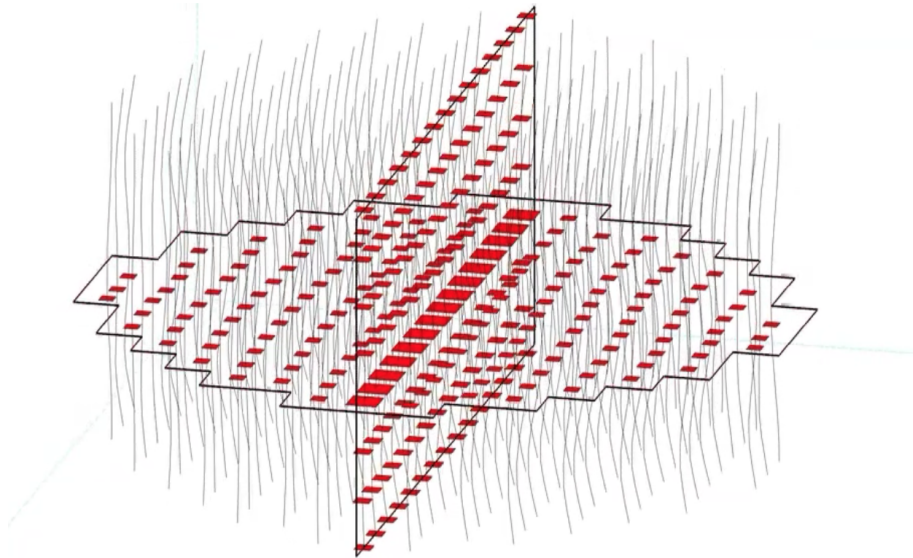


Figure 2.3: Nuclear core simulated under seismic load; grids are represented in red and assemblies by means of lines

Linear and non-linear models Since the fuel assemblies are elongated structures, they have been often represented as a single beam of Euler-Bernoulli type, in which the fluid effects are considered via added mass and damping.

The first studies in literature aimed at modelling the behaviour of a fuel assembly followed a linear approach for simplicity reasons. The behaviour of the assembly can be considered linear until the involved forces are small: in this case the rods are considered to perfectly fit the grids. To better model the physical reality of the problem non linear models have been studied, too. Briefly summing up, theoretical and empirical models have been developed modelling the fuel assembly with one simple Euler-Bernoulli beam, two beams, one for the rods and one for the guide tube, or even more beams. Moreover, models have been studied that either take in account or neglect friction between rods and grids, with either linear or non linear spring simulating the contacts between rods and grids or again models with clamped-clamped or free extremities.

Even if these models can fit some of the experimental results, they present some disadvantages. Indeed, they cannot represent the damping and frequency variation; secondly they can become too complex to be used in industrial simulations or, again, they might need to be adjusted a priori by some parameters. For these reasons they have an only limited usefulness in seismic simulations. Furthermore, all these models do not consider the non-linear effect on the fluid by the structure influenced by the fluid itself and therefore do not allow the presence of the coupling between assemblies.

The state of the art model has been proposed by Ricciardi(2008) taking in account fluid-structure coupling and porous medium theory, improving the simulations and keeping only few degrees of freedom.

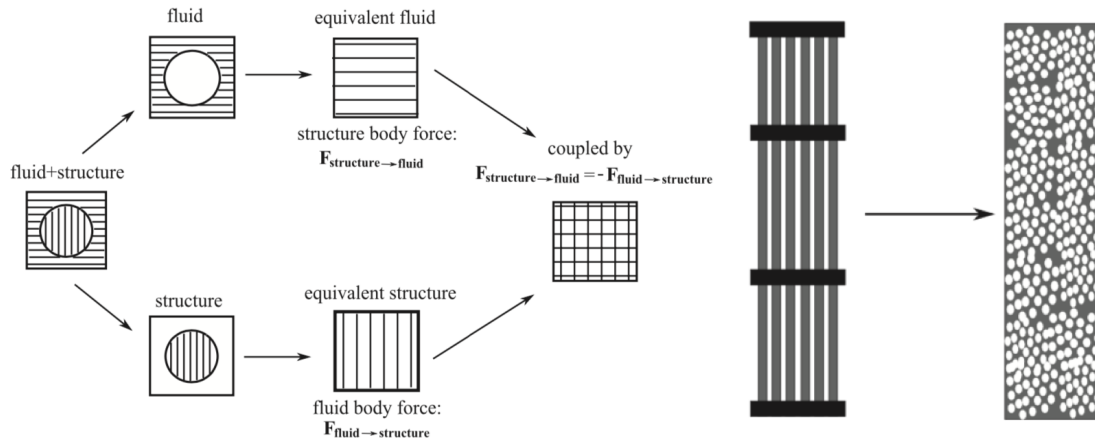


Figure 2.4: Porous structure model and method (Ricciardi *et al.* , 2009)

Porous medium model

Based on the theory of Païdoussis ((Païdoussis, 1966) and (Païdoussis, 2003)), the porous medium approach has been developed following these hypothesis:

1. Viscous, incompressible and Newtonian fluid
2. Negligible gravity effects both on the structure and on the flow
3. Constant cross section of the fuel rod
4. Constant distance between rods in the same fuel assemblies
5. Negligible turbulent kinetics energy with respect to the pressure gradient

This model takes the complexity of the structure (including its nonlinear behaviour determined by around 30 000 contacts in a single fuel assembly) and fluid flow coupling into account. The fluid and the structure are first modelled separately, before being linked together. The equations of motion for the structure are obtained using a Lagrangian approach and, to be able to link up the fluid and the structure, the equations of motion for the fluid are obtained using an Arbitrary Lagrangian Eulerian (ALE) approach. Each rod bundle is modelled in the form of a deformable porous medium; then, the velocity field of the fluid and the displacement field of the structure are defined over the whole domain.

The model transforms a fluid–structure problem with a complex geometry (large number of rods linked by numerous contact friction points) into a problem with a more simple geometry (equivalent beam for each fuel assembly). Therefore it permits to simulate both the fluid and the structure dynamics of a whole core taking few degrees of freedom. The model lost some local information compared to a direct numerical simulation, such as vibrations of rods into grids, but it holds informations on interactions between fuel assemblies, via fluid or contacts. For example the effects of an external excitation, such as an earthquake, on the impact forces between fuel assemblies can be simulated. Accordingly to Païdoussis theory, the model also

predicts instability; these are at fluid velocities greater than 33.9 m/s and since in reactor operating conditions the velocity is about 5 m/s, there is no risk that instability occurs in practice.

The porous medium method permits to model a fuel assembly with only a few degrees of freedom, thus the core with its large number of fuel assemblies can be simulated. To deepen the knowledge on this topics see (Ricciardi, 2008) and (Ricciardi *et al.*, 2009).

2.2 Simplified model

As already explained in section 1.3, this work falls into a PhD project aimed at reducing the computational time for a PWR core under seismic load (Capanna, 2018). The porous medium approach still has long characteristic time, hence there is the necessity of a simpler model. The simplified theoretical model beyond the PhD project is here presented.

This model describes the structures as Euler-Bernoulli beam while adds 2 new hypothesis in the modelization of the flow; indeed the flow is modelized as *irrotational* and *inviscid*.

2.2.1 Euler-Bernoulli beam

Modeling the assembly as the Euler-Bernoulli beam, the following assumptions must be made:

1. the length of the bar is higher with respect to the thickness;
2. each rod cross-section undergoes the same transverse deflection;
3. the bending due to its own weight is neglected;
4. the material behaves linearly;
5. the deflection are small compared to the beam thickness

The bending of a bar of length L is represented in Fig.2.5. The transverse displacement at any point x and time t is denoted $w(x, t)$, the transverse force per unit length is $f(x, t)$, while the mass per unit length is $m(x)$ and the flexural rigidity³ is $EI(x)$. Consideration of the equilibrium of the forces and moments, with the inclusion of the viscous damping per unit length c , leads to the governing differential equation of motion:

$$\frac{\partial^2}{\partial x^2} \left(EI(x) \frac{\partial^2 w}{\partial x^2} \right) + m(x) \frac{\partial^2 w}{\partial t^2} + c(x) \frac{\partial w}{\partial x} = f(x, t) \quad (2.1)$$

Aiming at studying the linear behaviour of the continuous system, an elegant method is the mode superposition technique. In order to apply it the knowledge of the natural frequencies (i.e. the frequencies around which resonances can occur) and the corresponding mode shapes is needed.

³The flexural rigidity EI is the product between the Young's modulus and the second order area inertial momentum for the cylinder $I = \frac{1}{4}\pi R^4$

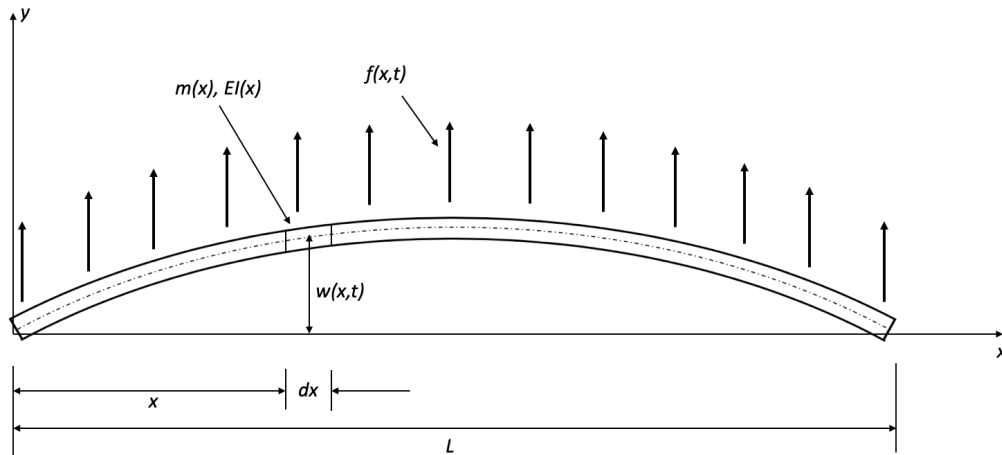


Figure 2.5: Bending of Euler-Bernoulli beam

Natural frequencies and mode shapes

Natural frequencies and mode shapes are obtained considering the homogeneous solution of the beam vibration equation, hence without the external load. In the case of interest, the undamped mode in bending vibration of the beam with uniform sectional property (flexural rigidity and linear mass) is considered. The equation 2.1 becomes:

$$EI \frac{\partial^4 w}{\partial x^4} + m \frac{\partial^2 w}{\partial t^2} = 0 \quad (2.2)$$

Assuming that for free vibration the response w is given by:

$$w(x, t) = \varphi(x) \sin \omega t \quad (2.3)$$

Where $\varphi(x)$ is the mode shape function and ω is the circular natural frequency. Therefore equation 2.2 becomes:

$$\frac{\partial^4 \varphi}{\partial x^4} + \alpha^4 \varphi = 0 \quad \text{with } \alpha^4 = \frac{m\omega^2}{EI} \quad (2.4)$$

The general solution of 2.4 is:

$$\varphi(x) = A \sin \alpha x + B \cos \alpha x + C \sinh \alpha x + D \cosh \alpha x \quad (2.5)$$

where A , B , C , and D are integration constants to be evaluated from the boundary conditions. In our case of interest the boundary conditions are those of the clamped-clamped beam case:

$$\begin{aligned} \varphi(0) &= 0 & \varphi(L) &= 0 \\ \varphi'(0) &= 0 & \varphi'(L) &= 0 \end{aligned}$$

which leads to the non trivial solution:

$$\cos \alpha L \cosh \alpha L = 1$$

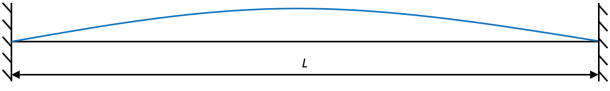
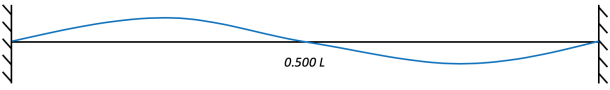
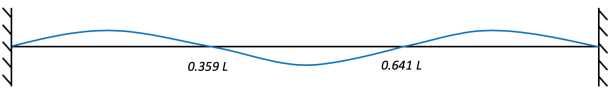
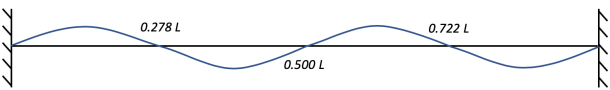
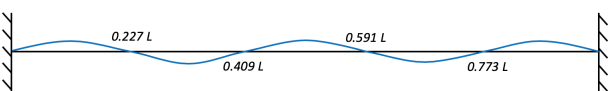
n	$\alpha_n L$	β_n	Mode shape
1	4.730042	0.98250221	
2	7.853203	1.00077731	
3	10,99561	0.99996645	
4	14,13716	1.00000145	
5	17,27876	0.99999994	

Table 2.1: Mode shapes and α values for the Euler beam at the first five proper frequencies

This transcendental equation has infinite solutions, which can be calculated numerically and that can be represented by α_n , where n indicates the n^{th} mode. In Table 2.1 the first five values are shown with the relative mode shapes, calculated by (Capanna, 2018). Defining $\beta_n = \frac{\cos \alpha_n L - \cosh \alpha_n L}{\sin \alpha_n L + \sinh \alpha_n L}$, the solution for the displacement, called *Mode Shape Functions*, is obtained:

$$\varphi_n(x) = A(\sin \alpha_n x - \sinh \alpha_n x + \beta_n(\cos \alpha_n x - \cosh \alpha_n x))$$

where A is a parameter depending on initial conditions. It is usually set to the unity, thus a multiplication constant will appear in the time dependent function, which will be determined by using boundary conditions.

Once the α_n coefficients are numerically calculated, from their definition it is possible to obtain the natural frequencies:

$$\omega_n = \alpha_n^2 \sqrt{\frac{EI}{m}} \quad (2.6)$$

The most important property of the normal modes is that of orthogonality. This property makes possible the uncoupling of the equations of motion for different modes.

Normal modes satisfy the following equations:

$$\begin{aligned} \int_L m(x)\varphi_n(x)\varphi_m(x)dx &= \begin{cases} 0 & \text{for } n \neq m \\ M_n & \text{for } n = m \end{cases} \\ \int_L \frac{d^2}{dx^2} \left[EI(x) \frac{d^2\varphi_n(x)}{dx^2} \right] \varphi_m(x)dx &= \begin{cases} 0 & \text{for } n \neq m \\ K_n & \text{for } n = m \end{cases} \end{aligned}$$

where M_n and K_n are respectively the modal mass and the modal stiffness of the n^{th} mode.

Adding external load

It is now possible to take into account the external load and solve the equation 2.1. The transverse displacement of the beam under external load can be written using a generic time-dependent coefficient for the mode n^{th} $\eta_n(t)$ and assuming that the distributed external load $f(x, t)$ can be expressed as a function of the modes shapes:

$$w(x, t) = \sum_{n=1}^{\infty} \varphi_n(x)\eta_n(t) \qquad f(x, t) = \sum_{n=1}^{\infty} \varphi_n(x)f_n(t)$$

The equation 2.1 becomes:

$$\sum_{n=1}^{\infty} \left[\frac{d^2}{dx^2} \left(EI(x) \frac{d^2\varphi_n(x)}{dx^2} \right) \eta_n(t) + c(x)\varphi_n(x)\dot{\eta}_n(t) + m(x)\varphi_n(x)\ddot{\eta}_n(t) \right] = \sum_{n=1}^{\infty} \varphi_n(x)f_n(t) \quad (2.7)$$

Multiplying on both sides equation 2.7 by the k^{th} mode shape, integrating in the domain of the beam and applying orthogonality condition of normal modes and assuming that orthogonality holds for viscous damping too, the partial differential equation of motion can be transformed into a collection of uncoupled ordinary differential equations of motion:

$$\ddot{\eta}_k(t) + 2\varepsilon_k\omega_k\dot{\eta}_k(t) + \omega_k^2\eta_k(t) = Q_k(t) \quad (2.8)$$

where ε_k is the modal damping ratio and Q_k is the generalized force for the k^{th} mode; assuming as in the most cases that linear mass m , flexural rigidity EI and viscous damping c do not vary along the beam, it is possible to express the 2 as:

$$\varepsilon_k = \frac{1}{2\omega_k} \frac{c}{m} \qquad Q_k(t) = \frac{1}{m} f_k(t)$$

For deeper knowledge, these calculations can be found in (Talukdar, 2016) and (Capanna, 2018)

2.2.2 Potential flow

Assuming high Reynolds values, the strong hypothesis of irrotational and inviscid flow are made in order to reduce the complexity of the model. The only assumption for the irrotational flow leads to identify a potential for the fluid, for which its gradient corresponds to the velocity field of the fluid itself. Therefore, this assumption reduces the dependency of the velocity vector field on one scalar potential.

$$\nabla \wedge \mathbf{v} = 0 \quad \longrightarrow \quad \mathbf{v} = \nabla \phi$$

Then, for incompressible fluid, the divergence of the velocity is null:

$$\nabla \cdot \mathbf{v} = 0 \quad \longrightarrow \quad \nabla^2 \phi = 0 \quad (2.9)$$

this implies that to describe the velocity field and the related quantities, the Laplacian equation 2.9 should be solved. Since this work concerns rods, it is advisable to rewrite it in cylindrical coordinates:

$$\nabla^2 \phi = \frac{1}{r} \frac{\partial}{\partial r} \left(r \frac{\partial \phi}{\partial r} \right) + \frac{1}{r^2} \frac{\partial^2 \phi}{\partial \theta^2} + \frac{\partial^2 \phi}{\partial z^2} = 0 \quad (2.10)$$

Laplace equation is linear, hence the superposition of different potential flows is still a potential flow. There are applications of potential flow theory in every field concerning not only fluids, but also aerodynamics, space, nautical, energy, nuclear and even biology, that uses potential flow theory to describe for example the locomotion of fishes (Lighthill, 1960) and birds or the blood flow in veins.

Linearized Bernoulli equation

Since Laplace equation is differential, it needs boundary conditions to be solved. The boundary conditions are also known in terms of pressure distribution on the boundaries of the problem. Thus, fluid mechanics equations relating the pressure distribution to the velocity potential are needed: they can be derived from the general Navier-Stokes momentum balance equation.

The Navier-Stokes equation for incompressible (naming τ the stress tensor $\nabla \cdot \underline{\tau} = \mu \nabla^2 \mathbf{v}$) and inviscid fluid ($\mu = 0$), with no external forces ($F = 0$) acting on it and neglecting gravitational effect, becomes the Bernoulli equation:

$$\rho \frac{D\mathbf{v}}{Dt} = -\nabla p + \rho F + \mu \nabla^2 \mathbf{v} \quad \longrightarrow \quad \rho \frac{D\mathbf{v}}{Dt} = -\nabla p \quad (2.11)$$

where $\frac{D}{Dt}$ is the material derivative $\frac{D}{Dt} = \frac{\partial}{\partial t} + \mathbf{v} \cdot \nabla$. The Bernoulli equation for potential flow thus is obtained from the equation 2.11 with potential flow hypothesis:

$$\frac{\partial \mathbf{v}}{\partial t} + \frac{1}{2} \nabla \|\mathbf{v}\|^2 = -\frac{\nabla p}{\rho} \quad \longrightarrow \quad \nabla \left(\frac{\partial \phi}{\partial t} + \frac{1}{2} |\nabla \phi|^2 \right) = -\frac{\nabla p}{\rho} \quad (2.12)$$

where the irrotational hypothesis allows to write $\mathbf{v} \cdot \nabla \mathbf{v} = \frac{1}{2} \nabla \|\mathbf{v}\|^2$

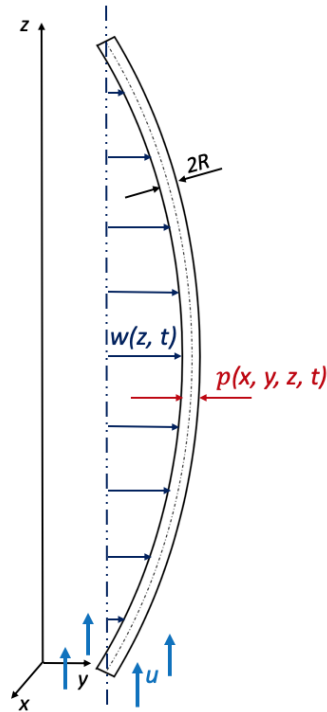


Figure 2.6: Bending of Euler-Bernoulli clamped-clamped rod subjected by an axial flow u

It is now possible to assume that the variation of the velocity can be decomposed in a steady term and in a perturbation term: $\mathbf{v} = \mathbf{v}_\infty + \mathbf{v}'$. The linearization of all the terms is possible since potential flow theory assumes the linearity of the equations; hence also p and ϕ can be decomposed: $p = p_\infty + p'$ and $\phi = \phi_\infty + \phi'$. In this condition the quadratic term in Bernoulli equation for potential flow becomes:

$$|\nabla\phi|^2 = |\nabla(\phi_\infty + \phi')|^2 = |\nabla\phi_\infty|^2 + |\nabla\phi'|^2 + 2\nabla\phi_\infty \cdot \nabla\phi'$$

Therefore it is possible to linearize to the first order the Bernoulli equation for potential flow, neglecting the second order term $|\nabla\phi'|^2$, obtaining:

$$\frac{\partial\phi'}{\partial t} + \nabla\phi_\infty \cdot \nabla\phi' = -\frac{p'}{\rho} \quad (2.13)$$

Since fluid and structure equation have been described, It is possible to state the fluid-structure interaction problem.

2.2.3 Fluid-structure interaction

In 2.2.1 there is the equation that models the displacement of the structure, while in 2.2.2 the problem of the fluid has been stated. In this case of interest, the linear mass and the flexural rigidity are constant along the length of the beam and viscous and gravitation effect are neglected. Potential flow theory has been taken in account.

Merging the two models, it is possible to link the displacement $w(z, t)$ to the force f^y acting on the structure and to express f^y as the resultant of the forces between

Chapter 2. Theoretical background

the liquid and the structure on the y direction as it is shown in Fig. 2.6. These forces can be expressed in function of the pressure field p , hence the equation 2.1 becomes:

$$m \frac{\partial^2 w(z, t)}{\partial t^2} + EI \frac{\partial^4 w(z, t)}{\partial z^4} = \underbrace{\int_0^{2\pi} p(R, \theta, z, t) \sin \theta R d\theta}_{f^y(z, t)} \quad (2.14)$$

In order to have a general formulation, all the physical quantities are made dimensionless using the cylinder length L as typical length and the flow velocity u as typical speed:

$$\begin{aligned} \hat{R} &= \frac{R}{L} & \hat{r} &= \frac{r}{L} & \hat{x} &= \frac{x}{L} & \hat{y} &= \frac{y}{L} & \hat{z} &= \frac{z}{L} \\ \hat{t} &= \frac{u \cdot t}{L} & \hat{l}_x &= \frac{l_x}{L} & \hat{l}_y &= \frac{l_y}{L} & \hat{w} &= \frac{w}{L} & \hat{p} &= \frac{p}{\rho u^2} \end{aligned}$$

where l_x and l_y are respectively the distances from the rod to the wall on x and y directions. Then defining

$$\hat{m} = \frac{m}{\rho L^3} \quad \hat{\beta} = \frac{EI}{\rho u^2 L^4} \quad \hat{f}^y = \frac{f^y}{\rho u^2 L}$$

a dimensionless formulation of the 2.14 is obtained:

$$\hat{m} \frac{\partial^2 \hat{w}(\hat{z}, \hat{t})}{\partial \hat{t}^2} + \hat{\beta} \frac{\partial^4 \hat{w}(\hat{z}, \hat{t})}{\partial \hat{z}^4} = \hat{f}^y(\hat{z}, \hat{t})$$

From the fluid point of view, the bulk flow is equal to u in z direction $\mathbf{v}_\infty = u \mathbf{1}_z$; hence it is possible to rewrite differential product $\nabla \phi_\infty \cdot \nabla \phi' = u \partial_z \phi'$. The linearized Bernoulli equation 2.11 can be rewritten in dimensionless form:

$$\hat{p}(\hat{x}, \hat{y}, \hat{z}, \hat{t}) = -(\partial_{\hat{t}} + \partial_{\hat{z}}) \hat{\phi} \quad (2.15)$$

with $\hat{\phi} = \frac{\phi}{uL}$.

Therefore, it is clear that the fluid-structure interaction problem is reduced to find $\hat{\phi}$ solving the Laplacian equation with its proper boundary condition. These are given by the impermeability condition (the fluid has the same normal velocity as the structure):

$$\begin{cases} \nabla^2 \hat{\phi} = 0 \\ \frac{\partial \hat{\phi}}{\partial \hat{y}} \Big|_{\hat{y}=\hat{l}_y} = \frac{\partial \hat{\phi}}{\partial \hat{x}} \Big|_{\hat{x}=\hat{l}_x} = 0 \\ \frac{\partial \hat{\phi}}{\partial \hat{y}} \Big|_{\hat{r}=\hat{R}} = -(\partial_{\hat{t}} + \partial_{\hat{z}}) \hat{w}(\hat{z}, \hat{t}) \sin \theta \end{cases}$$

Applying $(\partial_{\hat{t}} + \partial_{\hat{z}})$ to the previous equations and using equation 2.15, a Laplace problem with Neumann boundary conditions describing the pressure field is finally obtained:

$$\begin{cases} \nabla^2 \hat{p} = 0 \\ \left. \frac{\partial \hat{p}}{\partial \hat{y}} \right|_{\hat{y}=\hat{l}_y} = \left. \frac{\partial \hat{p}}{\partial \hat{x}} \right|_{\hat{x}=\hat{l}_x} = 0 \\ \left. \frac{\partial \hat{p}}{\partial \hat{y}} \right|_{\hat{r}=\hat{R}} = -(\partial_{\hat{t}} + \partial_{\hat{z}})^2 \hat{w}(\hat{z}, \hat{t}) \sin \theta \end{cases} \quad (2.16)$$

Closure of the model

The coupling between the two models (fluid and structure) happens due to two terms: the pressure term p and the displacement term w . Both terms are present either in the structure equation and in the fluid system 2.17.

Fluid-structure interaction can be studied. The presence of interactions between fluid forces (by mean of the pressure term) and structure forces means that the behaviour of the structure is going to influence the behaviour of the fluid and vice versa. Thus, the set of equations should be solved in an iterative way.

$$\begin{cases} \hat{m} \frac{\partial^2 \hat{w}(\hat{z}, \hat{t})}{\partial \hat{t}^2} + \hat{\beta} \frac{\partial^4 \hat{w}(\hat{z}, \hat{t})}{\partial \hat{z}^4} = \int_0^{2\pi} \hat{p} \sin \theta \hat{R} d\theta \\ \nabla^2 \hat{p} = 0 \\ \left. \frac{\partial \hat{p}}{\partial \hat{y}} \right|_{\hat{y}=\hat{l}_y} = \left. \frac{\partial \hat{p}}{\partial \hat{x}} \right|_{\hat{x}=\hat{l}_x} = 0 \\ \left. \frac{\partial \hat{p}}{\partial \hat{y}} \right|_{\hat{r}=\hat{R}} = -(\partial_{\hat{t}} + \partial_{\hat{z}})^2 \hat{w}(\hat{z}, \hat{t}) \sin \theta \end{cases} \quad (2.17)$$

The resolution of the system is out of the context of this work. The resolution process shifts the problem to the Fourier space in order to study the modal decomposition of the structure vibrations and to identify some parameters (e.g. the added mass coefficient or the natural frequencies) useful to characterize the structure behaviour. The research of these parameters on the experimental results will provide the accuracy of the model. The previous calculations and the resolution of the system 2.17 can be found in (Capanna *et al.*, 2017; Capanna, 2018).

2.3 Signal analysis theory

In order to analyse the experimental results, it is necessary to understand the phenomenon of resonance of fuel assemblies and, more in general, the behaviour of the assembly answering to an input. The transfer function correlates the output and the input of a dynamic system in the frequency domain. Defining $u(t)$ and $y(t)$ the input and the output of a system depending on the time variable, and naming $U(\omega)$ and $Y(\omega)$ their duals in frequencies domain, the transfer function $G(\omega)$ is:

$$G(\omega) = \frac{\tilde{y}(\omega)}{\tilde{u}(\omega)} \quad (2.18)$$

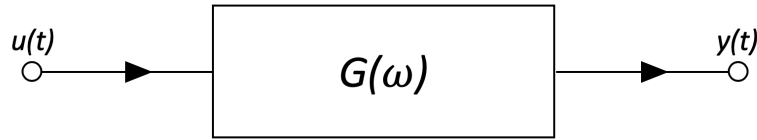


Figure 2.7: Transfer function scheme: every input $u(t)$ to the system gives an output $y(t)$ calculable by means of the transfer function $G(\omega)$.

Studying the behaviour of a dynamic system, it is fundamental to know its transfer function, in order to predict its answer to any input.

2.3.1 Transfer Function

Imaging to study a dynamic linear system, the simplest and most recurring in literature is the harmonic oscillator.

Naming $x(t)$ the displacement of the harmonic oscillator from its steady state position imposed by an external force $f(t)$, the following differential equation governs its forced motion:

$$m\ddot{x}(t) + c\dot{x}(t) + kx(t) = f(t) \quad (2.19)$$

Here m , k and c are respectively the oscillator's constant mass, stiffness and damping. Thus, the output of the system can be the displacement $x(t)$ due to the external force $f(t)$ given as input. Furthermore, equation 2.19 is a linear differential equation, thus the superposition principle can be applied.

The usual convention sees $x(t)$, $u(t)$ and $y(t)$ respectively the state, the input and the output of a system. Thus, concerning this discussion, it is useful to rename the variables:

$$\begin{aligned} f(t) &\implies u(t) \\ x(t) &\implies y(t) \\ m\ddot{x}(t) + c\dot{x}(t) + kx(t) = f(t) &\implies m\ddot{y}(t) + c\dot{y}(t) + ky(t) = u(t) \end{aligned} \quad (2.20)$$

The input $u(t)$ is the external force that excites the system, which responds moving with a displacement in output governed by the function in time $y(t)$.

Fourier's theorem states that any waveform in the time domain can be represented by the weighted sum of sines and cosines. The Fourier transform deconstructs a time domain representation of a signal into the frequency domain representation. It is a different way to look at the same signal. The Fourier transform $\mathcal{F}\{y(t)\}$ for a generic function $y(t)$ is:

$$\mathcal{F}\{y(t)\} = \tilde{y}(\omega) = \int_{-\infty}^{\infty} y(t)e^{-i\omega t} dt \quad \omega \in \mathbb{R}$$

and the same holds for $u(t)$. Thanks to the properties of the Fourier transform, equation 2.20 becomes

$$-m\omega^2\tilde{y}(\omega) + i\omega c\tilde{y}(\omega) + k\tilde{y}(\omega) = \tilde{u}(\omega)$$

which is linear and can be rewritten in order to isolate the system's transfer function:

$$\begin{aligned}\tilde{y}(\omega)[k - m\omega^2 + ic\omega] &= \tilde{u}(\omega) \\ \frac{\tilde{y}(\omega)}{\tilde{u}(\omega)} &= G(\omega) \\ G(\omega) &= \frac{1}{k - m\omega^2 + ic\omega}\end{aligned}\tag{2.21}$$

$$\tag{2.22}$$

Transfer function of the fuel assembly

As the assemblies are attached to the main structure at their extremes, their behaviour is similar to that of harmonic oscillators.

Transfer functions are used to perform an estimate of dynamical parameters of the fuel assembly such as the modal mass m_i , the modal stiffness k_i and the modal damping c_i , where the index i indicates the i -th mode. The system is supposed to behave linearly. Defining the reduced damping ξ_i and the natural frequency ω_i for the i -th assembly

$$\xi_i = \frac{c_i}{2\sqrt{m_i k_i}} \qquad \omega_i = \sqrt{\frac{k_i}{m_i}}$$

then the module of its transfer function 2.22 can be written:

$$|G_i(\omega)| = \frac{1}{m_i \sqrt{(\omega^2 - \omega_i^2)^2 + 4\xi_i^2 \omega_i^2 \omega^2}}\tag{2.23}$$

This transfer function has its maximum at the resonance frequency $\omega_{r,i} = \omega_i \sqrt{1 - 2\xi_i^2}$. The theoretical transfer function defined above is used to estimate the mass, stiffness and damping parameters of the fuel assembly making use of the LSM (Least Square Method). Such a regression method for the estimation of the parameters is simple to implement but does not ensure the convergence to a good set of parameters for any initial guess. A trial and error routine is thus used in order to choose the proper initial guess allowing the LSM method to converge to the right values.

2.3.2 Cross-correlation

The above-defined transfer function provides the frequency response of the linear dynamic system for an impulse at a fixed frequency. Using the method of cross-correlation, the frequency response is essentially calculated over all frequencies (i.e., experimentally speaking, a limited bandwidth of frequencies) in one run. The core of the method is that a random signal $u(t)$ is applied as excitation to the system, then the cross-correlation function between the signal and the resulting output $y(t)$ is calculated. The cross power spectrum is then obtained by taking the Fourier transform of the cross-correlation function. Finally, the frequency response is calculated by dividing the cross-spectrum by the input spectrum.

Chapter 2. Theoretical background

Taking a real⁴, stationary signal $u(t)$ of period T , its autocorrelation is defined as:

$$\mathcal{R}_{uu}(\tau) = \mathbb{E}[u(t)u(t + \tau)] = \int_{-\infty}^{\infty} u(t)u(t + \tau)dt$$

The Fourier transform of $\mathcal{R}_{uu}(\tau)$ is called the *Power Spectral Density* (PSD) $\mathcal{S}_{uu}(\omega)$. Thus:

$$\mathcal{S}_{uu}(\omega) = \lim_{T \rightarrow \infty} \frac{1}{T} \int_{\frac{T}{2}}^{-\frac{T}{2}} \mathcal{R}_{uu}(\tau) e^{-i\omega\tau} d\tau$$

The cross-correlation between two signals $u(t)$ and $y(t)$ is therefore

$$\mathcal{R}_{uy}(\tau) = \mathbb{E}[u(t)y(t + \tau)] = \int_{-\infty}^{\infty} u(t)y(t + \tau)dt$$

and the cross power spectral density (CPSD) is defined as:

$$\mathcal{S}_{uy}(\omega) = \lim_{T \rightarrow \infty} \frac{1}{T} \int_{-\frac{T}{2}}^{\frac{T}{2}} \mathcal{R}_{uy}(\tau) e^{-i\omega\tau} d\tau$$

Obtaining an accurate cross-correlation function would ideally take an infinite amount of time. However, inputs taking the form of periodic chain give good estimates of the correlation functions, by integrating over one complete period of the input signal.

This method gives the frequency response of a system cross-correlating the input with the output. It can be shown that the cross-correlation function of output/input is proportional to the transfer function of the system $G(\omega)$:

$$G(\omega) = \frac{\mathcal{S}_{uy}(\omega)}{\mathcal{S}_{uu}(\omega)}$$

This technique has two advantages: the experiment may be performed in real-time while the system is working in its normal mode and the measurements are free from extraneous noise, provided that this is not correlated with the input $u(t)$.

Having introduced the PSD and CPSD concepts, another useful function is the *Coherence*: the coherence function C_{uy} between two signals $u(t)$ and $y(t)$ can be used to examine the relation between the two. It estimates the causality between the input and output and is defined as follows:

$$C_{uy}(\omega) = \frac{|\mathcal{S}_{uy}(\omega)|^2}{\mathcal{S}_{uu}(\omega)\mathcal{S}_{yy}(\omega)}$$

Therefore, values of coherence will always satisfy $0 \leq C_{uy}(\omega) \leq 1$. For an ideal linear system with constant parameters, single input $u(t)$ and single output $y(t)$, the coherence will be equal to 1.

⁴The reality of the signal implies that the complex conjugate of the signal is the signal itself: $u^*(t) = u(t)$, for $u \in \mathbb{R}$

Discretization functions The Fourier transform deconstructs a time domain representation of a signal into the frequency domain representation, but it does not work on discrete signal. Since the signal analysis in chapter 5 concerns sampled signals, it is useful to take a look on the discretization of the previous functions.

Instead of the Fourier transform, the **discrete Fourier transform (DFT)** is used, which produces as its result the frequency domain components in discrete values. The **fast Fourier (FFT)** is an optimized implementation of a DFT that takes less computation to perform but essentially just deconstructs a signal.

The DFT for a finite length sequence $u(n)$, of length N , is defined as:

$$U(\omega) = \sum_{n=0}^{N-1} u(n)e^{-i\frac{\omega}{N}n}$$

The power spectrum of a deterministic, finite length, discrete-time signal, $u(n)$, is defined to be the squared magnitude of the signal's Fourier transform:

$$\mathcal{S}_{uu}(\omega) = \frac{1}{N} \left| \sum_{n=0}^{N-1} u(n)e^{-i\omega n} \right|^2$$

In an analogous fashion the cross-spectrum of two signals $u(n)$ and $y(n)$ is defined to be

$$\mathcal{S}_{uy}(\omega) = \frac{1}{N} \left(\sum_{n=0}^{N-1} u(n)e^{-i\omega n} \right) \left(\sum_{n=0}^{N-1} y(n)e^{-i\omega n} \right)$$

For further information on automatic control the reader is referred to (Lanning & Battin, n.d.).

2.4 Theory on optical velocimetry

In many physical experiments it is necessary to measure flow velocity avoiding to disturb natural pattern of the fluid. Optical velocimetry techniques are non-intrusive techniques for measuring the flow velocity without interacting with it. They have become more and more popular in fluid-dynamics measurement since lasers have become affordable with time and also because they do not require highly specialized technicians. Indeed, laser and opto-eletronic devices are the main characters in this field.

Among all the techniques that use laser to measure the velocity, during the internship period, two of them have been performed: **Laser Doppler Velocimetry (LDV)** and **Particle Image Velocimetry (PIV)**. In this section both will be explained after having briefly recapitulated the principles of a laser.

Laser principles Laser radiation is an electromagnetic wave that has the following properties:

1. the wave is **monochromatic**: it oscillates at a precisely optical frequency ν and has a precisely wave length $\lambda = \frac{c}{\nu}$;

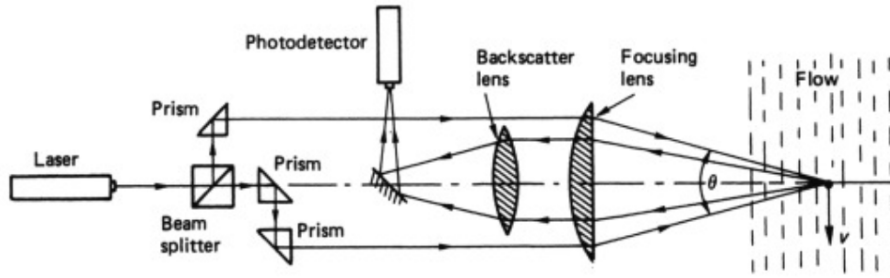


Figure 2.8: Backscattered LDV scheme

2. it is spatially and temporally **coherent**: for every point on the wave front, at any time, the phase differences $\Delta\varphi$ of the electric field is 0.
3. it is **directionable**: the wave electric field $\mathbf{E}(\mathbf{r}, t)$ does not diverge and remains confined in a preferred direction.
4. it is **brighter** than other light sources: the brightness $B(\theta, \phi)$ of a given source of e.m. waves is the power emitted dP per unit surface area dS per unit solid angle $d\Omega$: $B(\theta, \phi) = \frac{dP}{dS \cos(\theta) d\Omega}$. Due to its highly directional properties, laser beams of even moderate power have a brightness that is several orders of magnitude greater than that of the brightest conventional sources. This means that the peak intensity produced in the focal plane of a lens can be several order of magnitude larger for a laser beam compared to that of a conventional source.

Practically, all of these theoretical properties are subjected to small variations depending on the laser technology. These variations are studied with different approximation orders and, by operating with some optical parameter (such as the optical path or the laser power), they could be smoothed and controlled. The reader is addresses to (Svelto & Hanna, 1998) for a complete treatment of the laser principles.

2.4.1 Laser Doppler Velocimetry

Laser Doppler Velocimetry uses the Doppler effect to measure the velocities of the particles in a flow. Well known concerning sound waves⁵, the Doppler effect describes the wave frequency shift due to the velocity of the source itself. With the development of laser, Doppler effect on electromagnetic waves has become possible to measure.

To perform LDV measurements, it is necessary to have small particles moving inside the fluid. Indeed, the main assumption of LDV is that, measuring in a small control volume the velocity of the particles flowing through it, the velocity of the particles and the fluid is the same. Different methods are available when using LDV. In our case of interest, there are two laser beams and the photodetector catches the backscattered light, as it is shown in Fig.2.8⁶. The two incident laser beams create

⁵The classic example of Doppler effect in sound waves applied to everyday life is the change of sound when a siren approaches and then moves away from the observer.

⁶This figure is in (Carlton, 2018)

an interference volume: when the particle passes through this volume, it reflects the light. The backscattered light is collected in a photomultiplier and sent in the photodetector. By means of the photodetector it is possible to measure the frequency shift and therefore to obtain the velocities of the particles.

The two laser beams are different in their frequencies of $\Delta\nu$, hence the two frequencies are

$$\nu_{i,1} \qquad \text{and} \qquad \nu_{i,2} = \nu_{i,1} + \Delta\nu$$

Taking only one beam, supposing the first, and assuming its propagation direction is $\mathbf{l}_{i,1}$, when it intercepts the particle with velocity \mathbf{u} , it is reflected by the particle. The backscattered beam will be characterized by a frequency:

$$\nu_{s,1} = \nu_{i,1} + \frac{\mathbf{u}}{\lambda_{i,1}} \cdot (\mathbf{l}_{s,1} - \mathbf{l}_{i,1})$$

where $\mathbf{l}_{s,1}$ is the propagation direction of the scattered beam. The same holds for the second beam. Therefore the Doppler frequency is

$$\nu_D = \nu_{s,2} - \nu_{s,1} = \Delta\nu + \frac{\mathbf{u}}{\lambda_{i,1}} \cdot (\mathbf{l}_{i,1} - \mathbf{l}_{i,2}) \qquad (2.24)$$

The measures do not depend any longer on the propagation direction of the reflected beams since $\mathbf{l}_{s,1} = \mathbf{l}_{s,2}$ and the velocity of the particle, hence of the fluid, is easily obtained rearranging Eq. 2.24. Furthermore, the frequency shift $\Delta\nu$ is also justified: its presence allows to understand the sign of the particle velocity on the vertical direction:

$$\begin{array}{lll} \nu_D = \Delta\nu & \longrightarrow & \mathbf{u} = 0 \\ \nu_D > \Delta\nu & \longrightarrow & \mathbf{u} > 0 \\ \nu_D < \Delta\nu & \longrightarrow & \mathbf{u} < 0 \end{array}$$

To recapitulate, LDV is a non-intrusive and very accurate technique that permits to measure velocity of the flow with good spatial and temporal resolution. It allows to collect high data rates also in hostile environments. Furthermore it does not need to be calibrated. Unfortunately, it also has some limitations not only due to the expensive equipment. Indeed, the flow must be seeded with particles if none naturally exist, it could be difficult to collect data very near walls and it is a single point measurement technique. Nevertheless, in this work, none of these limitations were present.

For further information on LDV techniques the reader is addressed to (Kalkert & Kayser, 2006; Zhu, 1996; Albrecht *et al.*, 2013).

2.4.2 Particle Image Velocimetry

Particle Image Velocimetry (PIV) is a whole-flow-field technique providing instantaneous velocity vector measurements in a cross-section of a flow. The technique is applicable to a range of liquid and gaseous flows. The fluid is seeded with particles

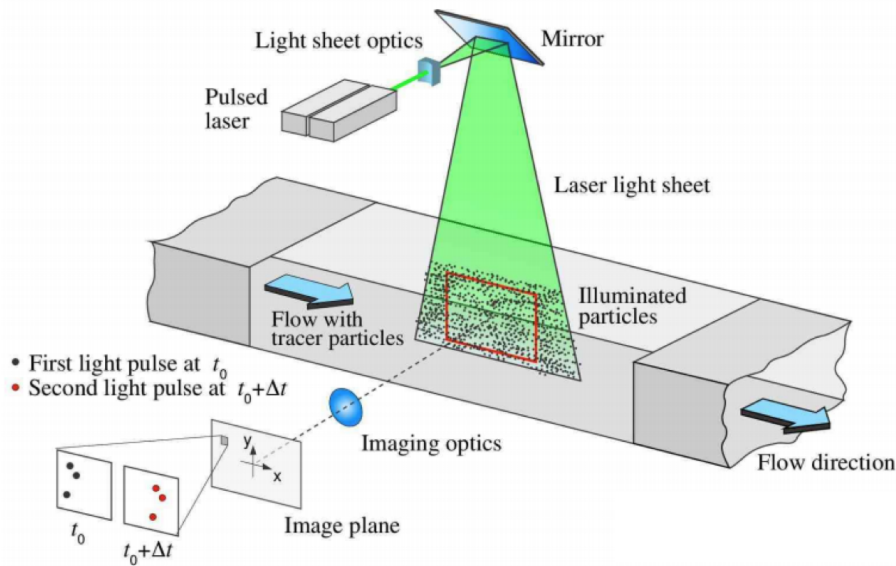


Figure 2.9: PIV scheme

which are generally assumed to faithfully follow the flow dynamics. It is the motion of these seeding particles from which the velocity information is calculated. It is done by taking two images shortly after one another and calculating the distance individual particles travelled within this time. The displacement field is determined from the motion of the seeding particles between the two images, then the velocity field is obtained by dividing the displacement field by the known time separation.

As illustrated in Fig. 2.9, a typical PIV setup consists of a CCD camera, high power laser, an optical arrangement to convert the laser output light to a light sheet, tracer particles and the synchronizer⁷.

A special camera is used so that it can store the first image (frame) fast enough to be ready for the second exposure. To avoid having blurred images while analysing fast flows, laser pulses must be used. They freeze any motion and also acts as a photographic flash for the digital camera. The light sheet is obtained from the laser beam by simply using spherical and cylindrical lenses in combination. The tracer particles form the basis of the velocity measurement in PIV. The particles should be as small as possible so that they are able to closely follow the flow. However on the other hand, they may not be too small, because then they will not scatter enough light, and hence produce too weak images. Any particle that follows the flow satisfactorily and scatters enough light to be captured by the camera can be used. The synchronization between the laser and the camera is then controlled by the synchroniser.

PIV actually does not track each particle individually, that is a similar but separate technique known as Particle Tracking Velocimetry (PTV). Rather than each particle, PIV divides the 2D region in *interrogation windows*, small enough as not to show any significant velocity gradient within the interrogation area. The particles in the laser sheet reflect the light that is caught by the camera. For each temporal steps the correlation between the intensities of the interrogation windows, in the two

⁷This figure is on (Raffel *et al.* , 2018).

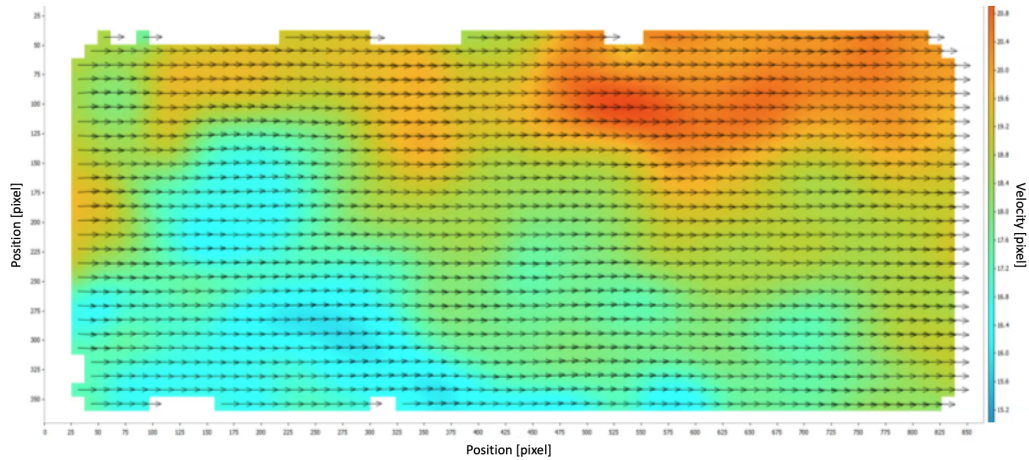


Figure 2.10: PIV result in a section plane of a vertical flow. Image is rotated of 90° . The different colors underline different values of the velocity, from the smallest in blue to the larger in red, while the vectors indicates the direction and the verse of the velocity field

frames at t_i and $t_i + \Delta t$, gives an average displacement vector. The union of the displacement vectors creates the final image obtained from the PIV measurement, as shown in Fig. 2.10.

PIV technique allows the identification of the velocity field in an almost 2D-flow. It is a powerful non intrusive techniques but it suffers from some limitations. For example the time delay between the laser pulses should be long enough to capture the displacement of the tracer particles and short enough so that the particles with an out-of-plane velocity component leave the light sheet. Furthermore, the accuracy of the PIV measurements will drastically improve as the particles follow the flow more closely: therefore, small particles are preferred but they can be used only if associated to high power lasers. Fortunately in LTHC these limitations were not present. These and further information on PIV and velocimetry techniques are available in (Raffel *et al.* , 2018; Nagargoje, 2017; ValueBound, 2008).

Chapter 3

Experimental setup

This chapter concerns the experimental setup. After a brief chronological excursus on the previous setups, *Icare experimental* will be presented and will conclude the first part of the thesis work. Secondly, the new configurations of Icare will be illustrated signing the starting point of the internship with its first goal: installing the *Small* confinement configuration 3.3.

3.1 History of the experimental setups

Fluid-structure interaction has been studied for long time at CEA. In particular, concerning fluid-structure interaction between fluid and assemblies in a PWR core, the first experimental facilities date back to the beginning of the 90s.

Since it would be complicated and very expensive to reproduce a real scale nuclear core, different facilities have been constructed during the years scaling some of the parameters (number of assemblies, pressure, temperature, etc.). Throughout these years their likelihood to a PWR core became so accurate that actually in LTHC there is *Hermes*, a facility with real scale dimensions. A brief summary on the older experimental setups *Eros*, *Echasse*, *Cadix*, *Couplage* is here discussed. Following, *Hermes T* is presented.

Eros In 1990, Eros was the first of a long series of facilities aimed at understanding the phenomena involved in the vibration of the assemblies. This setup consisted in 5 reduced-scale fuel assemblies, with 6 x 6 fuel rods each, placed on a shaking table. The experiments performed on Eros showed the possibility to model the assemblies as beams with non-linear relations.

Echasse The Echasse setup followed in 1999 at the LHC with the purpose of measuring the impact forces between two assemblies or between an assembly and the wall. It consisted of two reduced-scale assemblies, with 8 x 8 fuel rods each, and housed experiments in standing water and in axial flow up to 4.8 *m/s*. Therefore, the tests were performed in several flow configurations: air, standing water, 2.4 *m/s* and 4.8 *m/s*. During the experiments, the impacts were caused by a "quick-release" phenomenon: one of the assemblies was removed from its equilibrium position and then quickly released to the wall or the second assembly direction.

Cadix In 2000 new experiments were carried out in the Cadix facility at the EMSI lab (CEA-Saclay). This setup involved for the first time full scale 6 fuel assemblies in row on a shaking table. The tests aimed at measuring the impact forces on full scale assemblies while the table was shaking. They were performed either in air or standing water. The test evaluated also confinement effects and was also used to validate a computation code developed in parallel.

Couplage In 2006 the first experiments aiming at studying the coupling between assemblies were carried out on Couplage setup. It was built 2 years before in LHC and it was the first facility arranged in a 2D plane. It has 9 reduced-scale fuel assemblies arranged in square 3 x 3 lattice, each of which with 4 x 4 fuel rods held together by only one spacer grid placed in the middle. The central assembly was put in motion by means of a hydraulic jack that imposed a displacement following a sinusoidal signal whose frequency varied from 0 to 4 Hz. Even though the geometry of this experimental facility was not representative of a nuclear reactor core, and even if the assemblies scale was too small to be able to well represent a real nuclear fuel assembly, the experiments on Couplage allowed to study coupling forces between the fuel assemblies and to outline the presence of non negligible interaction forces between assemblies placed on different rows.

These and further information on the previous facilities are in (Boccaccio, 2015), (Clément, 2014), (Capanna, 2018) and above all in (Ricciardi, 2008), in which Ricciardi used the experimental data collected on Echasse and Cadix and performed by himself experiments on Couplage in order to corroborate his porous medium model (see section 2.1.2).

3.1.1 Hermes

As anticipated in the introduction to the chapter, regarding fluid-structure interaction, nowadays the main facility in LTHC is Hermes. Hermes is a setup that allows 2 different configuration: P and T. In P configuration, the facility houses 1 full scale 1300 MW PWR fuel assemblies and can simulate real operation conditions in a PWR core (155 bar and 330 °C). Such configuration was designed in order to analyse the pressure drops along real fuel assemblies and to be able to validate new designs for fuel assemblies and to ensure the compatibility between fuel assemblies with different designs. On the other side, in Hermes T configuration lower temperature and pressure conditions are admitted. It can handle up to 2 fuel assemblies, one of which is excited by a hydraulic jack. In Hermes T a pump can supply 1200 m^3/h in axial flow and 400 m^3/h in cross-flow, at 35 bar and 170 °C. Therefore, the flow rate is similar to the PWR conditions, the lower temperature allows to provide accurate measurement devices to the test-section. As it is shown in Fig.3.1, the fuel assembly used in Hermes is made up of 25 guide tubes and 264 fuel rods, each having a height of 4.5 m hold together by 10 spacer grids. The force applied by the hydraulic jack is measured by a load cell while the displacements of its grids are measured with *Linear Variable Differential Transformer* (LVDT) sensors. Its boundaries house acrylic windows allowing optical fluid measurements with a LDV device.

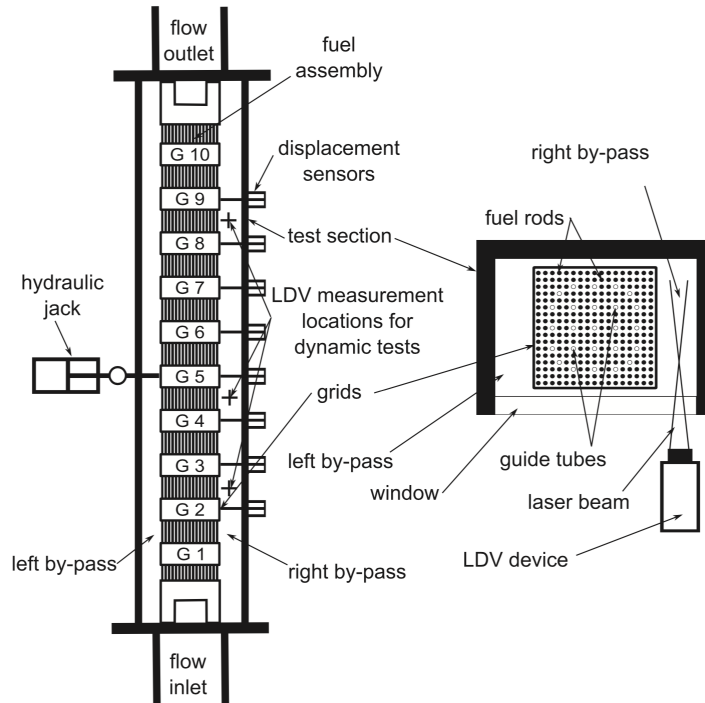


Figure 3.1: Hermes T: the facility handles a full scale fuel assembly which can be excited by a hydraulic jack. LDV experiments can be performed due to the presence of portholes in the wall of the structure.

Hermes has been used in order to perform several experimental analyses concerning coupling between fuel assemblies and fluid velocity in the boundary layer of the excited fuel assemblies. It has been and still is the main character of many papers, among all (Ricciardi & Boccaccio, 2014), (Ricciardi & Boccaccio, 2015), (Ricciardi, 2016) from which image in Fig.3.1 and Hermes T description have been taken.

3.2 Icare expérimental

Even though the Hermes T facility permits the study of the interaction between 2 assemblies, it has been used until now only with one excited assembly. Furthermore, it has been shown how chronologically the setups have been addressed even more to study the coupling between assemblies, also misaligned on multiple rows. Couplage reached this purpose even though not on a representative scale. Since in terms of time, money and space, it is expensive to recreate the same geometry of Couplage with full-scale assemblies, a new reduced-scale facility was designed and installed in LHC: *Icare expérimental* (Icare).

Icare facility has been firstly designed and made operative in 2014 during the PhD project of S. Clément (Clément, 2014), mainly aiming at studying the coupling between misaligned assemblies with a design close to the reality. Unlike Couplage, Icare has 4 assemblies in a square lattice 2 x 2 with the possibility to change their number from 1 single assembly to 4 assemblies. This setup permits to force the vibration of one assembly at different amplitudes, frequencies and heights. Icare

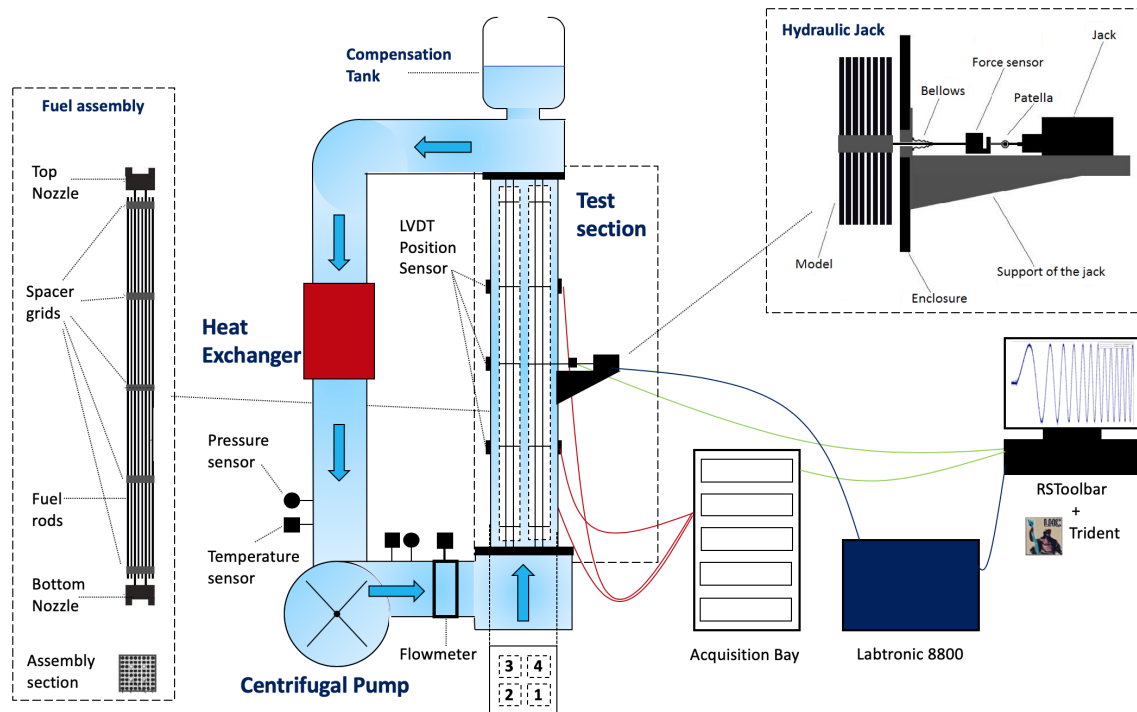


Figure 3.2: Icare scheme: the centrifugal pump turns the water into Icare cycle while the heat exchanger holds the temperature in stationary state. Inside the test section there are 4 fuel assemblies of which one is excited by the hydraulic jack. The jack is commanded by RSToolbar and the displacements of all the assemblies are recorded by Trident.

allows to study confinement effects changing the distances between assemblies and between assemblies and walls too. Finally, it is possible to change the flow rate and its temperature in order to investigate also the sensitivity to these parameters. Since Clement's design, Icare has been slightly modified by Capanna maximizing its performances (Capanna, 2018). Some of these modifications have occurred during the internship period and will be presented in the next section, meanwhile the technical description of Icare is provided. This and further information are in (Clément, 2014; Boccaccio, 2015; Mokhtari, 2016; Capanna, 2018).

As shown in Fig.3.2, Icare is a closed thermo-hydraulic loop mainly formed by the test section, one heat exchanger and one centrifugal pump. A compensation tank with a free open surface was added on the top of the test section in order to release the bubbles present inside the water loop.

Avoiding to spend too many words on the pump and the heat exchanger, it is sufficient to know that they allow a flow rate up to 6 m/s and a fluid temperature up to $30 \text{ }^\circ\text{C}^1$. In the test section there are four assemblies 1:2 scales in length. Simulating a PWR core fuel assembly (see subsection 2.1.1), each assembly contains 64 rods in a square lattice 8×8 , held together by 5 stainless steel spacer grids. Among the 64 rods, 60 simulate the fuel rods, while 4 of them simulate the guide

¹The maximum flow rate changes with the different layout chosen for the test section; with 2 assemblies in Small configuration the maximum flow rate is 6 m/s .

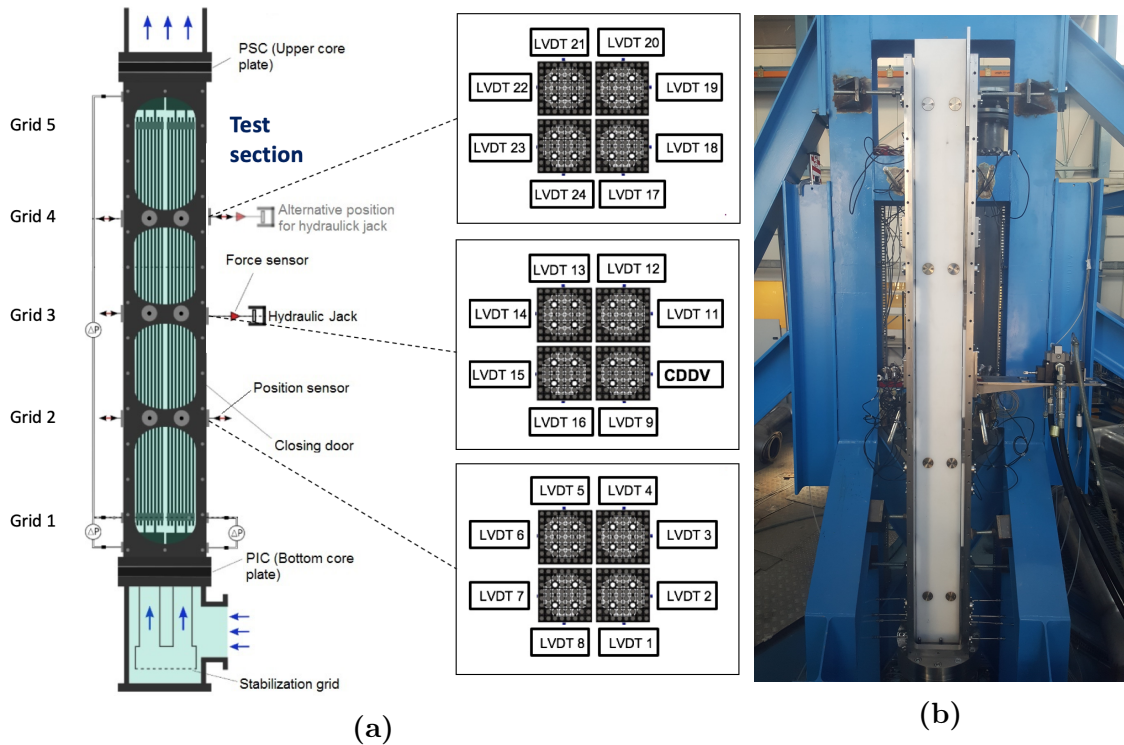


Figure 3.3: a) Icare LVDT displacement sensor scheme: the 3 sections correspond to the grid 2, 3 and 4. b) Photo of the empty Icare test section in Small configuration predisposed for two assemblies without frontal door; this photo corresponds to the scheme in Fig. 3.4e.

tubes. These 4 are in stainless steel and provide the stability of the structure, since they are micrometrically welded to the spacer grids. Instead, the other 60 rods are trapped into the grids, like in a real-scale full assembly. The assembly is trapped in its position by means of 2 nozzles, one that engages to the Upper Support Plate (PSC: *Plaque Supérieure de Cœur*) and one that engages to the Lower Support Plate (PIC: *Plaque Inférieure de Cœur*).

Each rod is 2.57 m long with a diameter of 9 mm . The 12.5 mm of pitch plus the thickness of the spacer grids, give to the assemblies a square section at the grids level of $10,1 \times 10,1\text{ cm}^2$. Then four assemblies are collocated in a vertical square test section with an area of $22,5 \times 22,5\text{ cm}^2$. Along the test section there are 9 pressure sensors and, corresponding to the 3 central spacer grids heights, there are 24 position sensor LVDT positioned as shown in Fig.3.3a. Further information on LVDT will be discussed in subsection 3.2.1.

Icare is a modular facility and it is possible to change many parameters. The test section consists of 3 longitudinal walls and a frontal door that allows to configure more layouts of the experimental setup. For example it is possible to change the material of the assemblies choosing between 2 set of 4 assemblies. The first set is in stainless steel and allows to perform experiments concerning the rigidity of the structure thanks to its similarity (apart for a scaling factor) to the real assemblies. The other set is in *Poly(methyl methacrylate)* (PMMA), and it allows to study better the forces between the structure and the fluid because of its reduced rigidity. **With respect to this work, which aims at studying fluid-structure interaction,**

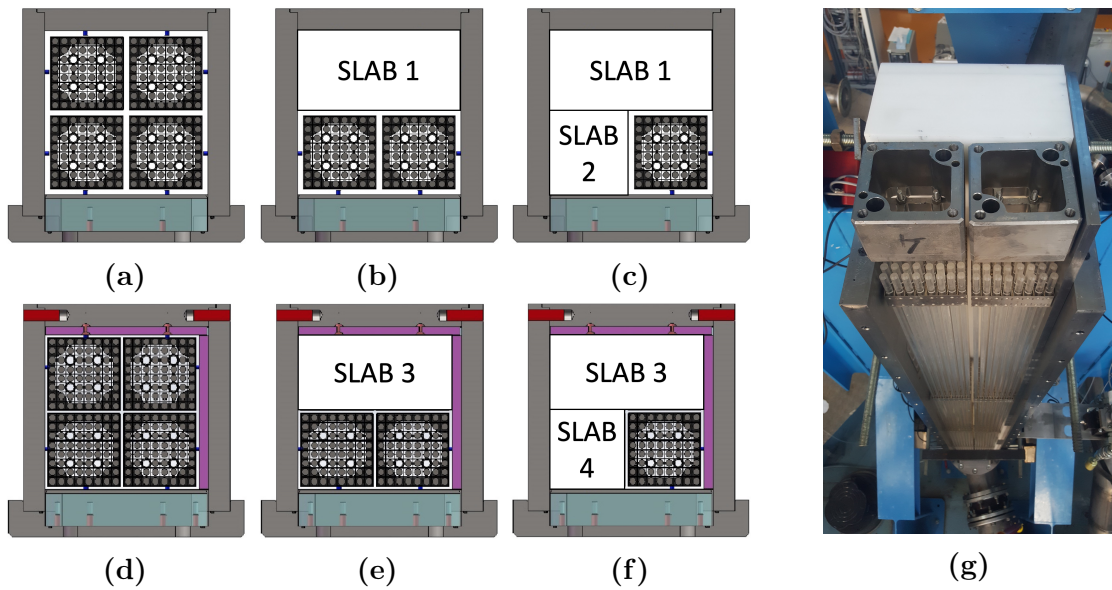


Figure 3.4: Icare confinements. Confinement size in large configuration is 8 mm between the walls and the assemblies and between the assemblies: a) 4 assemblies, b) 2 assemblies, c) 1 assembly. In small configuration two 12 mm thick plates, one behind and one on a side of the assemblies, reduce the confinement size to 4 mm between assemblies and between the assemblies and the walls: d) 4 assemblies, e) 2 assemblies, f) 1 assembly. g) Photo of Icare test section without frontal door corresponding to the e) layout: small configuration with 2 assemblies.

only experiments with PMMA are considered.

It is also possible to change the confinement size. As shown in Fig. 3.4, one can choose among 2 by-pass sizes between the assemblies and between the assemblies and the wall. In *Large* configuration all the by-passes are 8 mm , while in *Small* configuration the gap is reduced to 4 mm ; note that it is not possible to choose different size between the assemblies with respect to the assemblies and the walls: or all the by-pass are *Large* or all of them are *Small*². This allows the study of the sensitivity with respect to the confinement, too. Furthermore, again as it is shown in Fig. 3.4, one can choose the number of the assemblies for the experiment: 4 slabs (2 for each confinement) permit to select 3 configuration. Experiments can be carried out with 4, 2 or even a single assembly. In this work experiment with 1 assembly alone are not considered.

A hydraulic jack can be installed in the place of one of any LVDT sensor. By means of this jack it is possible to excite one of the four assemblies to the 3rd or to the 4th grid; in particular concerning this work, the experiments were carried out with the jack on the right wall facing the door of Icare. With respect to the Fig. 3.2, the jack excites the assembly number 1. The other assemblies are then enumerated clockwise. In Fig.3.3a the position of the jack is indicated as *CDDV*. The possibility to excite the assembly on different grids allows to excite different natural modes.

Finally, along the test section of Icare there are 4 portholes on 3 walls, for a total

²From now on, *Small* or *Large* with capitol letter will be used meaning *Small confinement* and *Large confinement*.

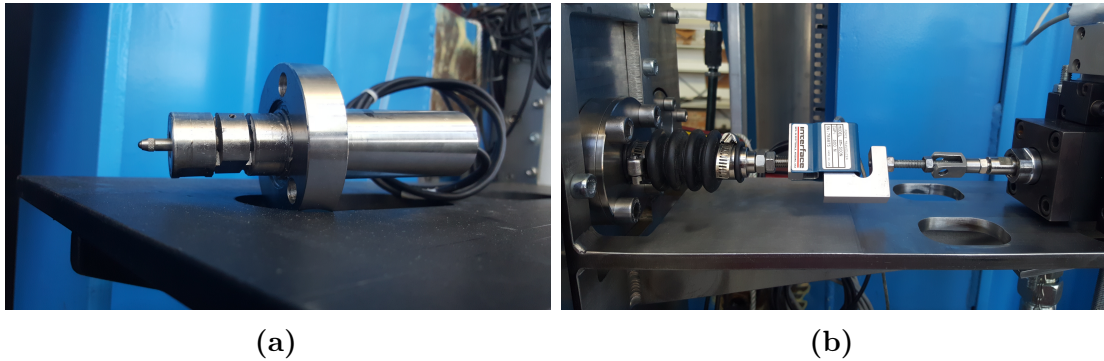


Figure 3.5: a) Displacement sensor LVDT housed in a cylindrical body ready to be mounted on the setup. b) Force sensor with first type bellow already connected to the piston and to the hydraulic jack.

of 12 portholes. These are on the frontal door of Icare and on the lateral walls and they permits to use optical velocimetry techniques in order to measure the flow inside Icare.

Out of the context of this work, two other parameters can be changed performing experiments in Icare. An asymmetry can be imposed to the flow rate inside the assembly by means of small plates with different hole section placed at the inlet channel. Furthermore, a pre-stress on the fuel assemblies can be imposed by using a toolbox which allows to flex or twist one or more fuel assemblies. The flow redistribution due to the asymmetry and the force applied on the pre-stressed assemblies can be measured with high accuracy.

3.2.1 Data acquisition

The experiments with Icare are performed exciting one assembly through the hydraulic jack. The input signal is given by *RSToolbar*; this is a software that permits to choose the shape of the signal, the amplitude of excitation, the range of frequencies and the temporal increment in the frequency sweep. Then the hydraulic group *Labtronic 8800* imposes the input signal on the assembly by means of the jack. The jack passes through the Icare wall using a bellow and it is screwed in the assembly (see Hydraulic jack scheme in Fig. 3.2). A Force sensor is installed in between the hydraulic jack and the bellow. The force sensor (SM-S by Interface shown in Fig. 3.5b) has a capacity of $\pm 500\text{ N}$ and an accuracy of 0,045 % of the full scale, meaning an uncertainty of $\pm 0,225\text{ N}$. The jack is also equipped with a position sensor with a capacity $\pm 10\text{ mm}$ and $0,03\text{ mm}$ uncertainty. Since its higher sensitiveness with respect to the force sensor, this position sensor gives the feedback to *RSToolbar* in order to allow the control of the jack motion.

As it is shown in Fig. 3.3a, the 24 displacement sensors are 8 for each level on the 3 central grids of Icare, grouped in 4 couples, one for each wall at each level. Assuming the first and the fifth grid as motionless, only the other 3 central grids are free to move in 2 directions. This configuration of the LVDT allows to measure the displacement of these grids in both directions. The LVDT sensors (model D5/300AW by RDP in Fig. 3.5a) have a capacity of $\pm 7,5\text{ mm}$ and an uncertainty of $\pm 0,0025\text{ mm}$

(giving a relative uncertainty of 0,3 %). They are housed in a cylindrical body to be mounted on the experimental apparatus.

The acquisition bay takes the signal from the LVDT and sends them to *Trident*. Trident is the LHC labVIEW-based software that records the sampled signal from LVDT and from the Force sensor. Furthermore it also records the signal from the pressure and temperature sensors and from the flowmeter. The signals from LVDT and force sensors are sampled at 2 *kHz*, while the others are sampled at 1 *Hz*.

Successively, the data sets recorded by Trident are treated with Scilab in order to perform the experimental data analysis.

Recap on experimental facilities

Table 3.1 shows the main properties of the facilities presented in this chapter sketching their configuration, goals and limits.

3.3 New configurations

All that has been presented so far (in the introduction of the subject, the theoretical notions and the description of Icare) had the purpose of making the reader able to understand the topic and the context in which the internship took place. After the bibliographic research, the core of the thesis work starts here, both chronologically and concretely, installing the Small confinement layout on the experimental setup.

3.3.1 Small confinement configurations

Several experimental campaigns in Large confinement layout have been carried out, both with 4 or 2 assemblies. One of the purposes of the internship is to perform new campaigns with Small confinement; indeed, this has been the first time in which such a configuration has been installed.

In the Large confinement configuration, the by-pass between the assemblies and between the assemblies and the walls is 8 *mm*. In order to reduce the by-pass size to 4 *mm*, two plates 12 *mm* thick have been installed on the back and on the right wall. A first attempt to install the back plate has failed. Indeed, the plate was in stainless steel and as long and wide as the test section, without proper tolerance parameters. It has been replaced with a better one in PMMA and then installed without problems (photo in Fig. 3.4g). Since on the right wall there are four portholes, the right wall plate is not a uniform vertical sheet. In order to gain the 12 *mm* on the right, the portholes are replaced with thicker ones, while five small plates are installed in the gaps between the portholes. These plates are in stainless steel with a thickness of 12 *mm* and a width of 213 *mm* equal to the section of Icare minus the 12 *mm* subtracted by the back plates. Also the PIC and the PSC have been replaced in order to center the 4 assemblies in the new configuration.

During the experiments, the assemblies are in Icare test section that is filled with water. The experiment consists in exciting one of these assemblies with a piston linked to an hydraulic jack. Between the piston and the jack there is the force sensor. The assemblies are in volume filled of water while the hydraulic jack and the force

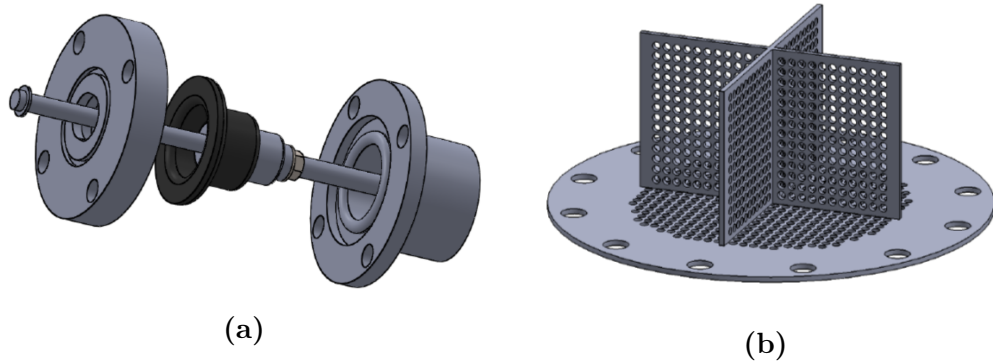


Figure 3.6: a) The new bellow hosted in the cylindrical body with the piston screwed in. b) Vortex breaker grid.

sensors are outside this volume (they are not waterproof). Therefore, the piston links two objects, one inside and one outside the water filled volume. In order to provide this link, avoiding any water leakage at any flow velocity, and allowing the displacement motion of the piston also at high frequencies, a bellow is necessary.

At high flow velocities the old bellow swelled with water. Therefore, a new sealing system has been designed by Capanna. The new design consists in a smaller bellow hosted in a cylindrical structure in which a new piston is screwed (see Fig. 3.6a).

Installing the Small confinement layout, the bellow and the piston have been changed. Once the sealing system has been installed, the new hydraulic jack and the force sensor have been calibrated. Also the LVDT sensors on the back and on the right walls have been recalibrated. Indeed, with the new layout, the body that houses the LVDT sensor is replaced with a shorter one. In this way the LVDT sensor can penetrate more in the test section, crossing the 12 mm added with the plates. Furthermore, while the old piston was installed on the 4th grid of the assembly, installing the Small confinement layout, the hydraulic jack has been mounted on the 3rd grid. Therefore, the experimental campaigns in Small confinement layout have been carried out exciting the assembly at half-height.

At high flow velocity over 3 m/s the presence of air bubbles represents a relevant problem. This problem becomes even more important when the Small configuration is used with two assemblies. Since the mass flow rate imposed by the pump is constant but the section of Icare is reduced, in this configuration the flow velocity can be brought to higher values. The only entrance for the gas in Icare water loop is by the compensation tank. Indeed, at high flow velocity, inside the tank the water creates a vortex that can imbibe small volumes of gas. This gas enters in the Icare loop creating the bubbles. The presence of bubbles in the fluid is a problem because the fluid becomes a double phase fluid and above all because the bubbles interact with the laser beam, making the optical velocimetry techniques unusable. To avoid this problem a vortex breaker grid has been designed by Capanna and has subsequently been installed at the base of the tank (see Fig. 3.6b) (Capanna, 2018).

Starting a new set of experimental campaigns for the first time in Small configuration, a new *Procédure de conduite Icare* (Icare drive procedure) has been written and released. The *Procédure de conduite Icare* is a document that illustrates how to

conduct an experiment with the Icare facility. From the parameters to set on the softwares (RSToolbar and Trident) at the beginning to the temperature range for the oil of the hydraulic jack, from the procedure to save the data to that to calibrate new sensors. Following this Procédure it is possible to run experiments on Icare even without having any familiarity with the facility.

3.3.2 Optical velocimetry configuration

Experiments with LDV and PIV techniques have been performed in Small confinement layout. As already explained in section 2.4, these techniques use a laser beam respectively detected by a photodetector and a camera. In this way it is possible to measure the local flow velocity inside Icare without interacting with the fluid, using some particles diluted in the water. LDV experiments measure the punctual particle velocity while PIV experiments record an area in which the particle trajectory and therefore the flow patterns could be reconstructed.

LDV configuration

During the LDV measurement the laser beam is reflected by the particles and the light is collected from the photodetector that records the velocity each time it receives a light impulse.

In order to perform LDV measurements on Icare, a few grams of Nylon particles with 40 nm diameter have been injected in the fluid. The laser is a solid state green continuous laser with a wavelength of 561 nm and power of 0,3 mW . LDV technique measures the velocity of one particle when it meets the measurement volume which is about 1 mm^3 .

LDV experiments have been carried out in 10 points of measure on 2 heights, 5 points for each level. The 2 heights are:

1. at 1738 mm from the bottom, between the 3rd and the 4th grid;
2. at 1138 mm from the bottom, between the 2nd and the 3rd grid.

For each level, the 5 points are located in the middle of the door of Icare, between the fuel assemblies [see Fig 3.7]; starting from the door:

- A at 2.5 mm , in the by-pass before the assemblies;
- B at 34.5 mm , at a quarter of the assemblies;
- C at 53.2 mm , at half of the assembly length;
- D at 103.1 mm , at the end of the fuel assemblies;
- E at 105.1 mm , at the beginning of the central bypass;

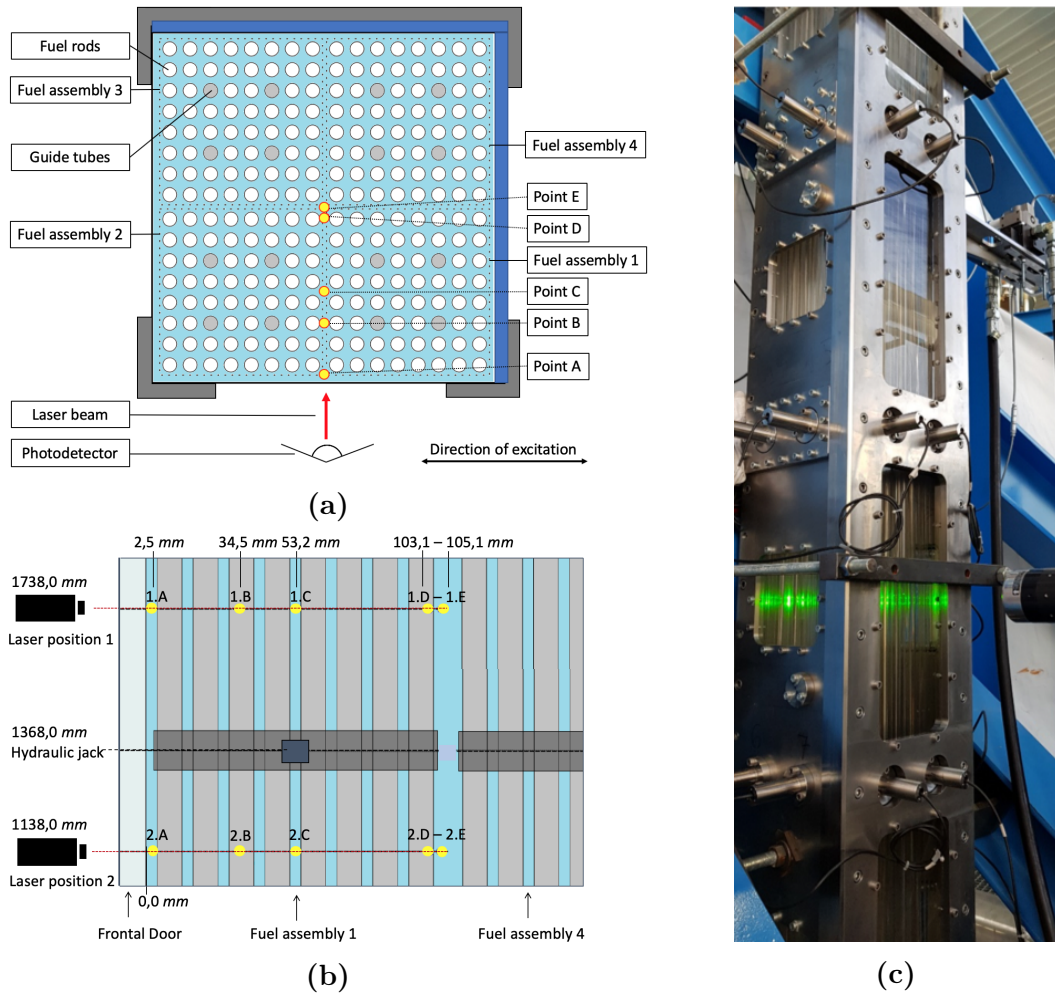


Figure 3.7: LDV points of measurements view: a) view on the horizontal section from the top; b) view on the central vertical section from the hydraulic jack side; c) photo of the LDV configuration with laser in position 2 [Test in Large confinement].

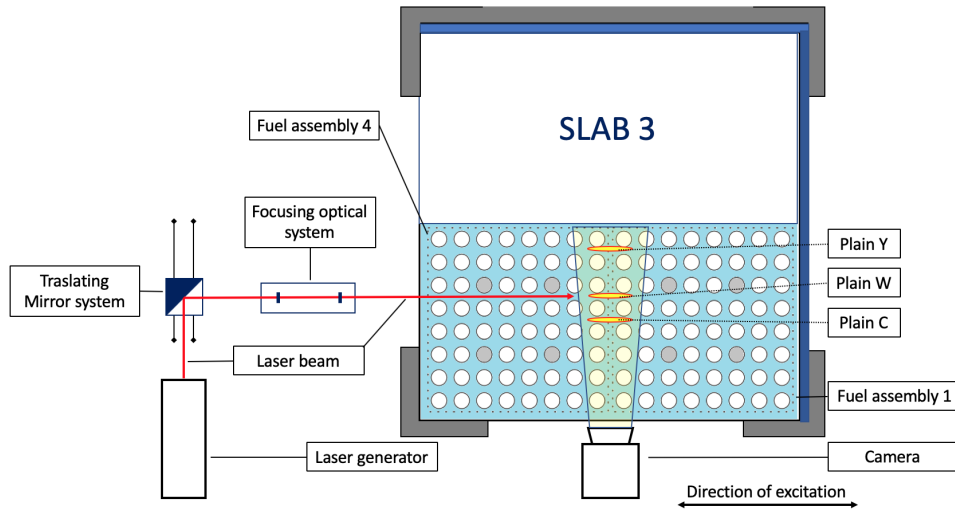


Figure 3.8: PIV scheme: view on the horizontal section from the top.

PIV configuration

Experiments with Particle Imaging Velocimetry technique record the flow by means of a high precision camera. These have been performed with only two assemblies, thus slab 3 was previously installed substituting assemblies 2 and 3 (see Fig. 3.4e); the LVDT facing the missing assemblies were replaced with special caps. For a better performance of the measuring techniques, another type of particles was diluted in the Icare loop: silver spheres with a diameter of $10 \mu\text{m}$. PIV technique needs the laser beam to enlighten the planes of measure. Therefore, the laser beam is flattened by the spherical and the cylindrical lenses.

Icare test section was not design to perform PIV measure, hence multiple attempts have been done before finding the right layout for the PIV setup.

A first attempt contemplated using an optical arm in order to bring the laser beam from the optical table, placed close to the test section, up to the left side window of Icare (see Fig. 3.9a). Then the final end of the optical arm was able to move by means of a millimetric 3D displacer. Due to mechanical instability and beam focusing problems, this method has been set aside.

In order to solve these problems, a little optical sheet has been adapted and installed on the left wall on Icare (see Fig. 3.9b). On this platform both the spherical and cylindrical lenses have been installed. In this way the laser beam leaves the optical table close to Icare, passes through a mirror system and reaches the lenses plane before entering the porthole. The mirror system is composed of two 45° mirrors one above the other. The mirror below is attached on a millimetric 1D displacer on the same table of the laser, while the upper one is movable along a vertical bar fixed to the table too. Therefore, the upper mirror can deflect the laser beam on different plane both in height and in depth inside Icare test section. With this design, PIV experiments have been carried out in 4 plans of measure on 2 heights, 3 plans for the level 2, between the 2nd and the 3rd grid, and 1 plan for the level 3, between the 1st and the 2nd grid:

Y between the 1st and the 2nd rod, only for the level 2

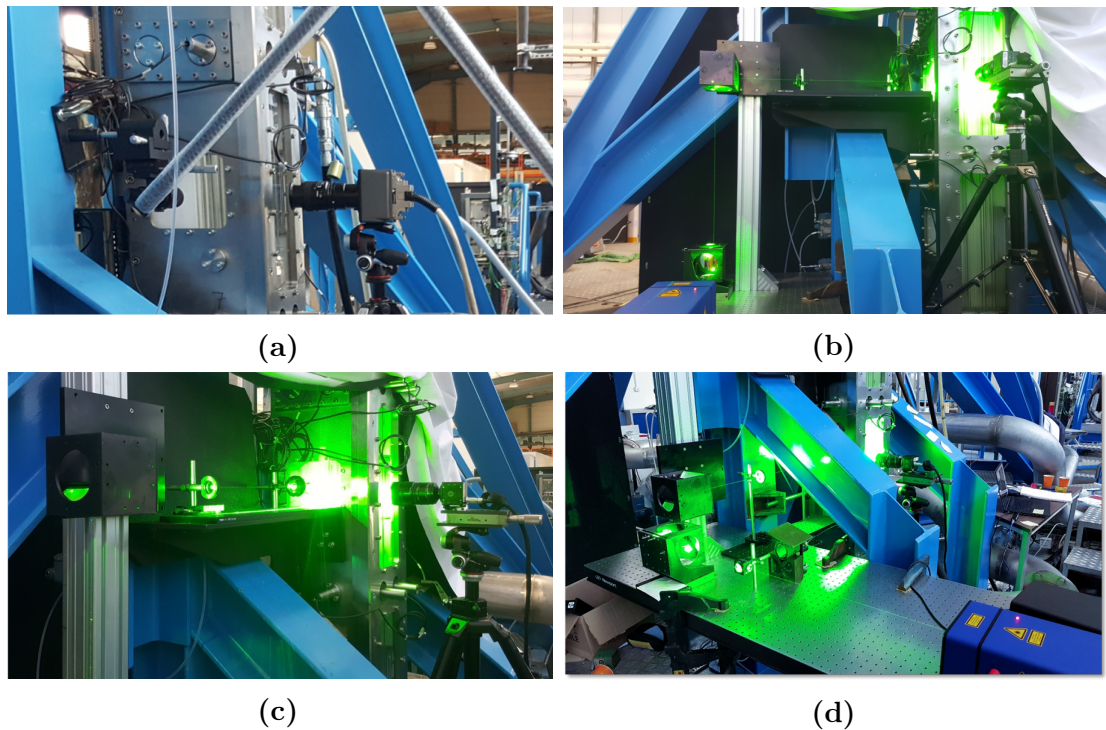


Figure 3.9: Photo of Icare test section for PIV measurement. a) first failed PIV layout; b) successful PIV layout; c) PIV configuration for level 2 measurements; d) PIV configuration for level 3 measurements.

W between the 3rd and the 4th rod, for levels 2 and 3

C at half of the assembly length, between the 4th and the 5th rod, only for the level 2.

As shown in Fig. 3.8, the camera recorded the portion of the plane in the gap between the 2 assemblies.

The internship has been focused on experiments in Small confinement layout. Unfortunately, PIV experiments have not been analysed. Data analysis of the other experiments will be shown in the next chapter.

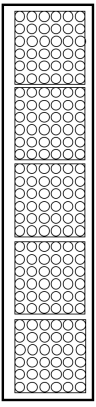
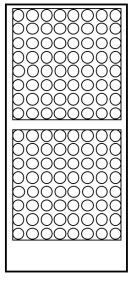
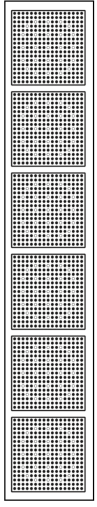
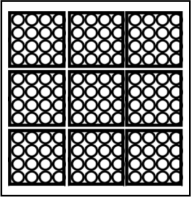
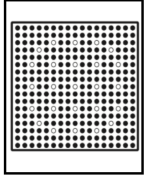
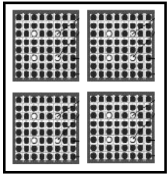
Facility	Section view	Objective	Limitations
Eros		Evaluating impact forces on a line of fuel assemblies	Reduced scale assemblies No water flow
Echasse		Evaluating impact forces under axial flow	Only 2 assemblies Large by-pass
Cadix		Evaluating impact forces on a real fuel assembly	No water flow Assemblies on a single line
Couplage		Evaluating coupling between fuel assemblies	Highly reduced scale assemblies: not representative Assemblies are not free to move
Hermes		Identification of modal parameters of a real fuel assembly (DEDALE campaigns)	Only one fuel assembly
Icare		Study the coupling between misaligned fuel assemblies that have a design close to reality.	Half scale assemblies

Table 3.1: Properties of the experimental facilities. Note that the **section views** are not in scale but contain the exact number of rods for assembly; the assemblies are in the right configuration.

Chapter 4

Experimental parameters and computational tools

In this chapter the experimental results obtained during the internship will be presented. Focusing on the objective of the experimental campaigns, the variables used during the experiments will be shown. Hence the procedure used to analyse the data set will be illustrated.

4.1 Objectives of the experimental campaign

Once the Small confinement layout was installed, it has been possible to perform the new experiments. As already pointed out in section 1.3.1, the internship involves the development of the code to analyse the experimental data.

During the whole life of Icare, experiment both in quasi-static and dynamic regime have been carried out. The experiments in almost-static regime aimed to identify the hysteresis of the stainless steel fuel assemblies. Evaluation on added mass and stiffness on both stainless steel and PMMA rods have been performed too. References on (Clément, 2014; Boccaccio, 2015; Mokhtari, 2016).

In particular, among all the possible analysis, this work is focused on the coupling between the assemblies, their natural frequencies, their vibrational modes and their sensitivity to the changes of the experimental parameters. For the very first time LDV and PIV measures have been performed on Icare, therefore LDV experimental analysis will be proposed too. Unfortunately, PIV measures will not be analysed in this framework.

4.1.1 Experimental parameters

Leads new campaigns in Small confinement layout, the experimental parameters have been chosen in order to collect a data set comparable with the Large confinement one. An important difference between Small and Large is due to the hydraulic jack position. Indeed, experiments in Small layout have been performed exciting the 3rd grid, while those in Large configuration were run forcing the 4th grid. Since the 3rd grid is at half-height of the assembly, in Small layout the even modes are not excited. This is due to the presence of a half-length node in the even modes (see

Parameter	Values							
Confinement	Small							
Excited grid	3 rd							
Frequency swept (Hz)	0,05 - 25,00							
Number of assemblies	2				4			
Temperature ($^{\circ}C$)	15		20		30			
Flow velocity (m/s)	No water	0	1	2	3	4	5	
Excitement amplitude (mm)	0,0	0,3	0,5	0,8	1,0	1,2	1,5	1,7

Table 4.1: Possible parameters for each experiment in Icare Small layout.

Velocity [m/s]	1A	1B	1C	1D	1E	2A	2B	2C	2D	2E
1	●	●	●	●	●	●	●	●	●	●
2	●	●	●	●	●	●	●	●	●	●
3	●	●	●	○	○	●	●	●	○	○
4	●	●	●	○	○	●	●	●	○	○

Table 4.2: Relations between experimental velocities, amplitudes and LDV points of measurements. **Legend:** ● → all the excitation amplitudes; ○ → any amplitude.

table 2.1). On the other hand in Large layout modes multiples of the 4th could not be investigate. This is less relevant since the proper frequency of the 4th mode is out of the frequency range excited during the experiments. Installing the hydraulic jack on the 3rd grid has been a contingent choice of the team. The same experiments could have been done exciting the 4th grid in Small layout too.

In order to investigate the transfer function of the fuel assembly, a sine wave is given as input. This sine wave is not fixed on a single frequency, but it swipes a range of frequencies from 0,05 Hz up to 25 Hz . The swept step is 0,05 Hz/s that is slow enough to excite harmonically the frequencies. The required time to swept the range is $T_s = 500 s$.

Table 4.1 recapitulates the possible values for the parameters in Small confinement layout. Experiments have been carried out both with 2 and 4 assemblies, at 15, 20 and 30 $^{\circ}C$. Different flow velocities have been investigated: 1, 2, 3,4 and 5 m/s . Experiments in stagnant water and without water have been performed too. The excitation amplitudes have been fixed at: 0,0, 0,3, 0,5, 0,8, 1,0, 1,2, 1,5 and 1,7 mm . Even if not all the combinations of these have been investigated, every value has been chosen at least once. Note that 0,0 mm excitation amplitude has been performed in velocimetry measures in order to investigate the velocity field without perturbation. Combinations of the parameters for LDV and PIV measures are following illustrated.

Temperature (°C)	Excitation amplitude <i>mm</i>			
	0,0	0,5	1,0	1,7
15	●	●	●	●
30	2B	○	2B	○

Table 4.3: Relation between experimental temperatures, amplitudes and LDV points of measurements. **Legend:** ● → all the points of measures; ○ → any points; 2B → only point 2B.

LDV

LDV measures have been performed at 15 °C for every point, for each level, with different excitation amplitudes and different flow velocities. At 30 °C only the measures in point 2.B have been carried out, with all the velocities but only amplitudes 0,0 *mm* and 1,0 *mm*. Furthermore, field velocities higher than 2 *m/s* were not possible in points **D** and **E**. Indeed, at these velocities and at these depths inside the test section, the photodetector had some problems recording the backscattered laser pulse. Therefore at 3 *m/s* and 4 *m/s*, only measures on the points **A**, **B** and **C** have been performed. Tables 4.2 and 4.3 recapitulate the relation of the experimental parameters in LDV measures.

PIV

PIV techniques has been proven to work on Icare facility. Even if the velocimetry data are not available, the data set concerning the motion of the 2 assemblies can be investigated.

PIV measurements have been performed at fixed frequencies due to practical reasons. Indeed, the recording time for the camera was 2 *s* while the excitement lasted for 8 *s*. The camera and the hydraulic jack were not synchronized, but the synchronization was between the operators of the jack and the camera. Due to the random nature of the delay in the operators communication, the team decided to keep the frequency fixed.

The amplitude used in PIV measures are 0.5 *mm* and 1.7 *mm* with flow velocity equal to 1 *m/s*. All experiments have been performed at 20 °C. Due to climatic reasons it was not possible to perform experiments at 15 °C as the majority of tests in Small configuration. For each excitation amplitude 11 frequencies have been investigated. Due to the great heterogeneity of the parameters, the author prefers to refer the reader to the Table B.2. Table 4.4 reports the relation between amplitudes, frequencies and plane of measures without claiming to be complete.

4.1.2 Work plan

Fig. 4.1 represents the conceptual map of the experiment. The values for the experimental parameters represents the variables. Giving in input a combination of

Amplitude (<i>mm</i>)	PIV plans			
	2Y	2W	2C	3W
0,5	•	•	•	◦
1,7	•	•	•	◦

Table 4.4: Relation in PIV measures between excitation amplitudes, frequencies and plane of measures. **Legend:** • → all the frequencies; ◦ → frequencies up to 12 *Hz*.

variable, the output provided by the experiment are:

- velocity signal in time for each point of LDV measures,
- displacement signal in time of all the LVDT sensors,
- force signal in time recorder by the force sensor.

Using the power spectral density and the cross-correlation functions, it is possible to switch from time domain to frequencies domain (see subsection 2.3.2). Then, in the frequencies domain it is possible to investigate several properties of the system. Among all, this work has been focused on:

- the transfer function between the displacements of the assembly 1 and the force needed to move it;
- the estimation of the excited vibrational modes of the assembly on its resonance frequencies;
- the transfer function between the motion of two assemblies, hence their coupling;
- the transfer function between the flow velocity in the gap between the assemblies 1 and 2 and the displacement of the assembly 1.

All these properties can be exploited by means of computational tools. Before to start the data analysis, the computational code will be illustrated in the next section.

For a whole idea of the parameter combination, Table B.1 collects the majority of the experiment run on Icare in dynamic regime, both in Large and Small layout. Even if the experiments in Large configuration were conducted before the stage, the code is able to analyse data with all the reported experiments.

4.2 Code development

The computational code has been developed on Scilab. Scilab is an open source software for numerical computation providing a powerful computing environment for engineering and scientific applications¹.

¹<https://www.scilab.org>

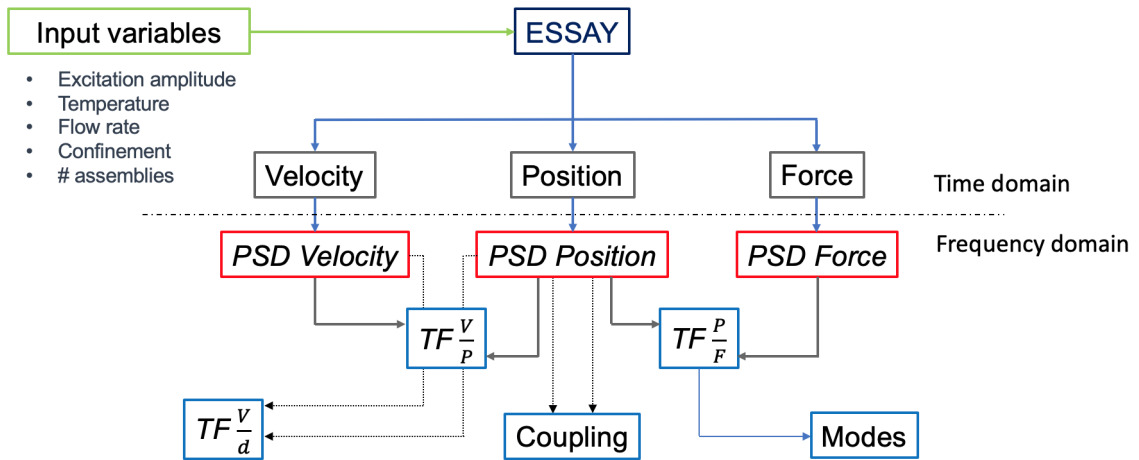


Figure 4.1: Conceptual maps of experiments.

The code uses the sampled signal of the sensors and the laser for the numerical analysis. Different functions with different purposes have been developed. For each function, the main goals are:

- *Modes.sce* computes the transfer function between the position and the force in order to identify the resonance frequencies of the excited assemblies. Once the resonance frequencies are localized, the *Modes.sce* extrapolates an oscillation period for each resonance. Then the function plots the shapes superposition of the assembly at equidistant time interval in the period.
- *Pairing.sce* computes the transfer function between the grids of two assemblies in any direction. For example between assemblies 1 and 2 along the excitation direction. Like *Modes.sce*, *Pairing.sce* identifies the resonances and plots the shape superpositions of the two assemblies for each resonance.
- *PIV_measures.sce* evaluates the coupling between the assembly 1 and 2. This function does not provide any analysis on the velocity field. Its peculiarity resides in the fixed excitation frequency. *PIV_measures.sce* computes the PSD of the position and the force, their transfer function and their coherence. The PSD of the assembly 2 central grid is computed too. Therefore *PIV_measures.sce* computes the transfer function and the coherence between the two central grids of the two assemblies, estimating the oscillation amplitude ratio and the phase delay too.
- *LDV_measures.sce* computes the PSD of the position of the central grids of the excited assembly and the PSD of the velocity signal recorded by the laser. Furthermore, the transfer function and the coherence function between these two PSDs are computed too. Differently from the previous functions, *LDV_measures.sce* allows to select several experiments and compare them. Then this function plots a single graph with all the curves of interest.
- *Icare_measures.sce* is a function that merge all the experiments. Indeed it can upload any kind of experiment. The *Icare_measures.sce* computes and

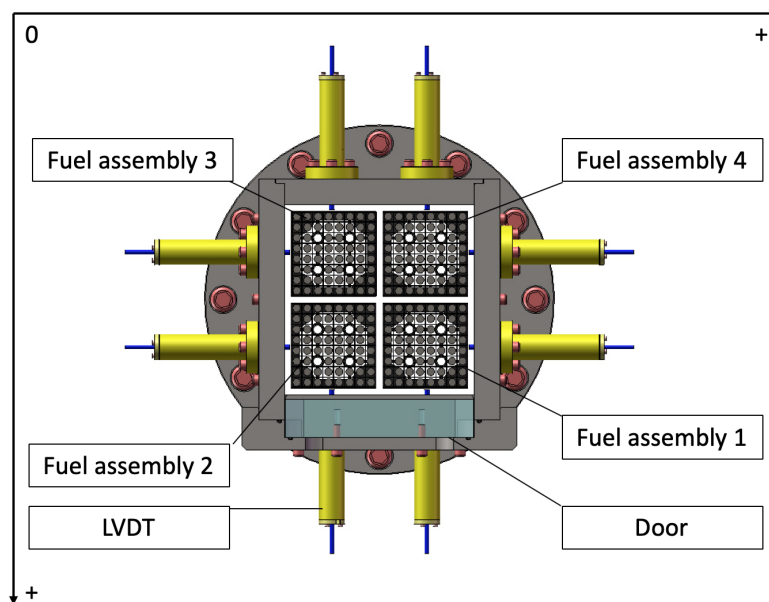


Figure 4.2: Reference system for LVDT: both the movements toward right and toward the door of the assemblies give a positive value in the in the displacement signal, vice versa for the movements toward left and toward the back wall.

plots for all the selected experiments: the PSD of the excited central grid and the exciting force, the transfer function and the coherence function between position and force of the excited assembly, the Pairing between the excited grid and the opposite one in the oscillation direction. This function upload all the data from all the sensors. Thus gives the possibility to run any kind of analysis by means of oportune instructions in the Scilab Console.

LDV_measures.sce and Icare_measures.sce interfaces are briefly showed in appendix A.

4.2.1 Acquisition e pre-treatment of the data

Before to use the experimental data in the analysis, the signal have to be treated with little precautions.

As already said in subsection 3.2.1, the signal from force and LVDTs sensor are acquired with a sample rate of 2 kHz . These data are stored in column vectors with $n = 2000$ rows for each recorded second. The signal acquired from the laser in LDV experiments is randomly sampled due to the nature of the interception process. Therefore laser data are firstly re-sampled by an interpolation method for 2 kHz and then stored in vectors.

The displacements and force vectors are set to 0 value at rest. Furthermore, the values from some LVDT sensors are changed in sign. Indeed, every sensor has its own reference system, while is oportune to have the same reference system for sensor measuring the displacement in the same direction. The LVDT gives a positive tension if the assembly approaches the wall and a negative value vice versa. Instead of having 4 reference system, one for wall, it is better having 2, one for each direction

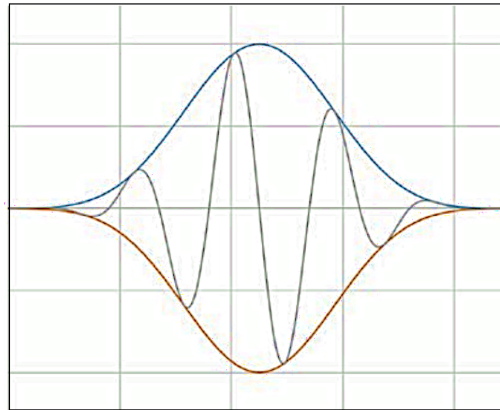


Figure 4.3: Hann window: the internal signal has its edge brought to zero by windowing.

of movement. In particular the LVDT placed in front of the right wall of Icare and those on the back wall are inverted: LVDT 04, 05, 06, 07, 12, 13, 14, 15, 20, 21, 22, 23 (see Fig. 3.3a). As shown in Fig. 4.2, the displacement values are positive if the assembly moves to right or to the door of Icare and vice versa.

4.2.2 Hann window

Once the time-domain vectors are treated, they can be used in order to evaluate the PSDs of velocities, forces and displacements. The mathematical tools to compute them are illustrated in section 2.3.2.

Although performing an FFT on a signal can provide great insight, it is important to know the limitations of the FFT and how to improve the signal clarity using windowing. Indeed, when the FFT is used to measure the frequency component of a signal, the analysis is based on a finite set of data. The FFT transform assumes that the set represents one period of a periodic signal. For the FFT, the time domain is circular topology, so the two endpoints of the time waveform are interpreted as they were connected together. In our cases the measured signal is not composed by an integer number of periods, therefore the endpoints are discontinuous.

The spectrum one get by using a FFT, therefore, is not the actual spectrum of the original signal, but a smeared version. It appears as if energy at one frequency leaks into other frequencies. It is possible to minimize the effects of performing an FFT over a non-integer number of cycles by using a technique called windowing.

Applying a window consists of multiplying the time record by a finite-length window with an amplitude that varies smoothly and gradually toward zero at the edges. As shown in Fig. 4.3, this makes the endpoints of the waveform meet and, therefore, results in a continuous waveform without sharp transitions².

Among all the window filters, in the developed code Hann window has been used. In general, the Hann window is satisfactory in 95 percent of cases. It has good frequency resolution and reduced spectral leakage. For combination of sine wave, Hann window is suggested. The PSDs have been calculated with a number of points

²Image from NationalInstrument (2019).

Chapter 4. Experimental parameters and computational tools

per windows $set_leng = 2^{15}$ and an offset of $set_step = 2^{12}$, giving an overlap of $set_leng - set_step$.

Having defined the experimental parameter and the investigation possibilities given by the computational code, it is possible now to proceed with the data analysis.

Chapter 5

Data analysis

This chapter is devoted to the analysis of the experiments. The transfer function between the imposed position and the applied force has been firstly investigated. Then the main active modes during experiments are shown. Coupling data have been retrieved before to switch to velocimetry analysis. Finally the results are underlined.

5.1 Transfer function Position/Force

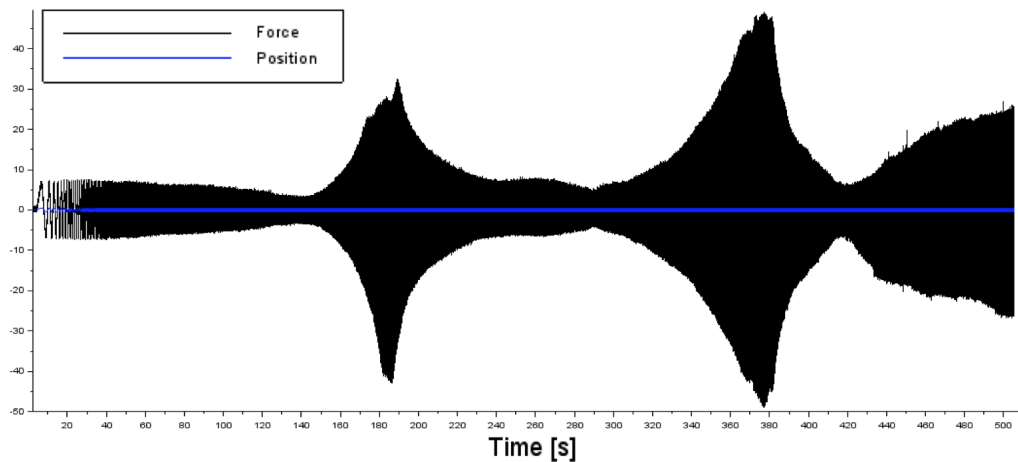
The transfer function between the displacement of the excited assembly and the applied force, allows to study the dynamical behaviour of the fuel assembly. As previously discussed in section 2.3.1, by means of the transfer function, it is possible to retrieve the coefficients of stiffness, damping and resonance frequencies. Indeed the amplitude at the starting point of the transfer function is inversely proportional to the stiffness, the peaks frequencies represents the resonance frequencies and the intensity and the width of each peak is proportional to the damping of the assembly.

In this section the analysis on the transfer function is presented varying different parameters: confinements, velocities, amplitudes, temperatures and number of assemblies. A first analysis on the dynamic behaviour of the excited fuel assembly can be performed in air. Indeed, the behaviour of the fuel assembly without any interaction with the fluid can be observed. Then, the dynamical behaviour of the fuel assembly in water (stagnant and flowing water) is analysed.

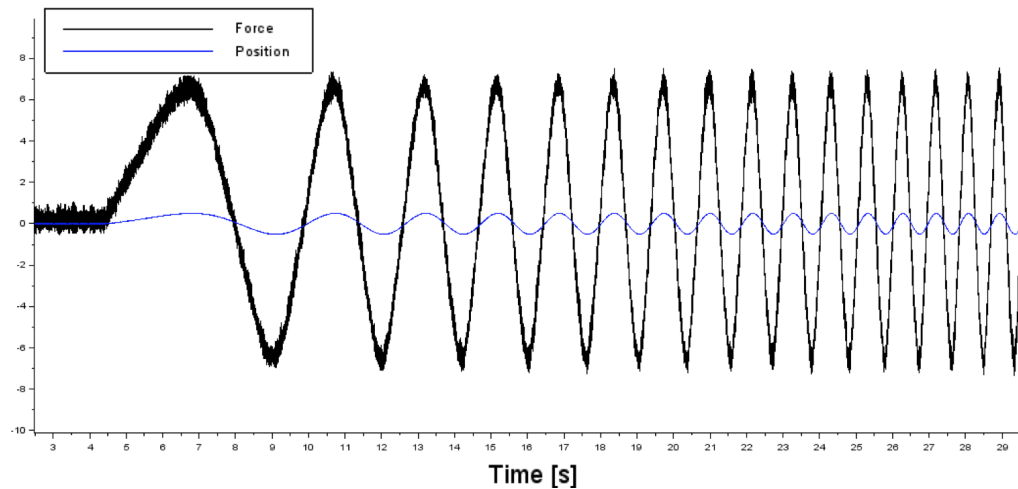
Confinement comparison

During the experiments the oscillation amplitude is kept constant and the feedback on the excitation is given by the displacement captor of the hydraulic jack. Therefore the motion is induced by means of the applied force, but the control on the motion is implemented on the displacement. Sweeping the frequencies range, the applied force varies in order to keep the excitation amplitude constant. Hence, the force signal in time has not a linear behaviour, as it is shown in Fig. 5.1a. In Fig. 5.1b, one can see that the motion of the assembly is in phase with the applied force and constant in the oscillation amplitude.

In Fig. 5.1a it is possible to note 3 valleys that begin around 120, 260 and 380 s. One can expect that these valleys correspond to the vibration in a proper mode of



(a)



(b)

Figure 5.1: a) Force and position signals in time for experiment with 2 assemblies in Large layout, without water, 0.5 mm amplitude, 15 °C; b) zoom on the lower frequencies.

the assembly. In the transfer function, these valleys corresponds to the frequencies around 6, 13 and 19 Hz, as shown in Fig. 5.3 (blue line). The vibrational mode on these frequencies will be investigated in the section 5.1.1.

Fig. 5.3 refers to the transfer function of 2 experiments carried out with the same parameters (at 0.5 mm excitation amplitude, 15 °C, in air with 2 assemblies) but in different confinement layout. As already pointed out in section 4.1.1, in the Small layout the even mode are not excited, hence the peak corresponding to the 2nd resonance frequency does not appear. In fact, the second peak of the transfer function in Small configuration overlaps with the third peak in Large configuration. This is the first and more evident difference in the comparison between the two confinement, even if it is due to experimental choices and not to dynamical aspect of the problem. If the Small layout was configured exciting the 4th grid instead of the 3rd, this difference would not be.

Another difference is a little shift between the resonance frequencies. In first analysis, this shift can not be imputed to the change of the confinement size, since

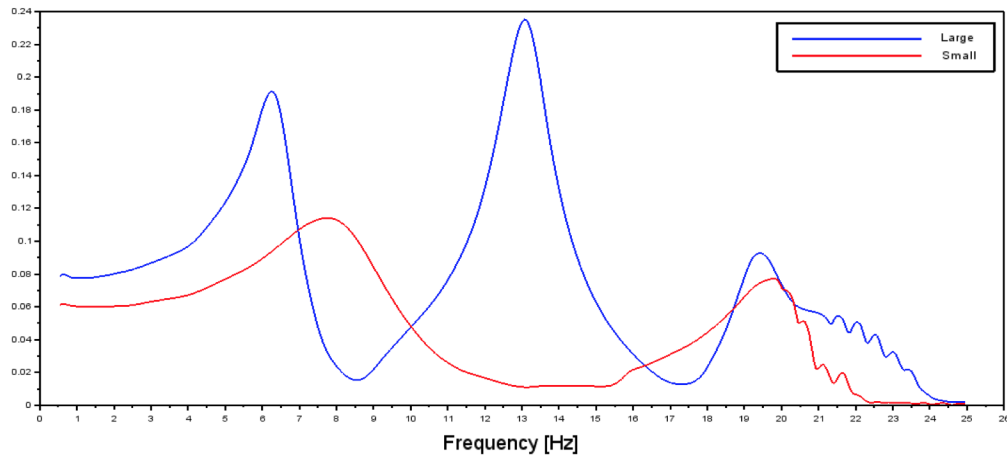


Figure 5.2: Transfer function comparison between Large and Small layouts, both at 0.5 mm amplitude, $15\text{ }^{\circ}\text{C}$, in air with 2 assemblies.

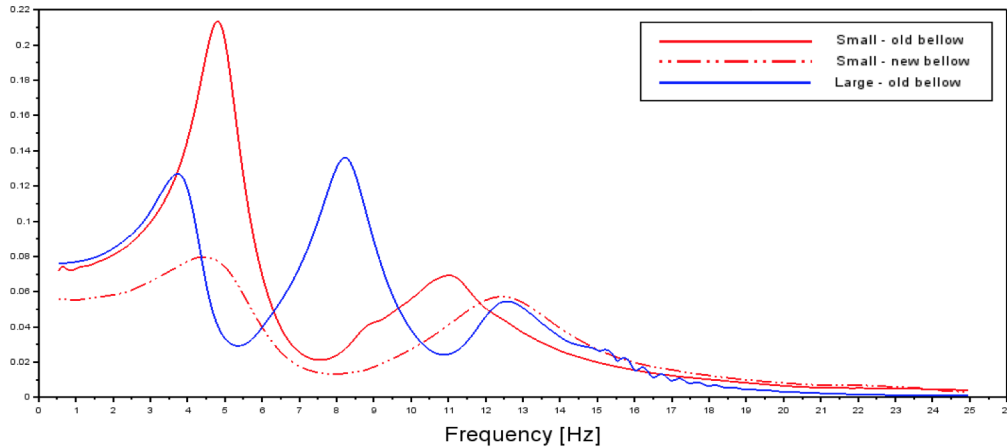


Figure 5.3: Different bellows comparison: the red lines refer to Small layout, the blue line to the Large one. Solid lines refer to experiments carried out with the old bellow, dotted line refers to the new one. The other parameters are : 0.5 mm amplitude, $15\text{ }^{\circ}\text{C}$, 2 assemblies and 0 m/s flow velocity.

these experiments have been carried out in air and hence the assembly does not perceive a real difference in the free space that surrounds it. One can think that the shift arises to the change of the bellow illustrated in section 3.3.1. Anyway, it is possible to see by Fig. 5.3 that the shift appears also in experiments in Small layout performed with the old bellow. Unfortunately, the experiment in Small layout with the old bellow have not been carried out in air. Fig. 5.3 refers to experiments at 0.5 mm excitation amplitude, $15\text{ }^{\circ}\text{C}$, with 2 assemblies in stagnant water (0 m/s). Both the experiments in Small configuration (red lines), with the old and the new bellows, present the same shift in frequencies.

Analysed in air, this shift represents a first evidence of the non linear behaviour of the assembly. Indeed, even if the even modes are not excited in Small configuration, away from the even resonance frequencies, one should expect to have the same transfer function also changing the point of excitation. Indeed a linear system the

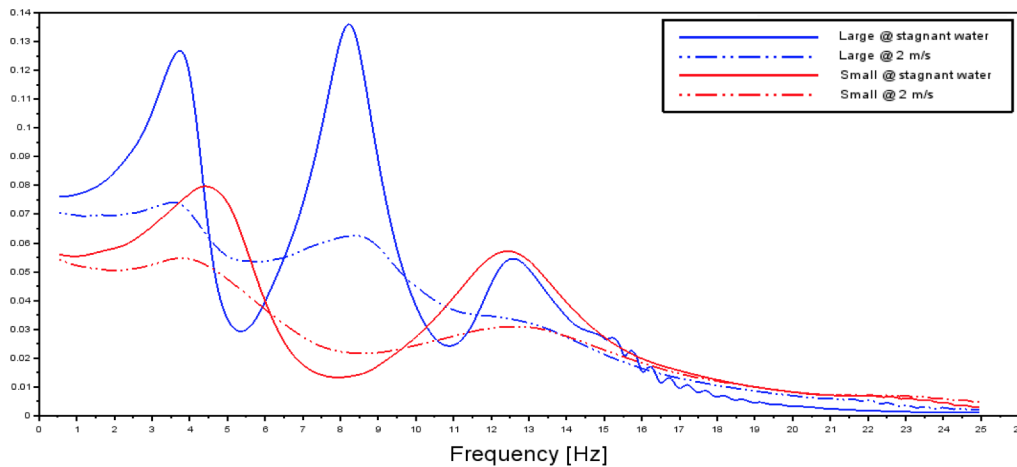


Figure 5.4: Confinement comparison . Experiment at 0.5 mm amplitude, $15\text{ }^{\circ}\text{C}$, in stagnant water (solid lines) and 2 m/s (dotted lines), in Large (blue lines) and Small (red lines) layouts.

dynamical behaviour does not depend on the excitation location. Instead, in presence of stagnant water this shift could be related to the restricted confinement size.

The main difference between Large and Small configuration is the amount of water flowing between the assemblies and between the assemblies and the walls. As already underline, this difference is not evident in absence of water. In Fig. 5.4 the transfer functions of 4 experiments are plotted. All the experiments have been performed with 2 assemblies, at 0.5 mm amplitude and at $15\text{ }^{\circ}\text{C}$; then for Large and Small layouts both the 0 m/s (stagnant water) and 2 m/s flow velocities are explored.

It is evident that increasing the water flow, the amplitude of the starting point of the transfer function decrease. Therefore, as first evidence of the fluid structure interaction, the stiffness of the fuel assembly shows a tendency to increase in Small confinement layout while the resonance frequencies are shifted when the confinement size changes. Anyway, this behaviour cannot be related exclusively to the confinement size changes, since also the excitation point is changed.

Velocities comparison

Another important evidence in Fig. 5.4 is the spread of the width and the amplitude reduction of the peaks with the increase the flow velocity. The presence of water and the intensity of the flow play an important role in the dynamical behaviour of the fuel assembly. The effects are perfectly visible in Fig. 5.5, where experiments at 0.5 mm amplitude, $15\text{ }^{\circ}\text{C}$, with 2 assemblies in Small layouts, are compared changing only the flow velocity.

One can note that there are mainly three effects in the dynamical behaviour of the assembly when the flow velocity increases: the first is a strong shift of the resonance frequencies to lower magnitudes, then the resonance peaks become more smooth and finally the stiffness slightly increases.

The resonance shift is well known in literature and it is explained by means of

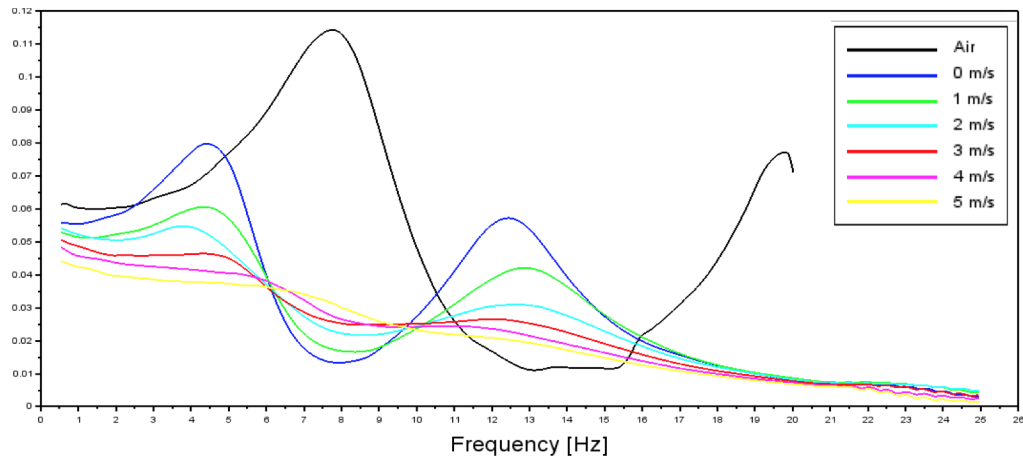


Figure 5.5: Velocities comparison . Experiment at 0.5 mm amplitude, $15 \text{ }^\circ\text{C}$, with 2 assemblies in Small layouts. Note that the experiment in air is performed from 0 to 21 Hz , while the other arrive at higher frequencies.

the added mass: the natural frequency decreases because the assembly moves part of the water mass moving itself. Thus the natural frequencies move from about 6 to 4 Hz for the first mode, from 13 to 8 Hz for the second mode and from 20 to 13 Hz for the third mode. Note that Fig. 5.5 represent experiments in Small layout, hence the 2^{mode} does not appear. In Fig. 5.6c all the three modes are represented.

The effect on the damping becomes relevant at flow velocities higher than 3 m/s . Indeed, at these velocities the resonance peaks become almost inappreciable; the dumping increases until the system appears to be over-damped. The stiffness increases with the velocity too. When the flow velocity increases, the water will oppose to the movement of the assembly itself.

For sake of completeness, other velocities comparisons are illustrated in Fig. 5.6. It is easy to see that the effects induced by the presence of the water or by its velocities are presents also for other excitation amplitude, temperatures, confinements and number of assemblies. Note that in Fig. 5.6 not all the curves end at 25 Hz ; this is due to the choice to stop first in order to investigate only the very first modes.

Amplitudes comparison

Having considered the velocity effects on the fluid-structure interaction, another important parameter that can be investigate is the excitation amplitude. Fig. 5.7 shows experiments carried out in stagnant water, with 2 assemblies in Small configuration at $15 \text{ }^\circ\text{C}$. Each curve represents a different amplitude: 0.3 , 0.5 , 1.0 and 1.7 Hz . Considering the peaks amplitude the transfer functions are very different one another. These differences prove again the non-linear behaviour of the structure. In particular, increasing the excitation amplitude, the damping and the stiffness decrease. The resonance frequencies slightly decreases too.

Fig. 5.8 shows that, increasing the flow velocity, the differences between different excitation amplitudes weaken to become inappreciable at 5 m/s .

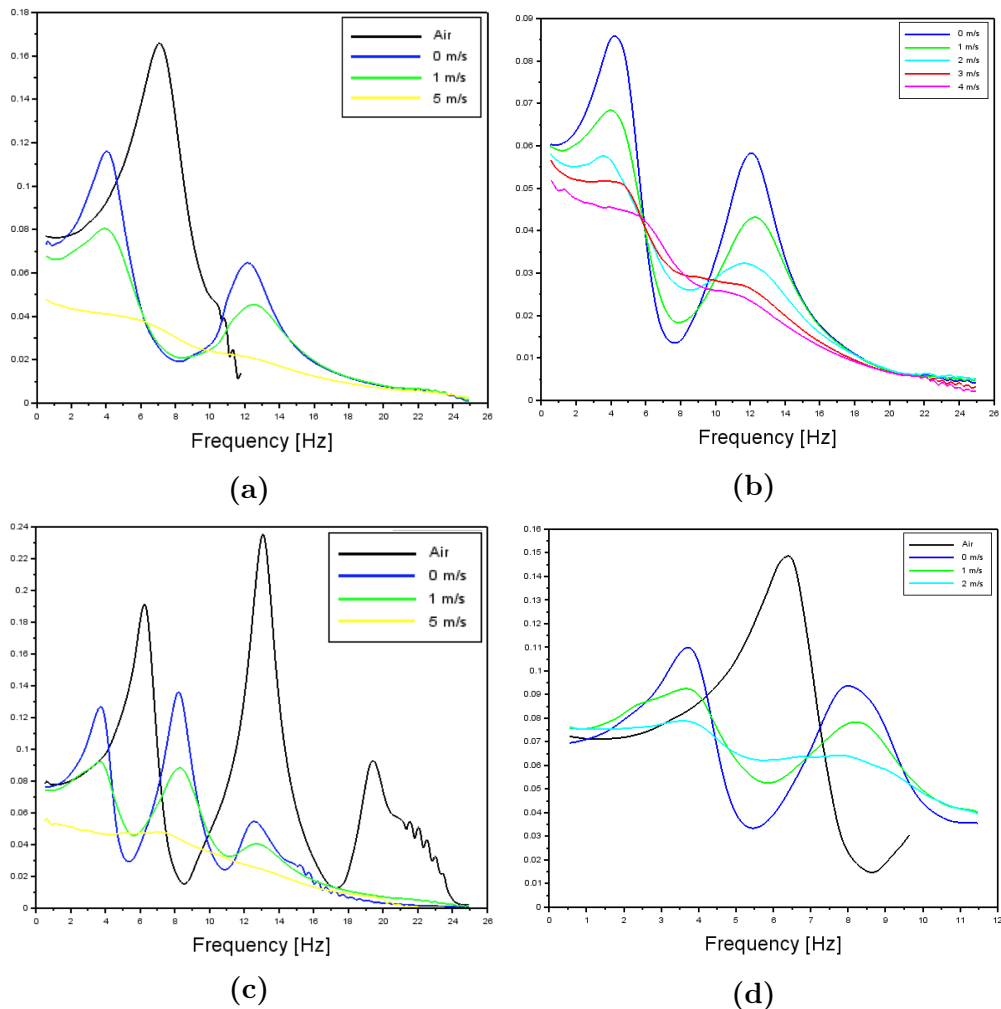


Figure 5.6: Cases for velocity comparisons. Different flow velocities for experiments at: a) 1.0 mm amplitude, 15 °C, with 2 assemblies in Small layout; b) 0.5 mm amplitude, 30 °C, with 2 assemblies in Small layout; c) 0.5 mm amplitude, 15 °C, with 2 assemblies in Large layout; d) 0.5 mm amplitude, 15 °C, with 4 assemblies in Large layout.

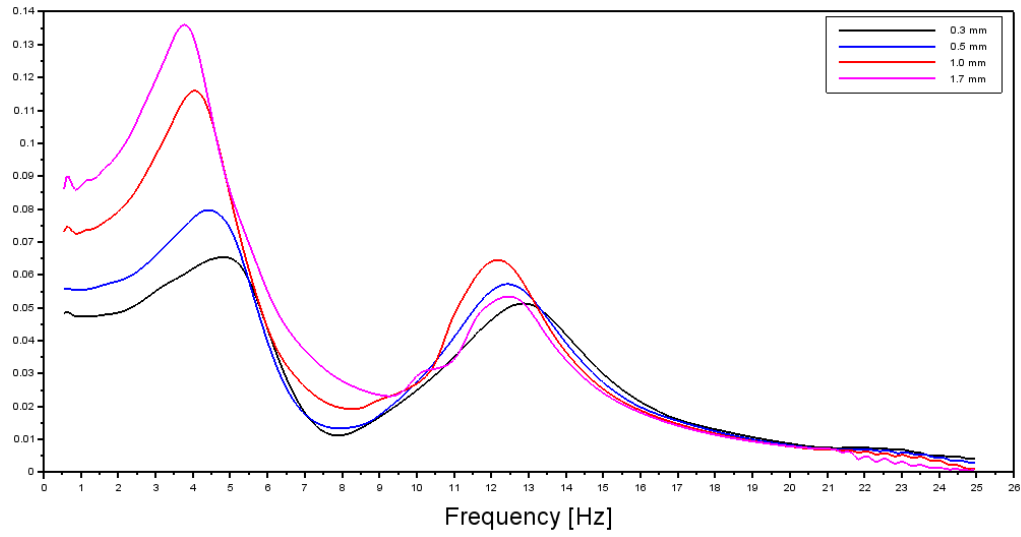


Figure 5.7: Amplitudes comparison for experiments carried out in stagnant water, with 2 assemblies in Small layout at 15 °C

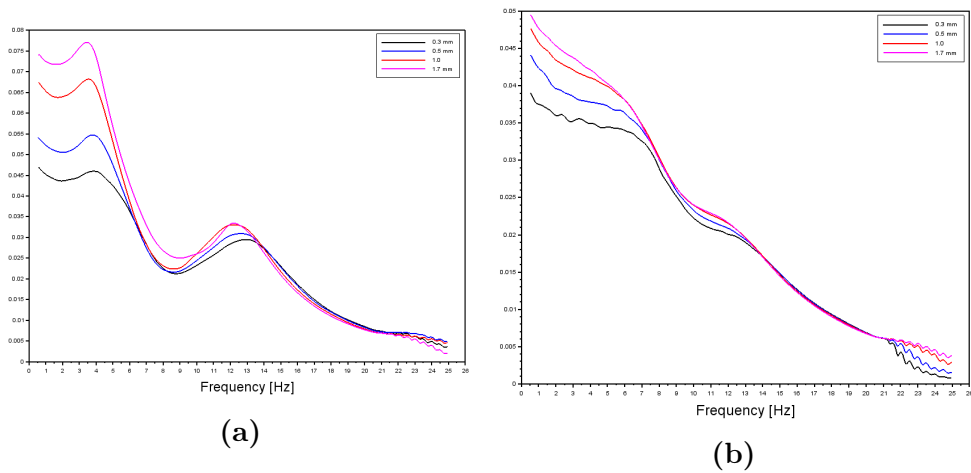


Figure 5.8: Amplitudes comparison for experiments carried out with 2 assemblies in Small layout at 15 °C at: a) 2 m/s and b) 5 m/s. It is possible to see how differences become imperceptible at high velocities.

Comparison for temperature and number of assemblies

The temperature effects are not mentioned in this discussion because of the fuel rods materials. Indeed the Young modulus of the PMMA rods is really affected from the temperature differences, thus investigation concerning the change in the viscosity and density properties of the water could lead to inaccurate results. This can happen specially if one consider the dynamical behaviour affected only by the change in the fluid properties and not in the structure. A deepen analysis is made by (Capanna *et al.* , 2019). For sake of completeness Fig. 5.9a reports experiments carried out at 0.5 mm amplitude, in Small confinement with 2 assemblies, at 0, 1 and 3 m/s of flow velocity, both at 15 and 30 °C.

The number of assemblies does not considerably affect the dynamic behaviour of the fuel assembly. Only the second mode seems to be influenced by the presence of a fuel assembly outside the direction of excitement. As shown in Fig. 5.9b, the presence of a flexible structure instead of the wall seems to increases the damping.

Explore the 4 assemblies layout is relevant because it represents better the neighbourhood condition for the assembly inside the reactor core. In section 5.2 the coupling between assemblies outside the excitement direction will be discussed.

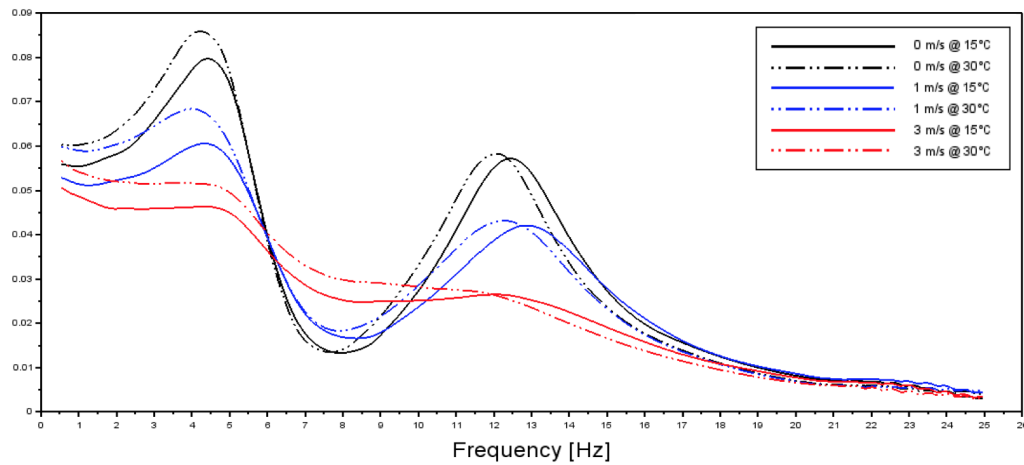
5.1.1 Vibrational modes in transfer function peaks

In this first analysis the 3 resonance peaks for Large confinement layout have been identified with the first 3 resonance frequencies and modes. The same holds for the Small configuration, with the exception that in Small confinement layout the 2nd mode is not excited, hence the second peak refers to the 3rd resonance frequency and mode. In order to understand in which percentage each mode contribute to the vibration of the structure at every frequency, a POD (*Proper Orthogonal Decomposition*) or a SWPOD (*Sliding Window Proper Orthogonal Decomposition*) analysis should be done. Due to technical reasons these have not been computed. The reader is addressed to (Clement *et al.* , 2014) and (Clément, 2014) for further information.

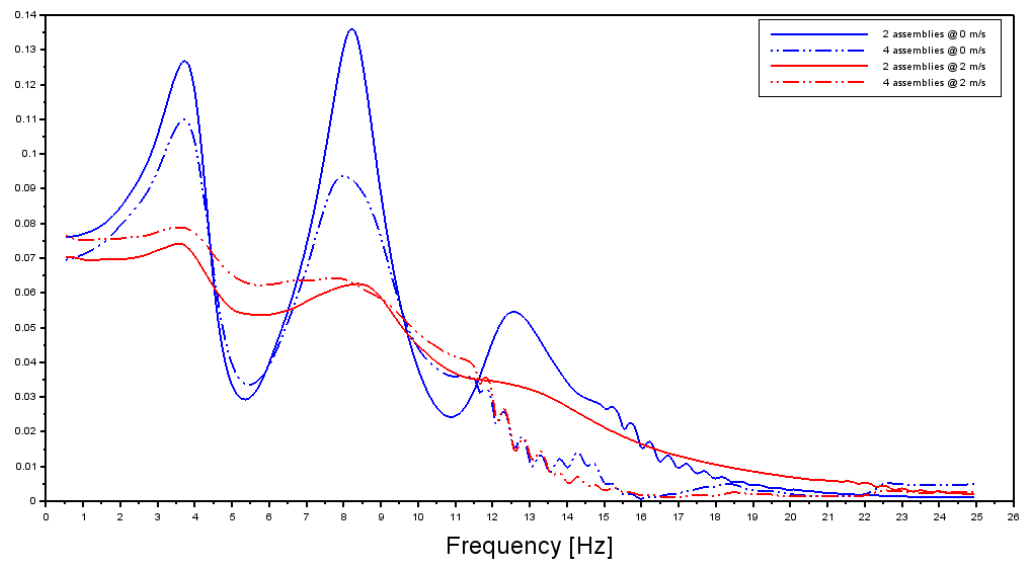
In any case, focusing on the peaks of the transfer function it is possible to extrapolate the assembly shape in different time steps along a period. Fig.5.3 shows 3 peaks for the Large confinement around 6, 13 and 19 Hz, and 2 peaks for Small confinement around 8 and 19 Hz. In Fig. 5.10 the shapes superposition for one period of each peak is illustrated. It is possible to see the prevalence of the vibrational modes corresponding to the resonance frequency. Nevertheless, since this is not a POD analysis, it is not possible to exclude the component of other vibrational modes for each peak: for example the shapes superposition shown in Fig. 5.10e look like a 3rd mode but one cannot exclude the presence of the 1st in smaller percentage.

5.2 Coupling

The experimental setup allows the study of the coupling between assemblies. The presence of the fluid between disjointed structure, couples their motion. In this section the coupling between the assemblies will be exploited. The main coupling in the structures and the effects of the different experimental parameters will be



(a) Temperatures comparison for experiments at 0.5 mm amplitude, in Small confinement with 2 assemblies, at different flow velocity.



(b) Neighbourhood comparison for experiments at 0.5 mm amplitude, in Large confinement at 0 and 2 m/s , with 2 and 4 assemblies layout.

Figure 5.9: Temperature and number of assemblies comparisons.

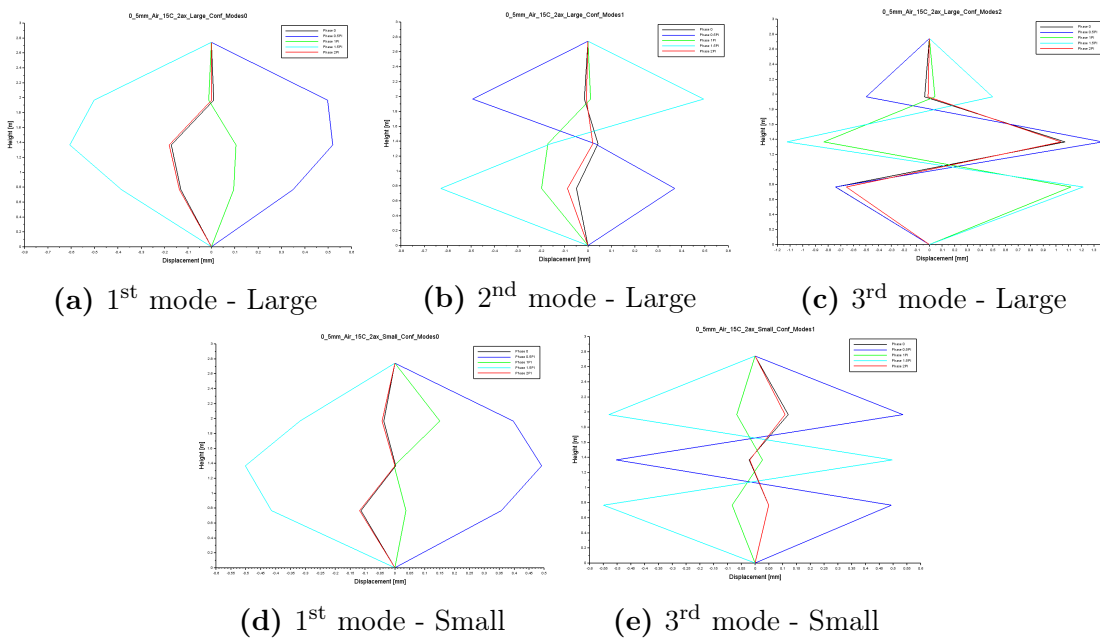


Figure 5.10: Vibrational mode at resonance frequencies. Experiments carried out in air, with 2 assemblies, at 0.5 mm amplitude and 15 °C in: a) b) c) Large configuration, d) e) Small configuration.

underlined. Experiment performed in air will not be discussed because there is not any evidence of coupling without the fluid.

One can expect to have the main coupling effect between assemblies 1 and 2 along the excitation direction. Experiment at 0.5 mm excitation amplitude, 1 m/s flow velocity, at 15 °C with 2 assemblies in Small layout, shows the time evolution and the transfer functions illustrated in Fig.5.11. These transfer functions are evaluated taking as input and output the PSD of the displacement of grids at the same level: bottom (2nd grid of the assembly), central (3rd grid) and top (4th grid). In particular, the input is given by the grid on the excited assembly, and the output is provided by the grid on the same level of assembly 2.

Another way to evaluate the transfer function is depicted in Fig. 5.12. In this case the transfer function has as input the PSD of the excited grid, and takes as output the PSD of the displacement for the Top, Central and Bottom grid of assembly 2. Obviously Fig. 5.11e and Fig. 5.12b are the same graph.

It is possible to see that the both the transfer functions, the one related to the height level (Fig. 5.11) and the one related to the excited grid (Fig. 5.12), presents the higher amplitudes corresponding to the resonance frequencies. The Central grid instead presents a peak around 8 Hz due to the excitation of the second proper mode in the assembly 2, even if this mode is not excited on assembly 1 (Small layout). The coupling is stronger between the central grids, and loses almost half of its intensity considering Bottom or Top grid.

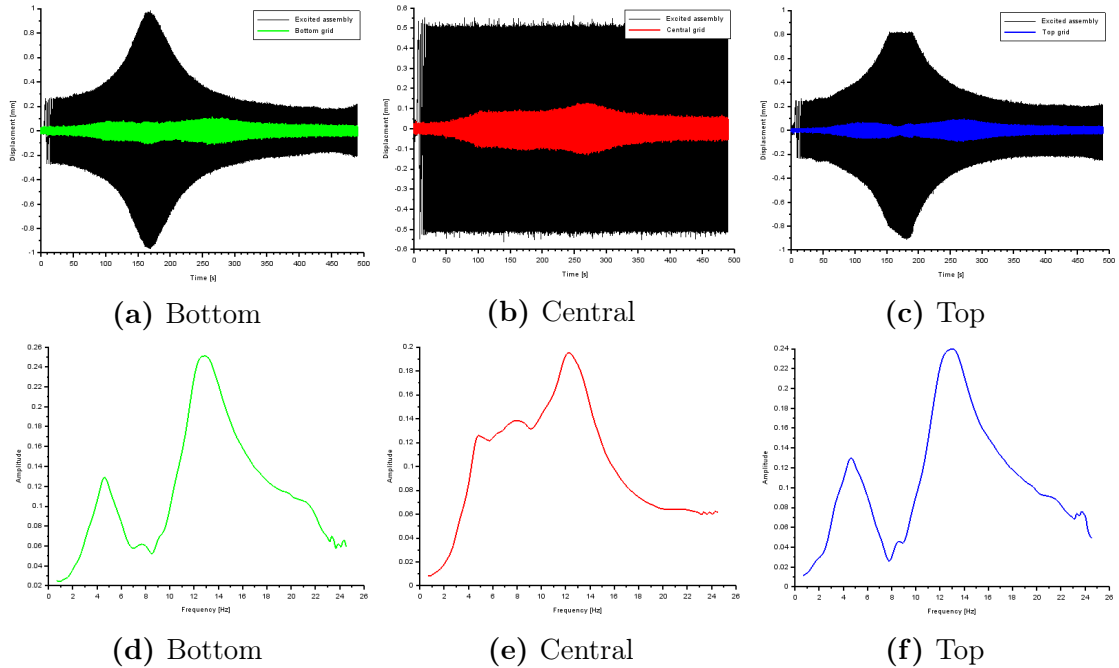


Figure 5.11: Coupling between assembly 1 and 2 on the same height level. Experiment carried out at t 0.5 mm excitation amplitude, 1 m/s flow velocity, at $15\text{ }^\circ\text{C}$ with 2 assemblies in Small layout. a) b) c) represent the recorded signal in time of the grids of assembly 1 (black line) and 2 (coloured line); d) e) f) represent the transfer functions.

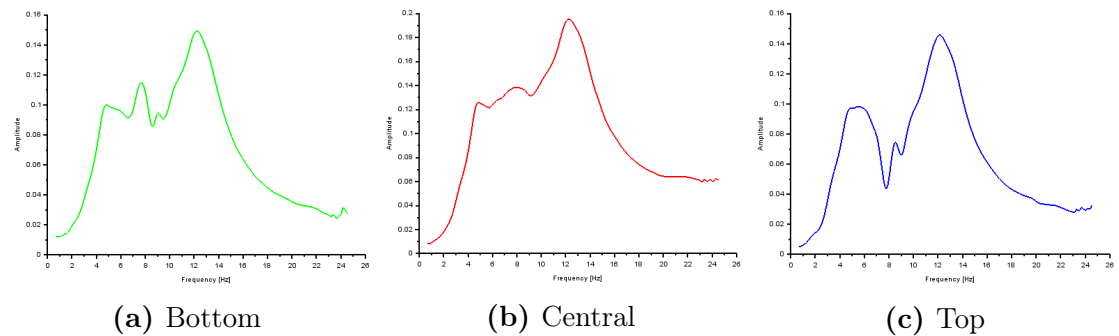
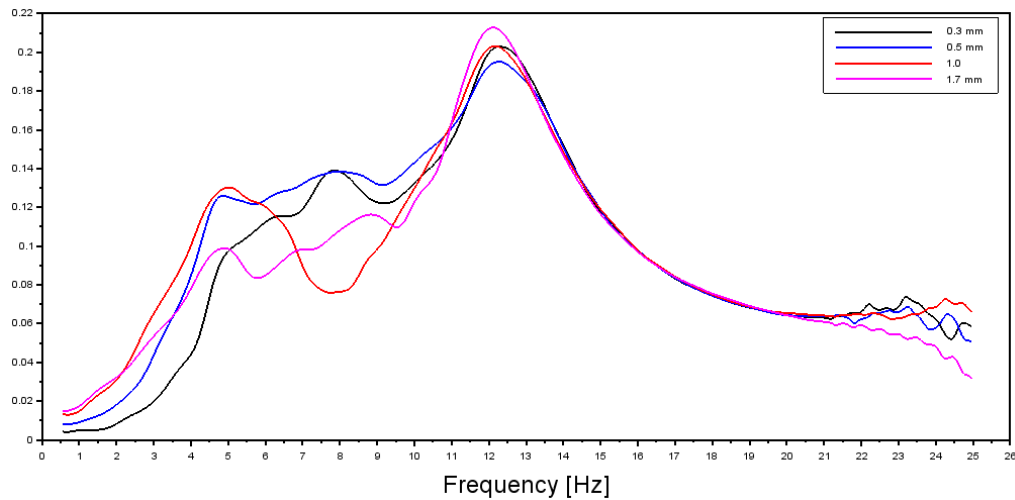
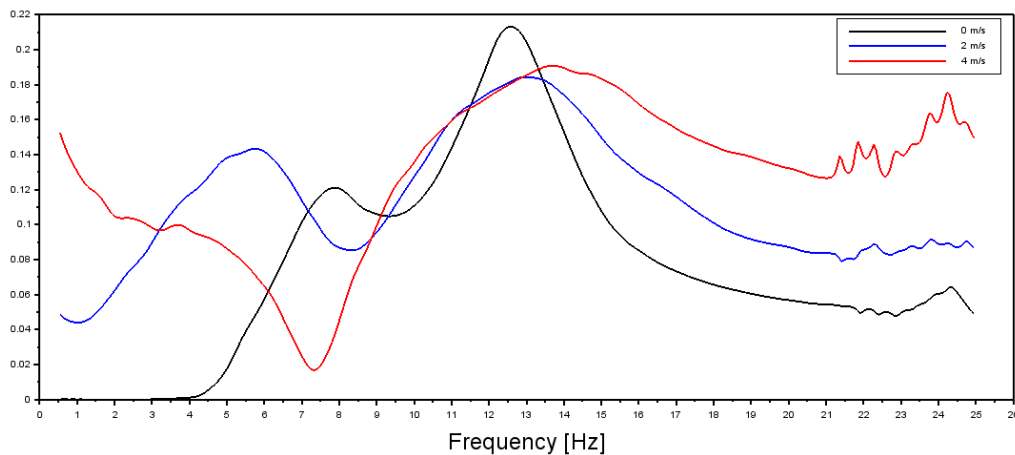


Figure 5.12: Coupling with respect to the central grids between assembly 1 and 2. Experiment carried out at t 0.5 mm excitation amplitude, 1 m/s flow velocity, at $15\text{ }^\circ\text{C}$ with 2 assemblies in Small layout. a) b) c) shows the transfer functions.



(a)



(b)

Figure 5.13: Flow velocity and amplitude effects. Experiments have carried out in Small configuration with 2 assemblies at 15 °C. a) at 1 m/s at different excitation amplitudes; b) at 0.5 mm with different flow velocities.

Flow velocity and excitation amplitude effects

The excitation amplitude does not affect considerably the coupling. As shown in Fig. 5.13a, at low frequencies there are some change but they does not define a clear tendency of the transfer function related to the excitation amplitude. Meanwhile, as shown in Fig. 5.13b, the flow velocity facilitates the coupling between the fuel assemblies at frequencies far from resonance.

Among all, in stagnant water the maximum has been found to be about 25% of the imposed oscillation amplitude (on the 3rd) and it concerned the Bottom grid at low frequencies. It raises up to 40% for a flow velocity of 4 m/s again at the Bottom grid for low frequencies. Therefore can be stated that increasing the flow velocity, the coupling between the assemblies is encouraged. The high flexibility of the PMMA assemblies makes this phenomenon more accentuated that really is in full scale fuel assemblies.

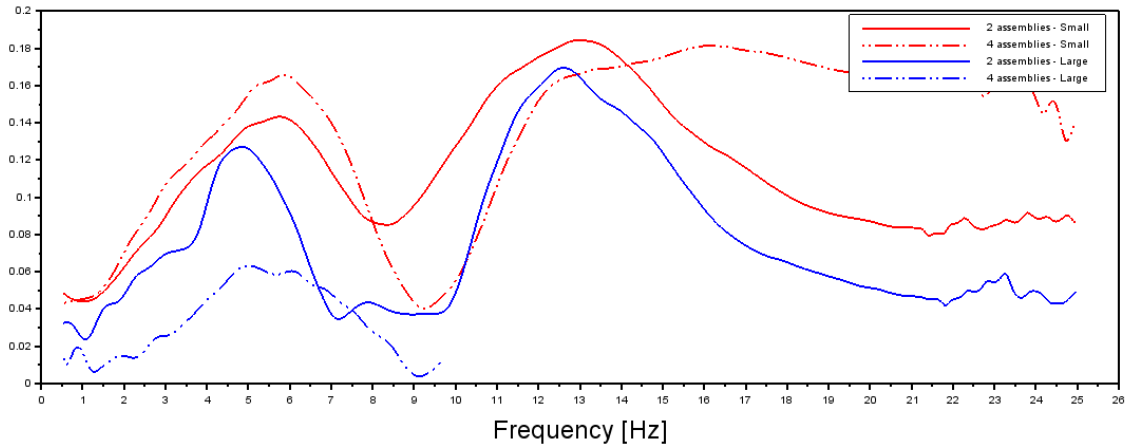


Figure 5.14: Neighbourhood effects. Experiments carried out at 0.5 mm excitation amplitude, flow velocity at 4 m/s , at $15\text{ }^{\circ}\text{C}$. Red lines represents Small configurations, while blue lines correspond to the Large layout. Solid lines are used for 2 assemblies and dotted lines for 4 assemblies.

Again in Fig. 5.13b it is shown how, increasing the flow velocity the coupling affects a wider range of frequencies. The presence of an anti-peak is underline around the 2nd resonance frequency.

Neighbourhood effects

It is clear that one should expect the major effect of the coupling at higher flow velocities. Another important effect on the coupling is given by the neighbourhood of the assembly. The number of assemblies and the confinement size can affect the fluid-structure interaction of the assemblies with the water. Fig. 5.14 shows these effects on experiments carried out at 0.5 mm excitation amplitude, flow velocity at 4 m/s , at $15\text{ }^{\circ}\text{C}$ for 2 and 4 assemblies, both in Small and Large layout.

It is demonstrated that the confinement size has a fundamental importance in the magnitude of the coupling phenomena. In Large layout (blue lines in figure) the coupling seems to be less affected by the number of assemblies present with respect to the Small configuration (red lines). Indeed in Small configuration and 4 assemblies, the anti-peak become more evident and the amplitude of the coupling transfer function at high frequencies, is higher.

Effects of neighbourhood are present all along the assembly because of the central position of the excited grid. It has been proved that when the confinement size is increased, the coupling is reduced due to the bigger distance between the assemblies.

Coupling on the orthogonal direction

Icare setup permits to study also other directions of coupling. With regards to Fig. 4.2, coupling effect can be investigate in both the excitation direction and the orthogonal one, among all the 4 assemblies. Experimental analysis made by (Capanna, 2018) on the same data set, show that there is no coherence between the displacement signals in the orthogonal direction.

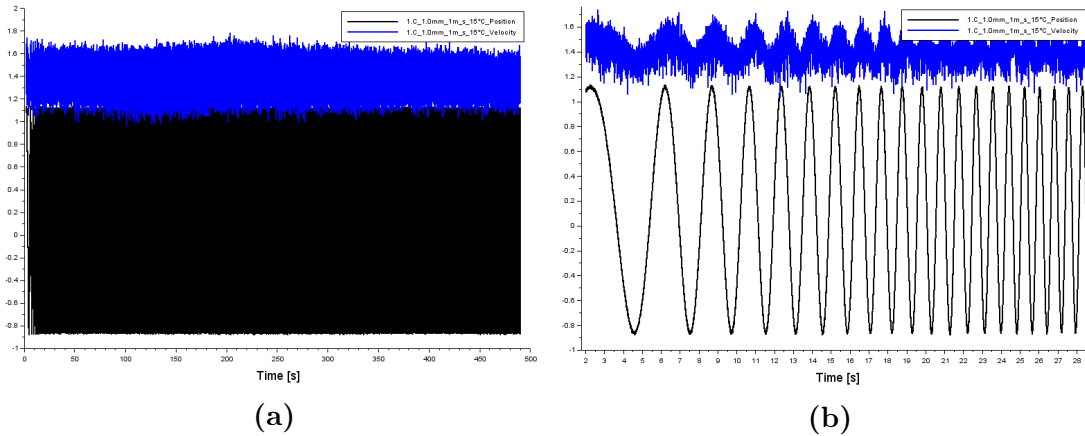


Figure 5.15: Velocity and position signals in time for: a) the entire duration of the experiment, b) initial times. Blue line corresponds to the velocity signals, while black line to the position one.

5.3 LDV

This paragraph is devoted to the analysis of the velocity field inside Icare test section. Differently from the previous analysis, this can be start from the analysis of the signals in time. Then, the PSD of the velocity and the transfer function will be discussed. All the experiments performed with LDV have been carried out with 4 assemblies in Small confinement layout. The temperature should be considered at 15 °C if not otherwise specified.

Signals in time

In Fig. 5.15 the displacement of the excited gird and the velocity time signals are shown. These plots correspond to experiment carried out at 1.0 mm amplitude, flow velocity at 1 m/s in point 1.C . From Fig. 5.15b it is possible to see how the displacement of the excited grid influences the velocity field. Even if there is some noise, zooming on the frequencies, velocity oscillation can be detected. This is a good reason to spread the LDV experimental campaign and its data analysis.

On the time domain, the experimental analysis unavoidably fallen into the comparison between velocities. Fig. 5.16 reports experiments at 1.0 mm amplitude in point 2.C, with flow velocity at 1, 2, 3 and 4 m/s. The first consideration concerns the oscillation amplitude of the signals, since it seems to be proportional to average velocity. This is reasonable, since the perturbation in the flow is amplified when the average flow rate increases. Also the noise increases with the flow velocity, and this can be explained because of the higher turbulences provided by higher velocities. Analysis of the same experimental parameter but without any excitation amplitude, confirms that the noise is due only to the average velocity magnitude.

Again fro Fig. 5.16 one can note that the measured velocity is every time higher than the nominal one. This is because the nominal velocity refers to whole Icare test section, while the measured velocity refers to the field between the assemblies. The water flows in Icare test section both inside the assembly and in the gaps between

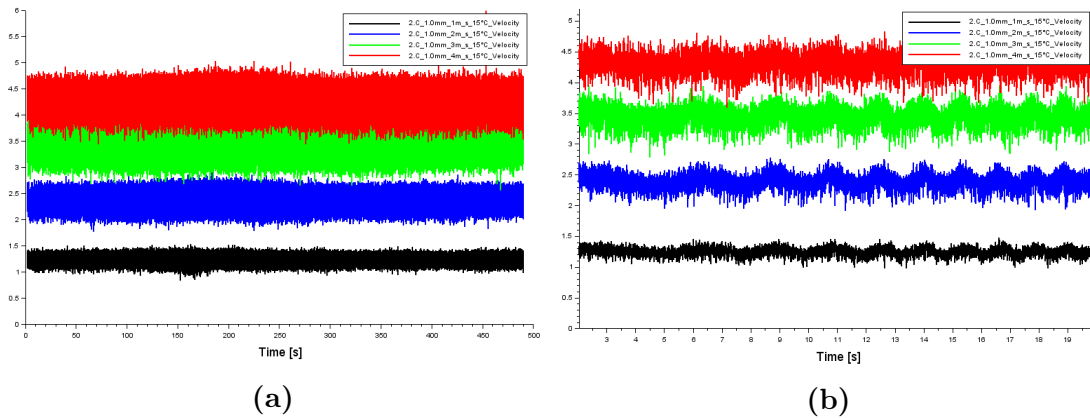


Figure 5.16: Comparison on velocity signals in time for: a) the entire duration of the experiment, b) initial times. The flow velocity varies from 1 up to 4 m/s .

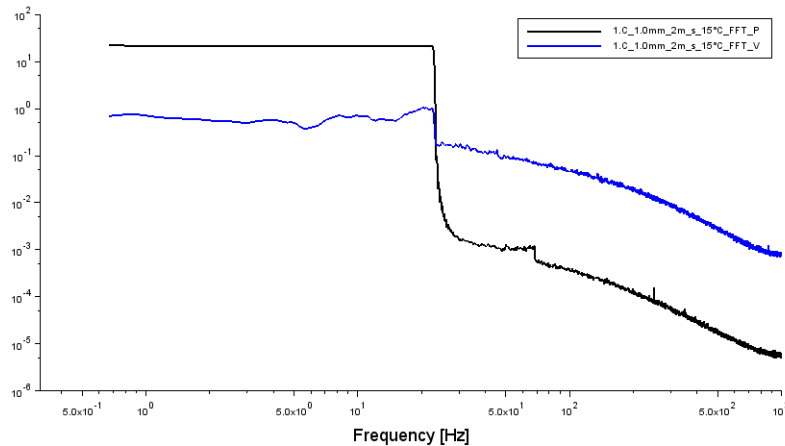


Figure 5.17: PSD of the velocity (blue line) and position of the excited grid (black line). 1.0 mm amplitude at 2 m/s in 1.C point

them. Since the gap present a larger hydraulic diameter, the measured flow velocity results to be stronger.

The possible analysis on time domain are confined to what it has just discussed. Again, the frequencies response can be an useful tool for investigate the physics of the involved phenomena

5.3.1 Transfer function Velocity/Position

The PSD of the displacement of the excited grid and the flow velocity are illustrated in Fig. 5.17. This experiment refers to 1.0 mm amplitude at 2 m/s and has been measured in 1.C point. It is possible to note that both the curves has a drop around 25 Hz , that is the maximum excited frequency. This can demonstrate that the oscillation in the velocity field are due to the displacement of the excited grid. Furthermore the PSD of the position presents a little jump around 70 Hz ; it refers to the electrical noise in the command line of the hydraulic jack, therefore it is out of the context of the present analysis.

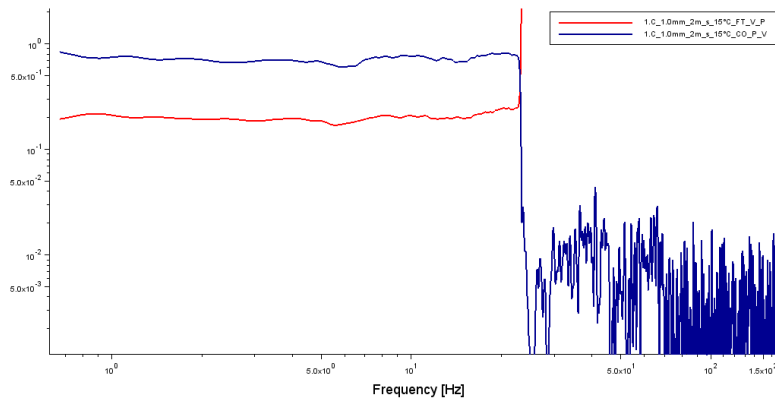


Figure 5.18: Transfer function (red line) and coherence (blue line) between velocity and position of the excited grid . 1.0 mm amplitude at 2 m/s in 1.C point

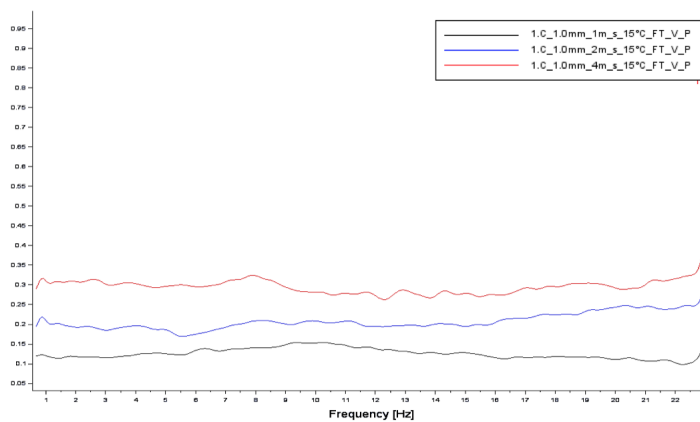


Figure 5.19: Transfer function for different flow velocities. 1.0 mm amplitude in 1.C point.

The transfer function between the velocity and the position (from now on 'position' refers to the displacement of the excited grid) are illustrated in Fig. 5.18. It is possible to note that the coherence is very good and well approximate the unit. This is the confirm that the oscillation in the velocity field are due to the displacement of the excited assembly. The transfer function diverges for frequency values higher than 25 Hz because the PSD of the position goes to 0. Since the PSD of the position is somehow at the denominator of the transfer function, this latest diverges up to infinity.

Water flow effects

In the time domain analysis, it has been shown how the magnitude of the bulk velocity influences the velocity field oscillation. In Fig. 5.19 this behaviour is presented on the frequency domain. Indeed the transfer functions absolute value increases with the increasing of the average flow velocity. It is not evident any direct proportionality between the increases of the amplitude of transfer function and the water flow rate. Therefore non-linear behaviour results also in velocimetry analysis.

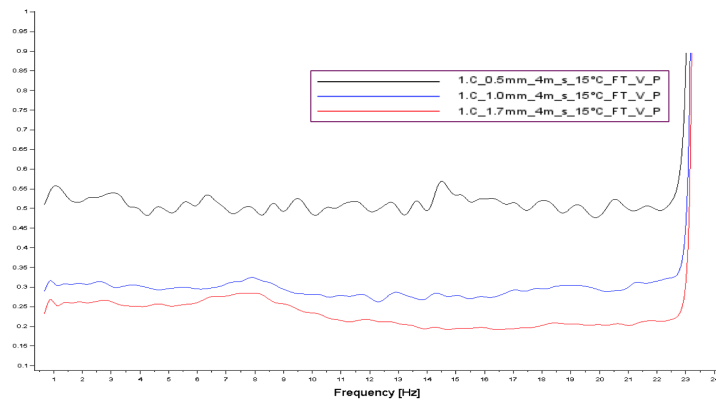


Figure 5.20: Transfer function for different excitation amplitude. 4 m/s flow velocity in 1.C point.

It is important to underline that the non linear behaviour of the transfer function changes with the points of LDV measures. This is due to the different hydraulic diameter in the test section of Icare: measurements taken closer to walls have a larger perturbation of the local ow velocity than the ones taken at middle depth of the fuel assemblies.

Excitation amplitude effects

Looking at Fig. 5.20, it is possible to see that the transfer function decreases increasing the excitation amplitude. This means that the flow velocity is more influenced by the movement of the assembly when the displacement is small. The structure response is not linear also with respect to this parameter since its frequency response is not proportional to the variation of excitation amplitude.

Even if the amplitude of the induced oscillating flow increases with the increase of the excitation amplitude, there is not a direct proportionality relationship. It can be seen that the transfer function between the local velocity and assembly positions are not superimposed. It is higher for smaller amplitude excitations, and it decreases as the excitation amplitude increases. This means that the energy introduced in the system by small amplitude oscillations is transferred to the fluid in a more efficient way than the energy introduced by large amplitude excitation.

Analysis on the points of measure

The last parameter that can be changed are the points of measure. As illustrated in section 3.3.2, LDV measures have been performed on 10 points, dislocated on 2 height level.

Fig. 5.21 shows the transfer function evaluated for the 2 levels.

Transfer functions are not affected in a significant way from the measurement locations. This is more specifically true for the measurement point located below the excitation grid (Fig. 5.21b), while transfer functions related to the measurements taken above the grid are more spread out.

This effect, higher in deeper points is probably due to the presence of the grid

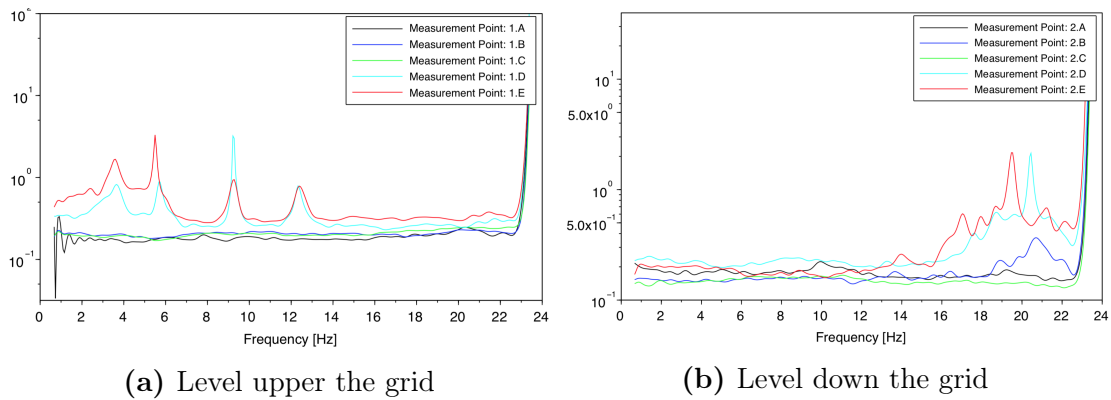


Figure 5.21: Comparison of the transfer function V/P related on different points of measure: a) on level 1, b) on level 2. Experiments carried out at 1.0 mm and 2 m/s flow velocity.

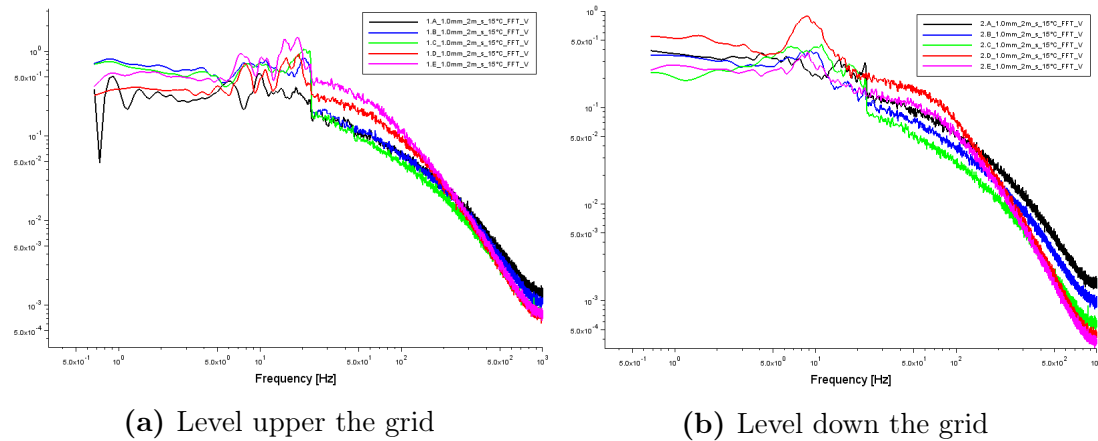


Figure 5.22: Comparison of the velocity power spectral densities related on different points of measure: a) on level 1, b) on level 2. Experiments carried out at 1.0 mm and 2 m/s flow velocity.

itself, which perturbs the flow introducing turbulence and edge effects. Furthermore, the errors in the alignment of the laser parallel to the assembly can introduce some variations on the measured values of the velocity oscillations since the distance between the measurement point and the fuel assemblies can change.

From the velocity power spectral densities illustrated in Fig. 5.22, it is possible to observe differences in the magnitude of the velocities between the height levels. Fig. 5.22a and 5.22b show the tendency of the velocity PSD among the points in depth, for experiments carried out at 1.0 mm and 2 m/s flow velocity. Water velocity is slightly larger for the measurement points located above the grid than for the ones located below the grid. This tendency is outlined also in Fig. 5.23. The represented velocities are the average of all the velocity measures taken for each point.

Moreover, the velocity profile is not uniform along the depth. Velocity profile has a maximum for the measurement points located next to the walls, while it decreases for the points located in the middle of the fuel assemblies. The gap between the fuel assemblies and the wall has an hydraulic diameter which is larger than the one in

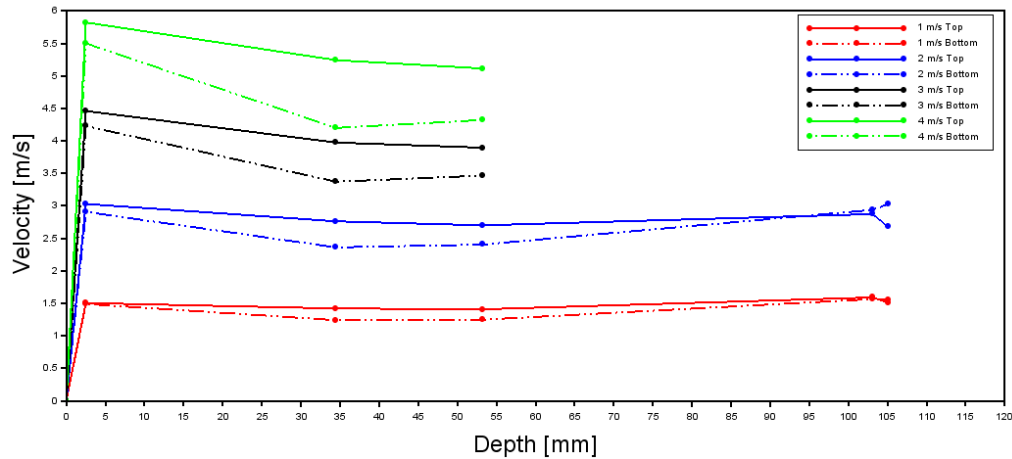


Figure 5.23: Average behaviour of the velocity with respect to height and depth

between the assemblies, thus it justifies the water velocity to be larger in the gap between the walls and the assemblies. This assumption is valid if the measurements are performed within a distance large enough to avoid the boundary layer, where the velocity profile rapidly decreases.

5.4 Comments on experimental results

With this chapter the data analysis of the experimental campaigns, have been presented. Here the main results are outlined.

The dynamical behaviour has been proved to be non-linear. Indeed the transfer function between the displacement and the applied force has not the same behaviour with respect to each resonance frequency, neither with respect to the location of the excitation point. The first resonance frequencies have been find to be around 4 Hz , 8 Hz and 13 Hz in stagnant water with the tendency to decrease increasing the flow velocity. These came out to be very similar to the real frequencies of a full scale assembly. Temperature effects have not been considered because of the Young modulus of the PMMA rods. It is not possible to identify which effect is due to the temperature difference and which to PMMA properties change. It is possible to consider both the causes simultaneously.

Concerning the coupling between the assemblies subjected to an axial flow, the displacement induced on the non excited ones have been investigated. In particular the discussion has fallen on the major influenced assembly, that is the opposite one, assembly 2, in the excitation direction. The coupling strongly depends on the water flow rates, and it increases as the water flow rate increases. At the best condition (Bottom grid, high flow velocity), the motion induced by coupling can reach values of above 40 % of the external imposed displacement, while it has been shown that also in stagnant water the coupling effects are not negligible.

With regard to LDV experimental campaigns, measurements show that an induced oscillating axial flow appears over the same excited frequency range of the assembly. The amplitude of such oscillations strongly depends on the intensity of the average

fluid velocity with a non linear behaviour. In fact the higher the mean velocity of the water flow is, the higher is the relative oscillation of the fluid velocity. This result also explains the coupling between fuel assemblies becoming stronger for large water flow velocities. On the other hand the amplitude of the fuel assembly excitations affects the induced axial flow in an opposite way. As the excitation amplitude increases, the induced velocity oscillations are smaller in intensity (relatively to the excitation amplitude). Such a behaviour is probably due to dissipation forces (viscosity for instance) which have a stronger effect on larger amplitude oscillations. No important effects are visible on the induced axial flow as the temperature changes.

Finally, the comparison between measurements taken in different points of the water domain confirms that the flow is not uniform over the test section. In particular an axial redistribution occurs due to the inlet nozzle system, causing the flow to considerably change in intensity as we move along the axial direction on the test section. Moreover the water flow is measured to be stronger in the bypasses next to the walls than in between fuel assemblies, as expected.

To conclude this chapter it is needed to underline a last aspect. One can note that any analysis concerning measurement errors and their propagation have been done. The author is aware of it and there are mainly two reasons that can be stated. From a first point of view, this is due to the high precision instrument used carrying out the experimental campaigns (see section 3.2.1). But the real reason is due to systematic errors inherent the measurement methods. Indeed, even if there was the possibility to check if the assemblies were perfectly upright or not, there was not the possibility to correct their eventual flexions. Thus, every measure is effected by a systematic random error on the initial condition on the fuel assemblies position. These systematic errors are stronger than the instrumental ones.

Chapter 6

Conclusions

6.1 Conclusions

The present document reports the main results obtained during the internship period at CEA Cadarache in the LTHC lab in January-July 2018. The main motivations leading to this work and the theoretical background have been clarified in the first and second chapters. The previous setups have been briefly illustrated focussing on the main advantages and drawbacks. The employed facility (Icare experimental) and the modifications needed in order to perform the new experimental campaigns have been deeply illustrated. Part of the large amount of experimental data collected on the facility have been analysed. The computational code developed has been presented with its main functions and their goals. All these functions have the key-benefit to be user-friendly: their simple and complete interface give access to any kind of experiments. In this way analyses on the experiments carried out on Icare can be performed even if Icare has been disabled.

Concerning the dynamic analysis, it has been focused on the transfer function between the displacement of the assemblies and the applied force, as well as on the coupling between the assemblies subject to an axial flow and on the velocity field measure by LDV techniques. All these analyses have been performed with respect to the change of parameters such as the excitation amplitude, the flow velocity, the confinement size, the number of assemblies in the neighbourhood and the temperature.

From both the dynamical analysis and LDV measurements the non linearities of the system emerged. These are mainly due to the presence of support grids, which with their springs and dimples induce the assembly to deviate from the linear behaviour.

These data analyses have been used by (Capanna, 2018) in his PhD project, in which the experimental data are used in order to estimate physical parameter such as added mass, added stiffness and added damping resonance frequencies. The main goal in that context is the validation of the simplified model for fluid-structure interaction illustrated in section 2.2. Furthermore, they have been used in the article by Capanna *et al.* (2019).

The PIV experiments have been carried out in a context of cooperation with the *George Washington University*. The data analysis of these experiments will be

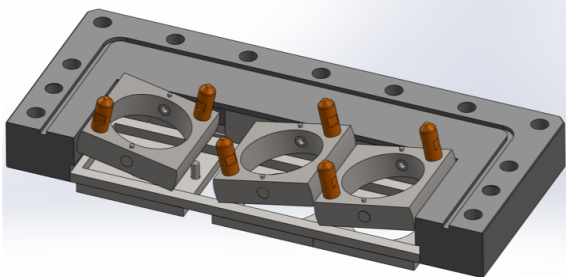
presented at the 18th International Topical Meeting on Nuclear Reactor Thermal Hydraulics *NURETH-18* by means of the article *TIME-RESOLVED PARTICLE IMAGE VELOCIMETRY BETWEEN TWO PWR SUB-BUNDLES*, of which the author of this thesis is co-author.

6.2 Future perspectives

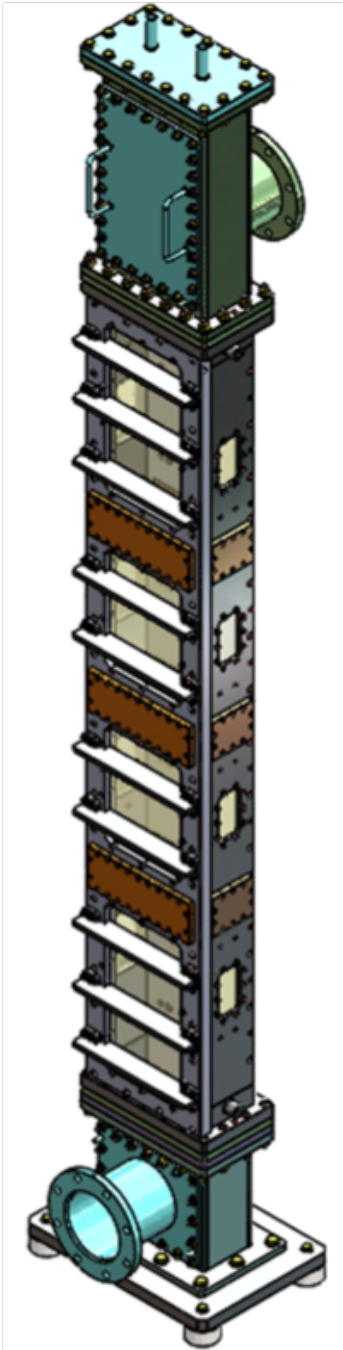
The huge amount of collected data allows further analysis, in particular concerning the flow velocity. In particular, one could think to search for a correlation between the area variation in the gap of the assemblies and the recorded flow velocity. Velocity decomposition analyses could be performed, too. Finally, an analysis based both on PIV and LDV could add new contributes to the study of the velocity field. With regard to non linear behaviour of the fuel assemblies, relevant information could be provided by the SWPOD analysis. In the general context, new models both for the core and for the fuel assembly could be developed.

The author of the thesis will start a PhD project in the LTHC Laboratory for the development of another model for the PWR core based on the porous medium approach. This model will be investigated with the aid of the new experimental setup Eudore. This new experimental facility has been recently designed and installed. Eudore, designed by Bouzet (2018) and represented in Fig. 6.1b, has replaced the Icare setup. It uses the same assemblies used in Icare but with three assemblies arranged in a row, on which a pre-deformation could be imposed by means of 2 plates integrated to the PIC and PSC. As we can see from Fig.6.1a Bouzet (2018), both these 2 plates contain 3 bases to hook the fuel assemblies. These bases can be turned in order to impose an independent bending on each fuel assembly. Another peculiarity of this new facility is that the whole structure can be excited with a hydraulic system, exploiting the possibility of applying seismic excitation to the entire test section. Furthermore, laser distance sensor will be used on Eudore to measure the movements of the assemblies. The developed instrumentation makes it possible to measure the displacements of the assemblies, the wall pressure fluctuations, the impact forces and the velocity field of the fluid by optical techniques in dynamics. Many parameters can be modified to observe the effect on the dynamics of the system.

For future projects, the results coming from this new experimental facility could be compared with the data collected on Icare and the potential flow model could be used to perform calculations on this new geometry, taking into account viscosity effects and the motion of the walls.



(a) Bottom plate for Eudore



(b) Eudore facility: this modurable setup houses 3 half-scale fuel assemblies in row

Figure 6.1: Eudore facility

Appendix A

Scilab

In this appendix it is briefly explained how the function developed for the data analysis work.

A.1 `Icare_measures.sce`

`Icare_measures.sce` allows to upload the data file for each experiment that we want to compare. The command windows will continue to appear until the confirmation to stop: each time it is asked if all the desired experiments have been added or if the operation must be further iterated. For each selected experiment all the parameters are displayed on the Console (see Fig. A.2).

Then `Icare_measures.sce` plots:

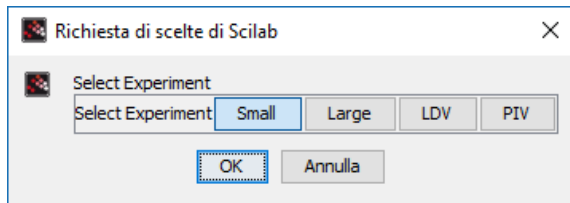
- the Transfer function between Position and Force of all the experiments,
- the Coherence between Position and Force of all the experiments,
- the PSD of all the Positions,
- the PSD of all the Forces,
- the Pairing between the excited grid and the opposite one in the excited direction for all the experiments.

For example, selecting the experiments showed in Fig.A.2, the function plots: (see Fig. A.3)

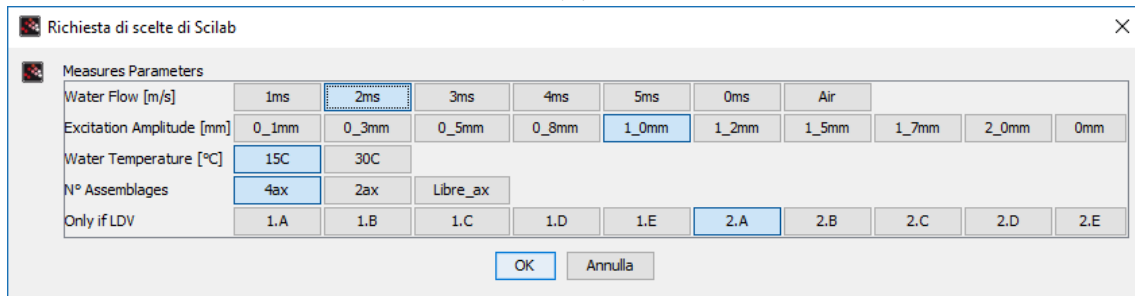
Since this function allows to compare a huge quantity of data, it is impossible to predict any kind of title for the graphs. Furthermore, this function does not save the 5 graphs already shown; its aim is to load all the data from the experiments. From the input window in Scilab it is possible to plot and save any kind of graph.

`Icare_measures.sce` uses the following satellite functions:

- `Correct.sce`
- `fonc_trans.sce`
- `igetfile.sce`
- `Give_me_Addrress_P.sce`
- `Address.sce`
- `Experimental_parameter.sce`
- `Load_parameter.sce`



(a)



(b)

Figure A.1: Command window for Icare_measures.sce: a) window to select experiment type; b) window to select experimental parameters

```

Bienvenue!

Upload Address

Upload External Functions

!For experiment 1 selected: Small !

  Datas for experiment 1 1_0mm 2ms 15C 4ax 2.A

!For experiment 2 selected: Small !

  Datas for experiment 2 1_0mm 2ms 30C 4ax 2.A

!For experiment 3 selected: Small !

  Datas for experiment 3 1_0mm 2ms 15C 2ax 2.A

!For experiment 4 selected: Small !

  Datas for experiment 4 1_0mm 2ms 30C 2ax 2.A

!Find address for experiment 1 !

!Find address for experiment 2 !

!Find address for experiment 3 !

!Find address for experiment 4 !

```

Figure A.2: Console output with the experimental parameters informations

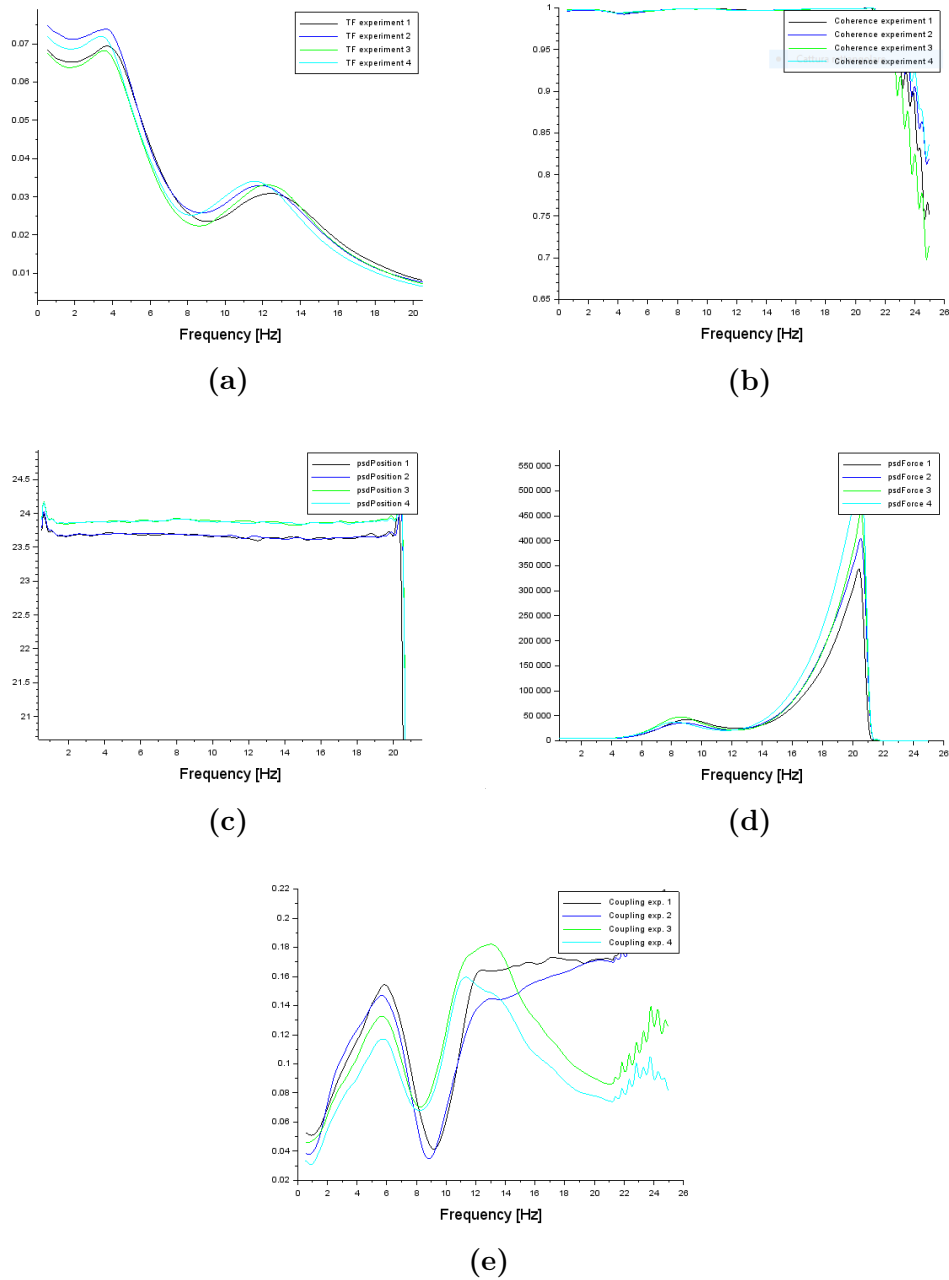


Figure A.3: Icare_measures.sce graphs: a) Transfer function; b) Coherence; c) PSD of the positions; d) PSD of the force; e) Pairing between the excited grid and the opposite one

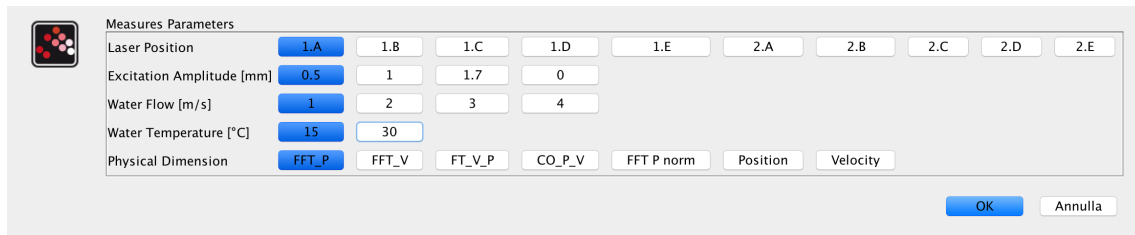


Figure A.4: LDV_measures.sce command window

- Load_data.sce
- Plottali.sce

A.2 LDV_measures.sce

LDV_measures.sce is a function concerning LDV experiments. It allows to select different experiments and compare them. For each experiment, LDV_measures.sce gives access to the:

- Power spectral density of the Position (**FFT_P**),
- Power spectral density of the Velocity (**FFT_V**),
- Cross-Correlation FFT_V/FFT_P (**TF_V_P**),
- Coherence Function PSD_V/PSD_P (**CO_V_P**),
- Normalized power spectral density of the Position (**FFT P norm**),
- **Position** vs time signal,
- **Velocity** vs time signal.

In Fig. A.4 represents the command window: all the experimental parameters can be selected from there.

It is possible to compare whatever number of experiment thanks to a "while" loop cycle that the user can be stop as soon as all the experiments have been selected. This function uses the following satellite functions:

- givemematrix.sce
- givemegoodpoint.sce
- Graph_2D.sce
- Graph_2D_color.sce

Appendix B

Tables of Experiments

The following table does not contain all the experiments; still, it is a useful guideline to compare experiments performed in similar conditions.

Main Table of Experiments

Confinement	# Assemblies	Velocity [m/s]	Temp. [°C]	Excitation Amplitude [mm]							
Large (jack on 4 th grid)	4	0	15	0.1	0.3	0.5	0.8	1.0	1.2	1.7	2.0
		1	15	0.1	0.3	0.5	-	1.0	1.2	1.7	2.0
		2	15	0.1	0.3	0.5	-	1.0	1.2	1.7	2.0
		3	-	-	-	-	-	-	-	-	-
		4	-	-	-	-	-	-	-	-	-
		5	-	-	-	-	-	-	-	-	-
	Air	15	0.1	0.3	0.5	0.8	1.0	1.2	1.7	2.0	
	0	15	0.1	0.3	0.5	0.8	-	1.2	1.7	2.0	
		30	0.1	0.3	0.5	0.8	-	1.2	1.7	2.0	
	1	15	0.1	0.3	0.5	0.8	-	1.2	1.7	2.0	
		30	0.1	0.3	0.5	0.8	-	1.2	1.7	2.0	
	2	15	0.1	0.3	0.5	0.8	-	1.2	1.7	2.0	
		30	0.1	0.3	0.5	0.8	-	1.2	1.7	2.0	
	3	15	0.1	0.3	-	0.8	-	1.2	1.7	2.0	
		30	0.1	0.3	0.5	0.8	-	1.2	1.7	-	
Small (jack on 3 rd grid)	4 (*LDV)	4	-	-	-	-	-	-	-	-	-
			-	-	-	-	-	-	-	-	-
		5	15	-	-	0.5	-	-	1.2	-	2.0
			-	-	-	-	-	-	-	-	-
		Air	15	0.1	0.3	0.5	0.8	-	1.2	1.7	2.0
			30	-	0.3	0.5	0.8	-	-	-	-
	0	15	-	-	-	-	-	-	-	-	
		30	-	-	-	-	-	-	-	-	
	1	15	-	0.3	0.5*	0.8	1.0*	1.2	1.7*	-	
		30	-	0.3	0.5	0.8	1.0*	1.2	1.7	-	
	2	15	-	0.3	0.5*	0.8	1.0*	1.2	1.7*	-	
		30	-	0.3	0.5	0.8	1.0*	1.2	1.7	-	

Confinement	# Assemblies	Velocity [m/s]	Temp. [°C]	Excitation Amplitude [mm]								
Small (jack on 3 rd grid)	4 (*LDV)	3	15	-	0.3	0.5*	0.8	1.0*	1.2	1.7*	-	
			30	-	0.3	0.5	0.8	1.0*	1.2	1.7	-	
		4	15	-	0.3	0.5*	0.8	1.0*	1.2	1.7*	-	
			30	-	0.3	0.5	0.8	1.0*	1.2	1.7	-	
		5	-	-	-	-	-	-	-	-	-	-
			-	-	-	-	-	-	-	-	-	-
		Air	-	-	-	-	-	-	-	-	-	-
			-	-	-	-	-	-	-	-	-	-
		2 (¹ also with OLD BELOW; ² PIV)	0	15	-	0.3	0.5 ¹	0.8	1.0	1.2 ¹	1.7	-
				30	-	0.3	0.5	0.8	1.0	1.2	1.7	-
	1		15	-	0.3	0.5 ^{1,2}	0.8	1.0	1.2 ¹	1.7 ²	-	
			30	-	0.3	0.5	0.8	1.0	1.2	1.7	-	
	2		15	-	0.3	0.5 ¹	0.8	1.0	1.2 ¹	1.7	-	
			30	-	0.3	0.5	0.8	1.0	1.2	1.7	-	
	3		15	-	0.3	0.5	0.8	1.0	1.2	1.7	-	
			30	-	0.3	0.5	0.8	1.0	1.2	1.7	-	
	4		15	-	0.3	0.5	0.8	1.0	1.2	1.7	-	
			30	-	0.3	0.5	0.8	1.0	1.2	1.7	-	
	5	15	-	0.3	0.5	0.8	1.0	1.2	1.7	-		
		-	-	-	-	-	-	-	-	-	-	
Air	15	-	0.3	0.5	0.8	1.0	1.2	1.7	-			
	-	-	-	-	-	-	-	-	-	-		

Table B.1: Table of Experiments

Experiments with PIV technique

Campaign	Experiment	Frequency [Hz]	Amplitude [mm]	Velocity[m/s]	Temp.[°C]	Point
10	1	0	0,5	1	20	2Y
10	2	0	0,5	1	20	2Y
10	3	0	0,5	1	20	2Y
10	5	1	0,5	1	20	2Y
10	6	1	0,5	1	20	2Y
10	7	1	0,5	1	20	2Y
10	8	3	0,5	1	20	2Y
10	9	3	0,5	1	20	2Y
10	10	4,95	0,5	1	20	2Y
10	11	4,95	0,5	1	20	2Y
10	12	5,8	0,5	1	20	2Y
10	13	5,8	0,5	1	20	2Y
10	14	8,06	0,5	1	20	2Y
10	15	8,06	0,5	1	20	2Y
10	16	9	0,5	1	20	2Y
10	17	11	0,5	1	20	2Y
10	18	12,4	0,5	1	20	2Y
10	19	12,4	0,5	1	20	2Y
10	20	14,8	0,5	1	20	2Y
10	21	21,4	0,5	1	20	2Y
10	22	1	1,7	1	20	2Y
10	23	2,8	1,7	1	20	2Y
10	24	4,95	1,7	1	20	2Y
10	25	5,7	1,7	1	20	2Y
10	26	7,08	1,7	1	20	2Y
10	27	8,91	1,7	1	20	2Y

Campaign	Experiment	Frequency [Hz]	Amplitude [mm]	Velocity [m/s]	Temp. [°C]	Point
10	28	9,5	1,7	1	20	2Y
10	29	11	1,7	1	20	2Y
10	30	12,21	1,7	1	20	2Y
10	31	14	1,7	1	20	2Y
10	32	21,2	1,7	1	20	2Y
11	3	0	0,5	1	20	2W
11	4	1	0,5	1	20	2W
11	5	1	0,5	1	20	2W
11	6	3	0,5	1	20	2W
11	7	3	0,5	1	20	2W
11	8	4,95	0,5	1	20	2W
11	9	4,95	0,5	1	20	2W
11	10	5,8	0,5	1	20	2W
11	11	5,8	0,5	1	20	2W
11	12	8,06	0,5	1	20	2W
11	13	9	0,5	1	20	2W
11	14	11	0,5	1	20	2W
11	15	12,4	0,5	1	20	2W
11	16	14,8	0,5	1	20	2W
11	17	21,4	0,5	1	20	2W
11	18	1	1,7	1	20	2W
11	19	1	1,7	1	20	2W
11	20	2,8	1,7	1	20	2W
11	21	2,8	1,7	1	20	2W
11	22	4,95	1,7	1	20	2W
11	23	4,95	1,7	1	20	2W
11	24	5,7	1,7	1	20	2W
11	25	5,7	1,7	1	20	2W
11	26	7,08	1,7	1	20	2W

Appendix B. Tables of Experiments

Campaign	Experiment	Frequency [Hz]	Amplitude [mm]	Velocity [m/s]	Temp. [°C]	Point
11	27	7,08	1,7	1	20	2W
11	28	8,91	1,7	1	20	2W
11	29	9,5	1,7	1	20	2W
11	30	11	1,7	1	20	2W
11	31	12,21	1,7	1	20	2W
11	32	14	1,7	1	20	2W
11	33	21,2	1,7	1	20	2W
11	34	0	1,7	1	20	2W
11	35	0	1,7	1	20	2W
12	5	0	0,5	1	20	2C
12	6	0	0,5	1	20	2C
12	7	0	0,5	1	20	2C
12	8	1	0,5	1	20	2C
12	9	3	0,5	1	20	2C
12	10	4,95	0,5	1	20	2C
12	11	4,95	0,5	1	20	2C
12	12	5,8	0,5	1	20	2C
12	13	5,8	0,5	1	20	2C
12	14	8,06	0,5	1	20	2C
12	15	9	0,5	1	20	2C
12	16	11	0,5	1	20	2C
12	17	12,4	0,5	1	20	2C
12	18	14,8	0,5	1	20	2C
12	19	21,4	0,5	1	20	2C
12	20	1	1,7	1	20	2C
12	21	2,8	1,7	1	20	2C
12	22	4,95	1,7	1	20	2C
12	23	4,95	1,7	1	20	2C
12	24	5,7	1,7	1	20	2C

Campaign	Experiment	Frequency [Hz]	Amplitude [mm]	Velocity [m/s]	Temp. [°C]	Point
12	25	5,7	1,7	1	20	2C
12	26	7,08	1,7	1	20	2C
12	27	8,91	1,7	1	20	2C
12	28	9,5	1,7	1	20	2C
12	29	11	1,7	1	20	2C
12	30	12,21	1,7	1	20	2C
12	31	14	1,7	1	20	2C
12	32	21,2	1,7	1	20	2C
12	33	0	1,7	1	20	2C
12	34	0	1,7	1	20	2C
13	4	0	0,5	1	17	3W
13	5	0	0,5	1	17	3W
13	6	4,95	0,5	1	17	3W
14	1	4,95	0,5	1	17	3W
14	2	8,06	0,5	1	17	3W
14	3	8,06	0,5	1	17	3W
14	4	12,4	0,5	1	17	3W
14	5	12,4	0,5	1	17	3W
14	7	4,95	1,7	1	17	3W
14	8	4,95	1,7	1	17	3W
14	9	8,91	1,7	1	17	3W
14	10	8,91	1,7	1	17	3W
14	11	12,21	1,7	1	17	3W
14	12	12,21	1,7	1	17	3W
14	13	0	1,7	1	17	3W

Table B.2: PIV measurement campaign

Bibliography

- Albrecht, H-E, Damaschke, Nils, Borys, Michael, & Tropea, Cameron. 2013. *Laser Doppler and phase Doppler measurement techniques*. Springer Science & Business Media.
- Boccaccio, Romain. 2015. *Etude expérimentale du comportement sous séisme de quatre assemblages combustibles à échelle réduite sur ICARE*. M.Phil. thesis, ENSIAME.
- Bouzet, Corentin. 2018. *Conception et processus de réalisation d'une installation expérimentale pour l'étude de la réponse mécanique sous transitoire sismique d'une ligne d'assemblages de combustibles rep*. M.Phil. thesis, Paristech Arts et Métiers.
- Capanna, R, Ricciardi, G, Eloy, C, & Sarrouy, E. 2017. Confinement Effects on Added Mass of Cylindrical Structures in a Potential Flow. *Pages V004T04A038–V004T04A038 of: ASME 2017 Pressure Vessels and Piping Conference*. American Society of Mechanical Engineers.
- Capanna, Roberto. 2014. *Contribution to the development of a calculation scheme into the code APOLLO3 dedicated to the modelling of an accidental scenario of type RIA in a nuclear power plant*. M.Phil. thesis, PoliMi.
- Capanna, Roberto. 2018. *Modelling of fluid structure interaction by potential flow theory in a pwr under seismic excitation*. Ph.D. thesis, Ecole Centrale Marseille.
- Capanna, Roberto, Ricciardi, Guillaume, Sarrouy, Emmanuelle, & Eloy, Christophe. 2019. Experimental study of fluid structure interaction on fuel assemblies on the ICARE experimental facility. *Nuclear Engineering and Design*, **352**, 110146.
- Carlton, John. 2018. *Marine propellers and propulsion*. Butterworth-Heinemann.
- Clément, Simon. 2014. *Mise en oeuvre expérimentale et analyse vibratoire non-linéaire d'un dispositif à quatre maquettes d'assemblages combustibles sous écoulement axial*. Ph.D. thesis, Aix-Marseille.
- Clement, Simon, Bellizzi, Sergio, Cochelin, Bruno, & Ricciardi, Guillaume. 2014. Sliding window proper orthogonal decomposition: Application to linear and nonlinear modal identification. *Journal of Sound and Vibration*, **333**(21), 5312–5323.
- Department, U.S. Energy. 2019. "Nuclear 101: How Does a Nuclear Reactor Work?". <https://www.energy.gov/ne/articles/nuclear-101-how-does-nuclear-reactor-work?>
- Kalkert, Christin, & Kayser, Jona. 2006. *Laser Doppler Velocimetry*. San Diego: *PHYS173*.

BIBLIOGRAPHY

- Lamarsh, John R, & Baratta, Anthony John. 2001. *Introduction to nuclear engineering*. Vol. 3. Prentice hall Upper Saddle River, NJ.
- Lanning, JH, & Battin, RH. Random Processes in Automatic Control, 1956. New York, McGraw-Hill, Library of Congress, Catalog Card.
- Lewis, Elmer E. 2008. *Fundamentals of nuclear reactor physics*. Elsevier.
- Lighthill, MJ. 1960. Note on the swimming of slender fish. *Journal of fluid Mechanics*, **9**(2), 305–317.
- Lombardi, Carlo. 2012. *Impianti nucleari*. Polipress.
- Mokhtari, Samy. 2016. *Etude du comportement sous séisme de 4 assemblages combustibles échelle réduite sur l'installation ICARE*. M.Phil. thesis, Ecole des Ponts ParisTech.
- Murray, Raymond, & Holbert, Keith E. 2014. *Nuclear energy: an introduction to the concepts, systems, and applications of nuclear processes*. Elsevier.
- Nagargoje, Mahesh. 2017 (11). *An introduction to particle image velocimetry (PIV) technique*.
- NationalInstrument. 2019. *Understanding FFTs and Windowing*. <https://www.ni.com/it-it/innovations/white-papers/06/understanding-ffts-and-windowing.html>.
- Paidoussis, MP. 1966. Dynamics of flexible slender cylinders in axial flow Part 1. Theory. *Journal of Fluid Mechanics*, **26**(4), 717–736.
- Païdoussis, MP. 2003. *Slender Structures and Axial Flow, vol. 2* Elsevier.
- Raffel, Markus, Willert, Christian E, Scarano, Fulvio, Kähler, Christian J, Wereley, Steve T, & Kompenhans, Jürgen. 2018. *Particle image velocimetry: a practical guide*. Springer.
- Ricciardi, Guillaume. 2008. *Une approche milieu poreux pour la modélisation de l'interaction fluide-structure des assemblages combustibles dans un coeur de réacteur à eau pressurisée: simulation et expérimentation*. Ph.D. thesis, Université de Provence-Aix-Marseille I.
- Ricciardi, Guillaume. 2016. Fluid–structure interaction modelling of a PWR fuel assembly subjected to axial flow. *Journal of Fluids and Structures*, **62**, 156–171.
- Ricciardi, Guillaume, & Boccaccio, Eric. 2014. Measurements of fluid fluctuations around an oscillating nuclear fuel assembly. *Journal of Fluids and Structures*, **48**, 332–346.
- Ricciardi, Guillaume, & Boccaccio, Eric. 2015. Modelling of the flow induced stiffness of a PWR fuel assembly. *Nuclear Engineering and Design*, **282**, 8–14.
- Ricciardi, Guillaume, Bellizzi, Sergio, Collard, Bruno, & Cochelin, Bruno. 2009. Modelling Pressurized Water Reactor cores in terms of porous media. *Journal of Fluids and Structures*, **25**(1), 112–133.
- Ricotti, Marco Enrico. 2016. *Course of Introduction to nuclear engineering*.

- Stephenson, Richard. 1958. *Introduction to Nuclear Engineering*. McGraw-Hill.
- Svelto, Orazio, & Hanna, David C. 1998. *Principles of lasers*. Vol. 4. Springer.
- Talukdar, S. 2016. Vibration of continuous systems. *Profesor, Department of Civil Engineering. Indian Institute of Technology Guwahati-781039*.
- Timoshenko, S. 1953. *History of Strength of Materials* McGraw-Hill Book Company. *Inc., New York/Toronto/London*.
- ValueBound. 2008. *PIV principles*. <https://www.velocimetry.net/principle.htm>.
- Zhu, Junyong. 1996. *Laser Doppler Velocimetry for flow measurements in pulp and paper research*.